2008

Growth and characterization of nanocrystalline diamond films for microelectronics and microelectromechanical systems

Sathyaharish Jeedigunta
University of South Florida

Scholar Commons Citation

Jeedigunta, Sathyaharish, "Growth and characterization of nanocrystalline diamond films for microelectronics and microelectromechanical systems" (2008). *Graduate Theses and Dissertations.*
http://scholarcommons.usf.edu/etd/316

Growth and Characterization of Nanocrystalline Diamond Films for Microelectronics and Microelectromechanical Systems

by

Sathyaharish Jeedigunta

A dissertation submitted in partial fulfillment
of the requirements for the degree of
Doctor of Philosophy
Department of Electrical Engineering
College of Engineering
University of South Florida

Co-Major Professor: Ashok Kumar, Ph.D.
Co-Major Professor: Shekhar Bhansali, Ph.D.
Stephen E Saddow, Ph.D.
Jing Wang, Ph.D.
John Bumgarner, Ph.D.
Priscila Spagnol, Ph.D.

Date of Approval:
May 29, 2008

Keywords: chemical vapor deposition, nucleation, mems, field emission, pressure sensor

DEDICATION

To My Family

ACKNOWLEDGMENTS

I would like to thank my co-advisor Prof. Ashok Kumar, for giving me an opportunity to pursue my doctoral studies in his group. I would also like to thank my other co-advisor Prof. Shekhar Bhansali, for his timely suggestions during my research. Special thanks are due to Prof. Stephen E Saddow and Prof. Jing Wang for their invaluable help and support. I would like to highly acknowledge Dr. John Bumgarner for extending support through out this course of research. I thank Dr. Priscila Spagnol for her invaluable guidance during this research. I would like to thank Dr. Timothy Short and his group members for helping me with the device testing. I have learnt a great deal working with everyone at the MEMS STAR Center. My thanks are due to all the members at COT, SRI International, NNRC, AMRL and engineering machine shop. I have to thank office staff in the departments of mechanical, and electrical engineering and college of marine science for processing all the paper work in time. The NEXAFS study during this research was conducted at the synchrotron radiation center, University of Wisconsin–Madison, supported by the NSF under contract no. DMR-0084402. The financial support for this research came from NSF NIRT grant # ECS 0404137 and space and missile defense command (SMDC) grant # W9113M-06-C-0022. I would like to acknowledge the encouragement and support from my family, friends, and colleagues.

TABLE OF CONTENTS

CHAPTER 3. GROWTH AND CHARACTERIZATION OF NANO-CRYSTALLINE DIAMOND FILMS 29

LIST OF TABLES

LIST OF FIGURES

Growth and Characterization of Nanocrystalline Diamond Films for Microelectronics and Microelectromechanical Systems

Sathyaharish Jeedigunta

ABSTRACT

Diamond is widely known for its extraordinary properties, such as high thermal conductivity, energy bandgap and high material hardness and durability making it a very attractive material for microelectronic and mechanical applications. Synthetic diamonds produced by chemical vapor deposition (CVD) methods retain most of the properties of natural diamond. Within this class of material, nanocrystalline diamond (NCD) is being developed for microelectronic and microelectromechanical systems (MEMS) applications. During this research, intrinsic and doped NCD films were grown by the microwave plasma enhanced chemical vapor deposition (MPECVD) method using $CH_4/Ar/H_2$ gas mixture and $CH_4/Ar/N_2$ gas chemistries respectively.

The first part of research focused on the growth and characterization of NCD films while the second part on the application of NCD as a structural material in MEMS device fabrication. The growth processes were optimized by evaluating the structural, mechanical and electrical properties. The nature of chemical bonding, namely the ratio of sp^2:sp^3 carbon content was estimated by Raman spectroscopy and near edge x-ray absorption fine structure (NEXAFS) techniques. The micro-structural properties were studied by x-ray diffraction (XRD), atomic force microscopy (AFM), scanning electron microscopy (SEM), and transmission electron microscopy (TEM). The mechanical properties of the pure NCD films were evaluated by nano-indentation. The electrical properties of the conductive films were studied by forming ohmic as well as schottky contacts.

In second part of this study, both free-standing and membrane capped field emitter devices were fabricated by a silicon mold technique using nitrogen incorporated (i.e., doped) NCD films. The capped field emission devices act as a prototype vacuum microelectronic sensor. The field emission tests of both devices were conducted using a diode electrical device model. The turn-on field and the emission current of free-standing emitter devices was found to be approximately 0.8 V/μm and 20 μA, respectively, while the turn-on fields of capped devices increased by an order of magnitude. The emission current in the field emission sensor changed from 1 μA to 25 μA as the membrane was deflected from 280 μm to 50 μm from the emission tip, respectively.

CHAPTER 1. INTRODUCTION

1.1. Introduction to CVD Diamond

“Diamond” has been known to common man as a precious stone in jewelry since biblical times [1]. Even before it was realized as an ornament, diamonds were used in grinding, polishing, and as hard coatings on drill bits, cutting tools and dicing saws. Besides the superlative mechanical properties, they possess extraordinary electrical, electronic, thermal, and optical properties. Hence, diamond can be useful in applications such as high power electronics, heat sinks, and radiation detectors [2]. Diamond is suitable for operation in harsh environments (except oxygen ambience) as it is highly inert to most acids, bases and other chemicals [3]. The difficulty in engineering diamond to a desired shape and size has limited its applications to a great extent.

Hence, several researchers have investigated suitable alternative methods to produce synthetic diamond. Most of the early growth techniques failed to deposit good quality diamond films. In 1952, *William G. Eversole* of the *Union Carbide Corporation* reported the first successful growth of diamond using a low-pressure chemical vapor deposition method. Later, the low pressure growth technique was confirmed by other groups [1, 2, 4]. This method involved heating the carbon containing gaseous mixture in diamond powder at temperatures ~ 1000° C. Due to the simultaneous growth of graphitic carbon, the deposition rate on the order of only 0.01 μm/hr was achieved [5]. *Eversole et. al.* suggested periodic injection of diamond powder into hydrogen gas to etch the graphitic carbon and improve the growth rate [6, 7]. In 1974, *Russian* scientists developed a method of heating the diamond powder by short pulses in a high pressure gas discharge, which resulted in a higher growth rate of 1μm/hr [8].

It was in 1955 that a reproducible deposition method using high pressure technique has been reported by the *General Electric Company* [5]. The initial interest was in the synthesis of single crystal, homo-epitaxial films, and high pressure high temperature (HPHT) diamonds [9]. The high cost of single crystal diamond substrates has encouraged researchers to focus on the growth of diamond films on non-diamond substrates. Preliminary research toward this end has produced another fascinating class of material known as diamond-like-carbon (DLC) [10].

1.2. Phase Diagram of Carbon Based Materials

Although CVD has been widely accepted as an ideal deposition technique to grow diamond films, the difficulty in the diamond growth is due to its metastable nature. The deposition conditions favor the nucleation of both diamond and graphite crystals. The phase diagram of carbon based materials is shown in Figure 1.1 [118]. It can be found that the growth regime of CVD diamond is surrounded by the growth of graphitic carbon.

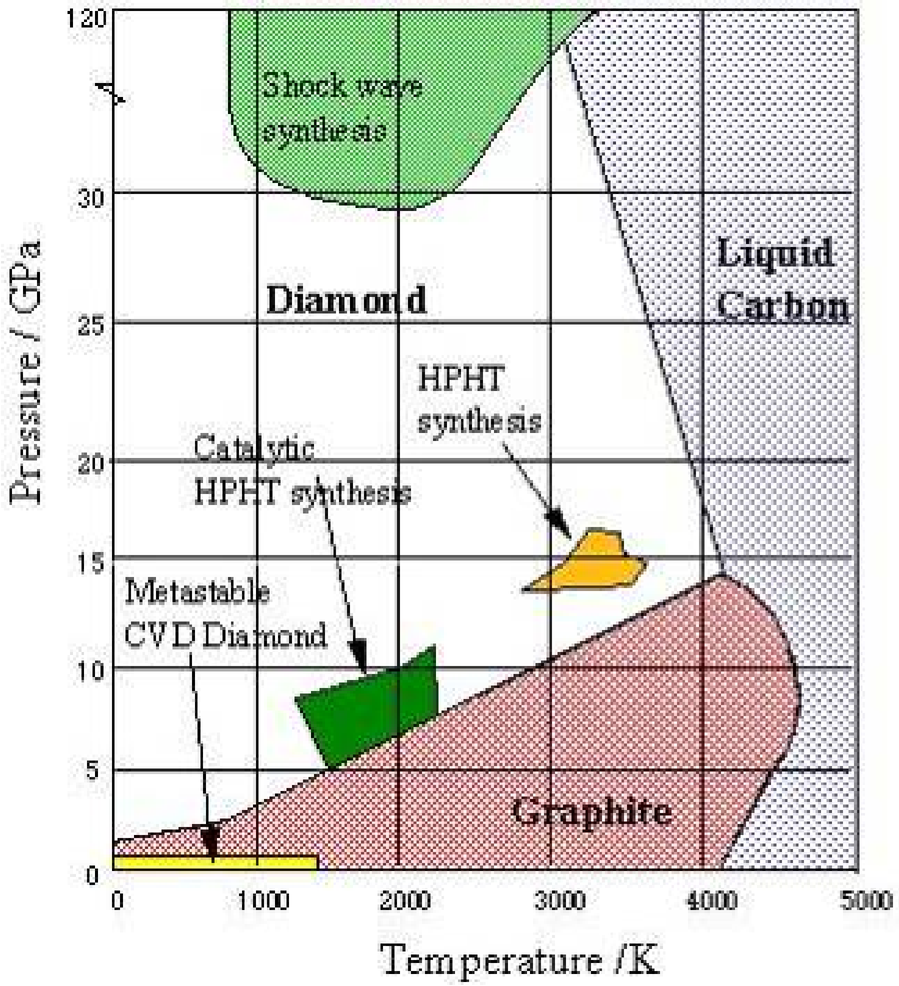

Figure 1.1 Phase Diagram of Carbon Based Materials [118]

Therefore, the relationship between the diamond and graphite is thermodynamic and kinetic one. At normal temperatures and pressures, the activation energy of graphite is only few eV higher than diamond which results in the existence of diamond. Once the diamond crystal is formed, there is no easy mechanism to convert into graphite without completely destroying the lattice.

1.3. Crystal Structure of Diamond

The face centered cubic crystal (FCC) lattice of diamond consists of a unique arrangement of carbon atoms with eight corner atoms, six face centered atoms and four other atoms from adjacent interpenetrating lattices offset by one-quarter of the body diagonal as shown in the ball and stick model of Figure 1.2 [11]. Each of the carbon atoms is covalently bonded to four nearest neighboring atoms resulting in a strong sp^3 character. The (111) planes of the diamond are along the bond direction with a lattice constant (a_0) of 3.567 Å and a bond length of 1.54 Å [12]. Due to this unique chemical bonding, and atomic density of 1.76 X 10^{23} cm^{-3}, diamonds possess several extraordinary material properties.

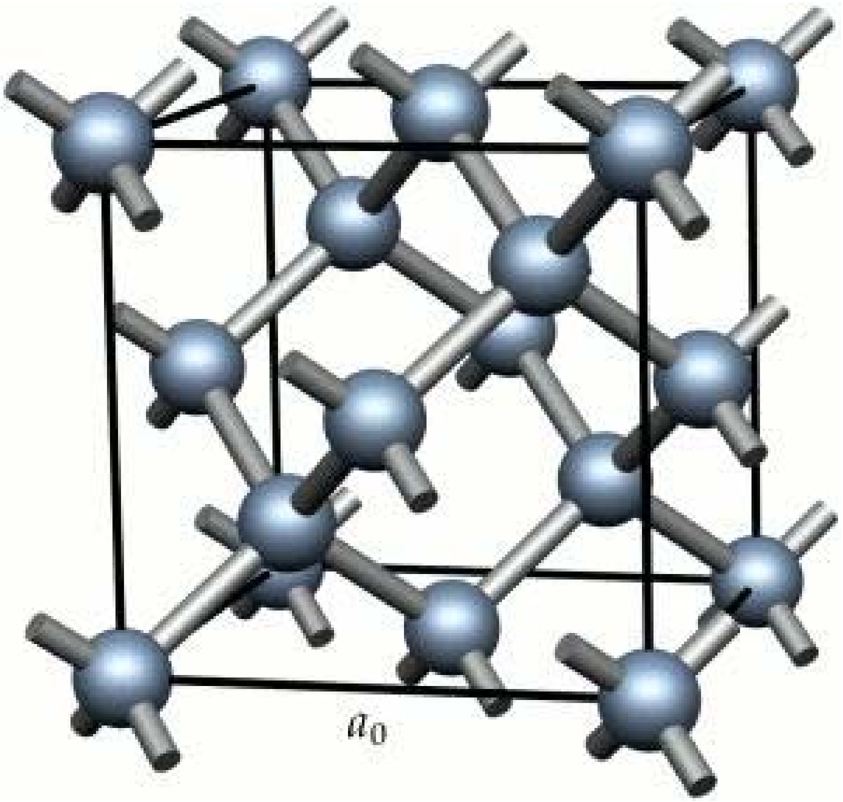

Figure 1.2 Crystal Structure of Diamond Lattice [11]

1.4. Fundamental Properties of Single Crystal Diamond

Table 1.1 summarizes few important properties of diamond [4, 13, 14]. It is evident that diamond is suitable for a wide range of mechanical, thermal and electronic applications.

Table 1.1 Fundamental Properties of Single Crystal Diamond

Property	Value
➢ STRUCTURAL PROPERTIES	
Crystal structure	FCC(*sp*^{3} bonded, tetrahedral)
Atomic density	1.76 X 10^{23}cm^{-3}
Lattice constant	3.567 Å
Density	3.52 gmcm^{-3}
➢ MECHANICAL PROPERTIES	
Young's modulus	1050 GPa
Coefficient of friction	0.03
Knoop hardness	110 GPa
➢ THERMAL PROPERTIES	
Thermal expansion coefficient	1.1 X 10^{-6} k^{-1}
Thermal conductivity	2500 W/m-k
➢ OPTICAL PROPERTIES	
Optical index of refraction(at 591 nm)	2.41

Table 1.1 (Continued)

Optical transmittivity	225 nm (UV) to long IR (> 25 μm), IR absorption band from 2-7 μm
➢ ELECTRICAL PROPERTIES	
Intrinsic resistivity	10^{13}-10^{16} Ω-cm
Bandgap	5.45 eV
Electron affinity	~ -1 eV
Dielectric constant	5.7
Dielectric strength	1.0 X 10^7 Vcm^{-1}
Electron mobility	2200 $cm^2(Vs)^{-1}$
Hole mobility	1600 $cm^2(Vs)^{-1}$

It can be found that diamond has some of the extraordinary material properties required not only for cutting tools and abrasive coatings, but also for microelectronics and microelectromechanical systems and applications. As silicon technology is well matured, most of the present day microelectronic and MEMS devices are fabricated using silicon. Due to some of its poor material properties, other materials such as SiC and diamond are also currently under investigation especially for the fabrication of MEMS devices. Some of the properties of Si, SiC and diamond are shown in Table 1.2. It can be observed that diamond possess much better properties than both silicon and silicon carbide.

Table 1.2 Fundamental Properties of Silicon, Silicon Carbide and Diamond

Property	Silicon	SiC	Diamond
Lattice Constant (Å)	5.43	4.358 (β-SiC)	3.567
Hardness (GPa)	10	35	110
Young's Modulus (GPa)	130	450	1050
Thermal Conductivity ($Wcm^{-1}K^{-1}$)	1.5	5	25
Thermal Expansion (10^{-6} °C)	2.6	4.7	1.1
Melting Point (°C)	1420	2540	4000
Band gap (eV)	1.1	3.0	5.45
Resistivity $(\Omega.cm)^{-1}$	10^{3}	150	10^{13}-10^{16}
Break down voltage (X 10^{5} Vcm^{-1})	3	40	100
Dielectric constant	11.8	9.7	5.7

1.5. Scope and Outline of the Dissertation

This dissertation discusses various aspects of nucleation, growth and characterization of intrinsic and conductive nanocrystalline diamond films deposited by microwave plasma enhanced chemical vapor deposition (MPECVD) method. Both intrinsic and conductive NCD films were used as structural material in the fabrication of MEMS devices. The fabrication of vertical NCD based field emission source/sensor and their field emission characteristics were presented.

Chapter 1 starts with a brief history about CVD diamond films along with some of the interesting properties which make diamond a potential candidate for mechanical, electrical and thermal applications.

Chapter 2 provides a background on field emission, and the advantages of using NCD films for the fabrication of field emission devices. The fabrication procedures and the field emission properties of vertical and lateral field emission devices are discussed. This chapter concludes with an introduction to the principle of field emission based sensing as well as some of the earlier work reported by other researchers.

Chapter 3 provides insight into the growth and characterization of intrinsic and conductive nanocrystalline diamond films. A detailed study on nucleation and deposition of NCD films is presented. The electrical properties of nitrogen incorporated conductive NCD films conclude this section of the dissertation.

In Chapter 4, the approach towards the fabrication of a field emission source and a field emission sensor are presented. An overview on the fabrication procedure of vertical field emitter arrays by silicon mold technique is provided. The method of testing the field emission source and sensor for their emission characteristics are discussed in the last section of this chapter.

Chapter 5 provides the design specifications of both field emitter arrays and anode-on-membrane arrays. For the design of anode, two types of membranes: free standing and boss type structures have been considered in the current research. The finite element modeling and the mechanical analysis of the membranes were performed in *Coventorware*^{TM}. The effect of membrane dimensions and external load on the deflection of the membranes is also discussed.

Chapter 6 presents the fabrication details of free-standing NCD field emitter arrays and a fully packaged capped field emission source. The fabrication of NCD field emission sensor involves a three-wafer process with five levels of lithography and two levels of packaging: a-chip-level and a wafer-level. This section also discusses the field emission behavior of both types of devices.

Chapter 7 concludes the dissertation with a summary of the current investigations and suggests few recommendations on the future work of the present research activity.

CHAPTER 2. BACKGROUND ON FIELD EMISSION

2.1. Introduction

With a revolution in semiconductor field, there was a tremendous growth in the electronics industry during the last decade of the 20th century. Inventions such as cellular phones, palm and laptops, and flat panel displays have indicated remarkable progress made in this field. The past 10 years, there has been an increasing momentum in the display industry. The evolution of liquid crystal displays (LCD's) and plasma displays have replaced the bulky monitors in computers and televisions with sleek, compact and lightweight flat panel displays. Field emission displays (FED's) can be an alternative and efficient display technology [15]. FED's provide a flat panel technology that features less power consumption than existing LCD and plasma display technologies. Besides, they can be cheaper to make as they have fewer total number of components. Field emission sources are also used in electron microscopes [16], MEMS devices [17] and vacuum microelectronic devices [18].

The principle of field emission is based on the quantum mechanical tunneling of electrons emitted from the surface of a material into vacuum under an applied electric field. If a material possesses sufficiently small work function and electron affinity, the barrier height can be small, and electrons can tunnel through the narrow potential barrier. The first field emission devices fabricated using molybdenum tips were known as "Spindt type cathodes" or "Spindt - FEA's" [19]. In the meantime, alternative materials such as Si [20], cubic-Boron Nitride(c-BN) [21], AlN [22], Barium Strontium Titanate (BST) [23], and nanostructures of Si [24], SiC [25], ZnO [26], In_2O_3 [27], SnO_2 [28] and TiO_2 [29] were also investigated for field emission applications. It was later found that carbon based materials such as carbon nanotubes (CNT's) [30], diamond-like-carbon (DLC) [31] and diamond [32] can be efficient electron emitters. The synthesis of vertically aligned CNT's has opened a new direction for the fabrication of field emission arrays [30].

The fabrication of emitter devices with a gate or a collector at a micro/nanoscale involves expensive fabrication processes. It will be cost-effective if the material used can compensate for the cost of fabrication in terms of its enhanced performance. For efficient tunneling of electrons, the material should possess low work function, electron affinity, and dielectric constant, and high thermal conductivity, melting point, and chemical and physical robustness [33]. Most of the carbon based materials possess these properties and, hence, are very suitable for field emission and related applications.

2.2. Principle of Field Emission

The electrons inside a material are bound closely by an electrostatic force of attraction. Due to this force, a potential barrier known as "work function" is established. For any material to emit these closely bound electrons, they have to overcome this potential barrier and escape to the vacuum level. When a sufficient thermal energy is supplied to a material, electrons in the conduction band gain kinetic energy required to escape into vacuum. In another way, the electrons can be released by applying high electric fields or by applying both thermal and electric fields. Field emission is based on the principle of extracting electrons from the surface of a metal or a highly doped semiconductor to vacuum by applying a potential or an electric field. The electron affinity is "the amount of energy required for an electron to release from the conduction band into the vacuum level". Hence, it is evident that materials with small or negative electron affinity can easily emit electrons from their surfaces.

The energy band diagrams of a positive electron affinity (PEA), effective negative electron affinity (NEA) and a true NEA diamond surfaces are shown in Figure 2.1 (a-c), respectively [34]. The electron affinity of diamond depends on the amount of hydrogen present. If the surface of the diamond is completely free of hydrogen, the net electron affinity is positive. Therefore, the highest level of the conduction band edge is below the vacuum level resulting in a potential barrier (or electron affinity) between the diamond-vacuum interfaces (Figure 2.1(a)). On the other hand, when the surface of the diamond is partially hydrogenated, a positive dipole is induced which results in the band bending and correspondingly a smaller electron affinity value than the previous case. In that case, the surface of the diamond will have an effective NEA where the highest level of the conduction band edge is above the vacuum level while the lowest level of the conduction band edge bends below the vacuum level (Figure 2.1(b)). In Figure 2.1(c), the energy band diagram of a true NEA surface of diamond is shown.

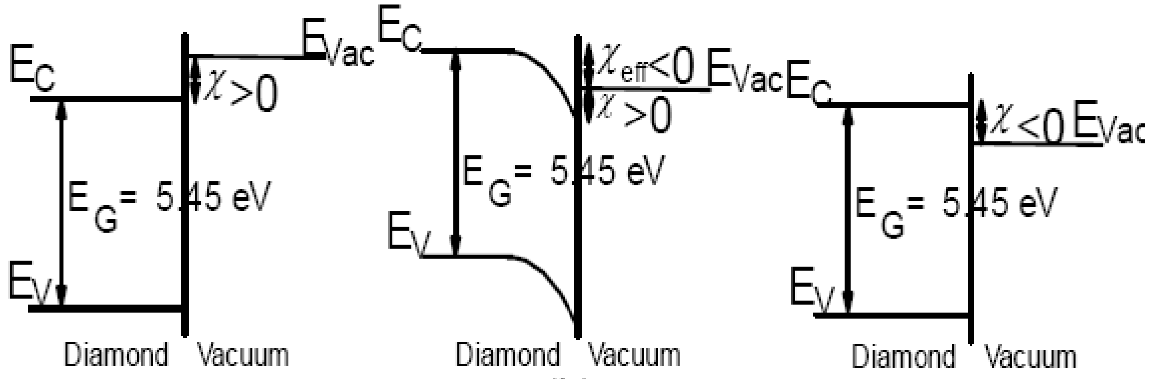

(a) (b) (c)

Figure 2.1 Energy Band Diagram of Diamond Surfaces (a) Positive Electron Affinity (b) Effective Negative Electron Affinity (c) True Negative Electron Affinity [34]

A true NEA surface in diamond is obtained only when the surface is fully hydrogenated. As the conduction band is above the vacuum level, the net barrier height is negative and therefore, electrons can easily flow from the conduction band to the vacuum level without any potential drop. A true NEA surface is not usually observed in many semiconductors and therefore was not believed to exist.

If the emitting surface is a flat film, the corresponding electric field is given by E=V/d where 'V' is the applied voltage and 'd' is the separation between the film and the anode. But if the emitting surface consists of tips, the electric field not only depends on the applied voltage and the separation but also on the geometry of the tip [37]. The field emission current is governed by the Fowler-Nordheim (F-N) principle [38]. According to Fowler-Nordheim tunneling, the current density is given by Eq 2.1.

$$J = AE^2 \exp\left(\frac{-B}{E}\right) \tag{2.1}$$

where 'J' is the current density, 'E' is the electric field in the insulator, A and B are constants given by

$$A = \frac{m}{m^*}\frac{q^3}{8\pi h\phi_B} \tag{2.2}$$

$$B = \frac{8\pi}{3}\left(2\frac{m^*}{h^2}\right)^{\frac{1}{2}}\frac{\phi_B^{\frac{3}{2}}}{q} \tag{2.3}$$

$$E = \frac{\beta V}{d} \tag{2.4}$$

where m, m*, q, h and Φ_B are the electron mass, the effective electron mass, the electronic charge, the Planck's constant and the barrier height respectively. 'β' is the field enhancement factor, 'V' is the applied potential and 'd' is the thickness of the oxide layer. The field enhancement factor can be expressed in terms of the geometry of the tip. Accordingly, β = L/R, where 'L' is the height of the tip, 'R' is the radius of the curvature of the tip. Substituting all the terms in Eq. 2.1, it can be rewritten as

$$I = aJ = aA\left(\frac{LV}{Rd}\right)^2 \exp\left(\frac{-B}{\frac{LV}{Rd}}\right) \tag{2.5}$$

As can be observed from the above equations, for a fixed thickness of insulator(d) the emission current (I) primarily depends on the emission area (a), applied bias ‘V’, height of the tip ‘L’, the radius of curvature of the tip ‘R’ and the work function ‘Φ_B’.

2.3. Advantages of Nanocrystalline Diamond (NCD) Films for Field Emission Sources

Table 2.1 shows the properties of few materials that were investigated for field emission applications [33].

Table 2.1 Properties of Materials Suitable for Field Emission Applications [33]

Material	Fusion Point (°C)	Dielectric Constant	Band gap (eV)	Electron affinity (eV)	Thermal Conductivity (W $K^{-1}cm^{-1}$)
Diamond	**3550**	**5.7**	**5.5**	**-0.7**	**20**
Cubic-BN	2700	7.1	6	NEA	1
AlN	2400	9.1	6.2	NEA	3
amorphous-SiO_2	1700	3.9	9	0.6-0.8	0.02
Al_2O_3	2030	9.4	8.3	0.88	0.46
LiF	870	9.3	14.2	-2.7	0.12
CaF_2	1423	8.4	12.1	-0.54	0.08

Of the above materials, diamond is very suitable for the fabrication of field emission devices. The emission current from the tips is usually on the order of several microamperes. In both hot and cold cathode emission devices, if the emission current from each tip increases, the temperature at the emitter tip increases tremendously due to I^2R losses and make the tips blunt and reduce the device lifetime. In order to circumvent this problem, it will be advantageous if one can fabricate the micro tip array from such a material that can easily dissipate heat, thereby can enhance the performance. In this context, the tips made from NCD films can effectively dissipate the heat due to high thermal conductivity and emit current for longer periods.

The metal emitter tips adsorb the contaminants from the surrounding environment and increases the surface work function of the material resulting in an inconsistent emission current. Hence, intermediate "conditioning the tip surface" becomes mandatory for maintaining constant emission current without a significant increase in the applied voltage [39]. This problem of surface adsorption could be minimized, if not fully be eliminated, by the use of NCD films as they provide a relatively high chemically inert surface. Hence, NCD based field emitters can be operated in harsh environments with almost equivalent performance as can be used in a normal ambience [3].

If the diamond films are completely hydrogenated or partially hydrogenated, the corresponding electron affinity values can be negative or slightly positive [35, 36]. A significant electron emission can be obtained if n-type impurities can be incorporated into the diamond films. The incorporation of n-type impurities increases the concentration of electrons in the conduction band, thereby increases the probability of more electrons to escape to the vacuum. However, the inability to successfully dope n-type diamond has limited diamond field emission devices for several years. With the recent success in obtaining n-type NCD films, diamond field emission devices have gained interest. It is widely known that the field emission from NCD films cannot be completely attributed to the NEA surface alone but was found to be also due to the defective grain boundaries consisting of graphitic carbon [40].

Unlike silicon technology, fabrication procedures of diamond-based devices are not fully mature. Besides, the growth, etching and processing of diamond films is time consuming and, hence, may not be cost effective unless the current methods are improved. Several reports on the field emission properties of diamond films, both as a flat film and also as a vertical and lateral tip shaped emitters can be found in the literature. In the below section, a brief review on the fabrication of vertical and lateral field emitter devices and their field emission properties is presented.

In a field emission diode, voltage is applied to the emitter and the current from the tip is collected at the anode (or collector). However, the fabrication of anode structures with sub-micron features may have certain limitations due to photo-lithography. Hence, alternative methods of self-aligning the gated structures have been suggested. The fabrication steps implemented by *W. P. Kang et al.,* [41] for a self-aligned structure are shown in Figure 2.2.

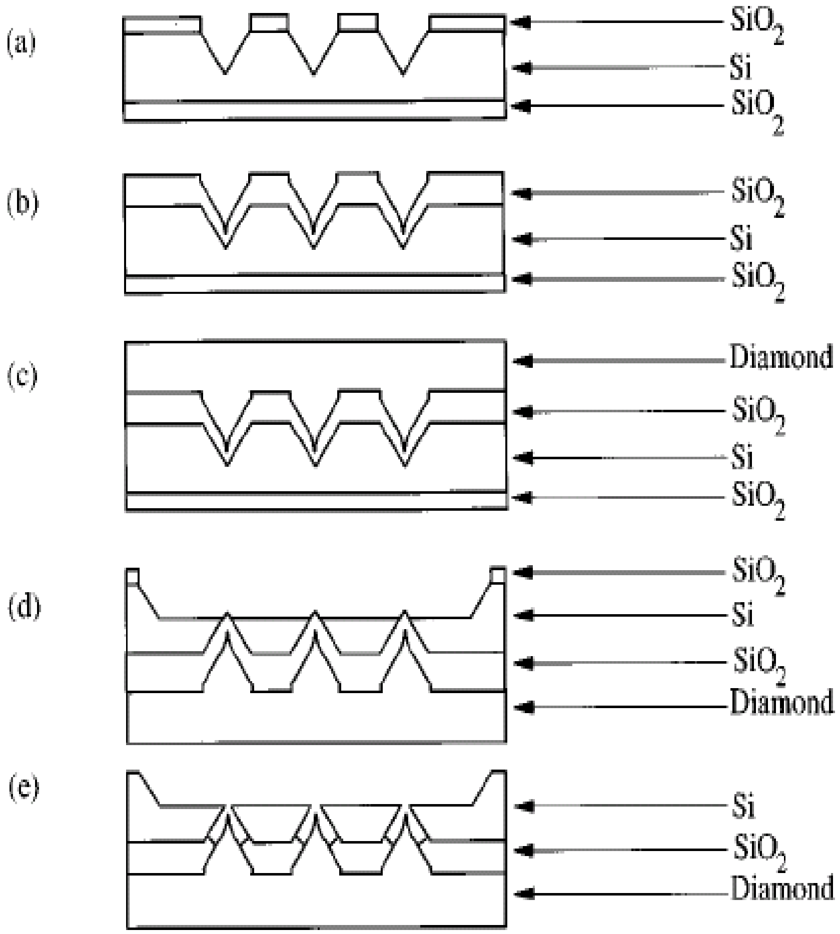

Figure 2.2 Fabrication of Vertical Field Emitter Array by Mold Technique [41]

The silicon wafer was anisotropically etched to form V-grooves by the use of standard photo-lithography and etching techniques, followed by the deposition of an insulating SiO_2 layer, and finally the diamond films were deposited by plasma enhanced chemical vapor deposition (PECVD) method on the SiO_2 inverted sharpened pyramidal mold. The thickness of SiO_2 layer determines the gap between the emitter and the anode. A square window was etched on the backside of the silicon mold to anisotropically etch the silicon substrate until the apex of the diamond tips was exposed. Finally, SiO_2 near the apex region was etched to expose the diamond tips (see Figure 2.2).

It has been reported that the field emission properties of such devices were promising, with a low turn-on voltage of ~ 0.7 V and an emission current of 4 μA at a gate voltage less than 5 V (See Figure 2.3). The linear relation of the inverse of electric field vs. the logarithmic of the square of the current/electric field indicates the Fowler-Nordheim characteristics. The enhanced field emission property in such devices was attributed to the oxide-sharpening effect of the emitter tip.

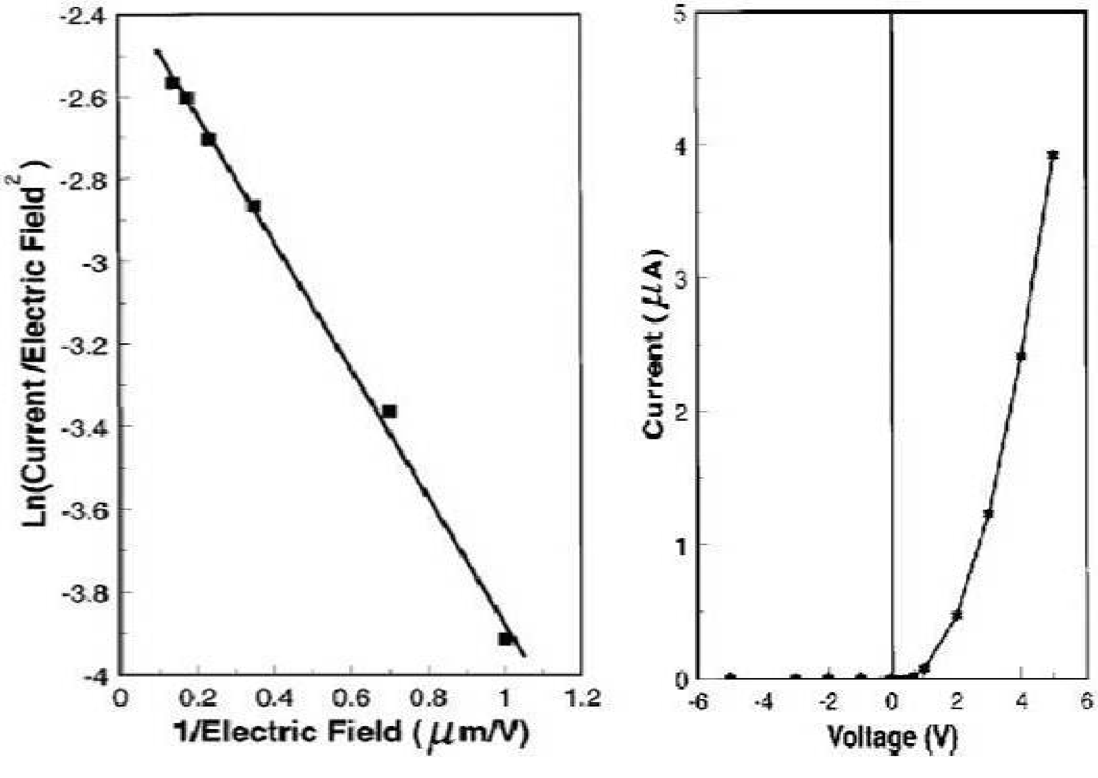

Figure 2.3 Fowler-Nordheim Characteristics of Vertical Field Emitter Array Device [41]

Even today, most of the field emission sources are fabricated in vertical configuration using mold technique. But due to the complexities in the fabrication of vertically-aligned field emitters, the fabrication of lateral field emission devices is also under investigation. The lateral emitters can be fabricated with a fairly simple fabrication procedure. The lateral field emission devices using CVD diamond films reported by *W. P. Kang et al.,* [42] included a single mask process with a high device yield of 80 %. Figure 2.4 shows the schematic of the process steps implemented in the fabrication of lateral field emitters using silicon-on-insulator (SOI) wafers.

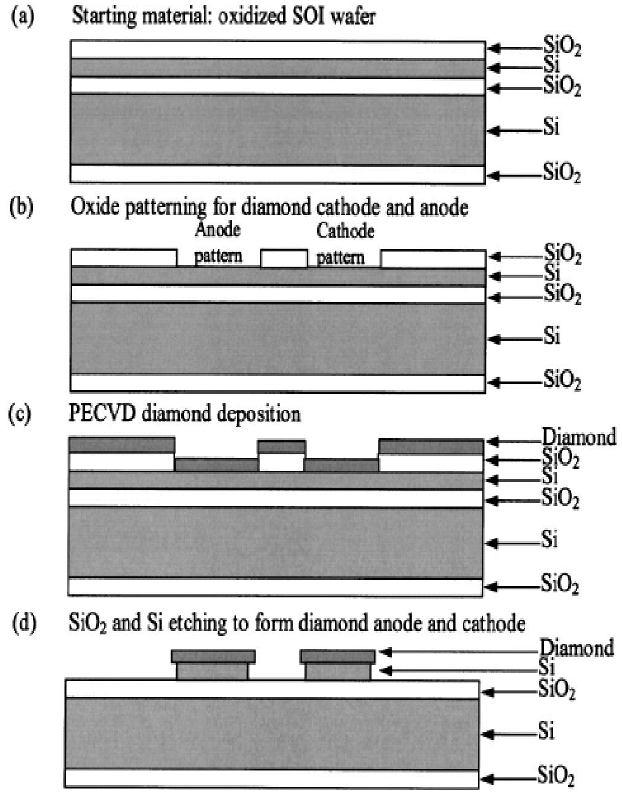

Figure 2.4 Process Steps for the Fabrication of Lateral Field Emission Device [42]

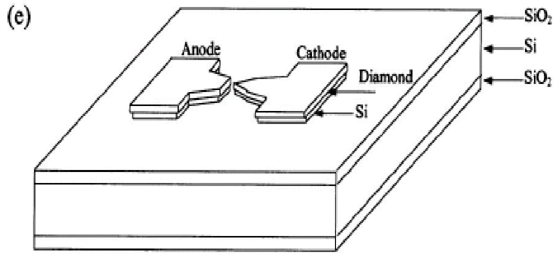

Figure 2.4 (Continued)

Boron doped diamond films (p-type) were grown on patterned SiO_2 films to form the lateral field emitter geometry. With an anode to cathode spacing of 2 μm, a turn-on voltage of 5 V, and an emission current of 6 μA have been achieved (seen in Figure 2.5). The limitation of this approach is the high cost of silicon-on-insulator (SOI) wafers as compared to standard silicon substrates.

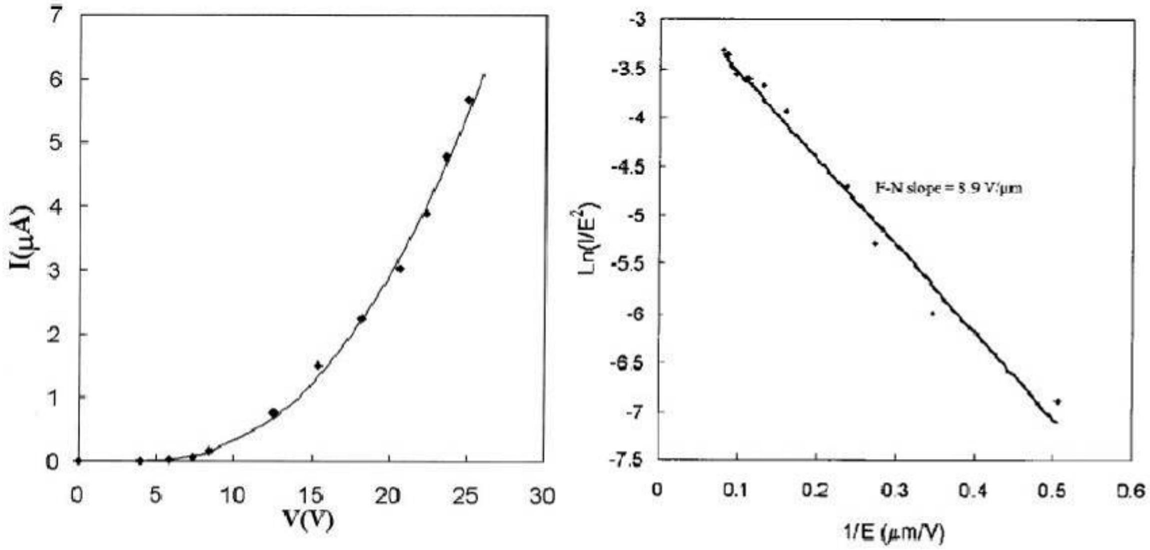

Figure 2.5 Field Emission Characteristics of Lateral Field Emission Device [42]

2.4. Field Emission Based Sensing

Miniaturizing the sensors and actuators was made possible by MEMS technology. The capacitive [43], piezo-resistive [44], and optical sensors [45] are actively investigated in commercially available MEMS sensors. The above sensing methods have their own advantages and disadvantages and, hence, the choice depends on the end application, manufacturing and integration costs, etc. Field emission based sensors can provide an alternative sensing mechanism to the existing ones. Its specific advantages such as temperature insensitivity, minimal resonance effects, and possibility to integrate with microelectronic circuits put forth this as a highly sensitive technique. A field emission sensor can operate in a diode or a triode configuration. In a diode configuration, the cathode consists of an emitter array and an anode or a collector is a thin metal plate. In a triode configuration, besides the two terminals of a diode, a control gate is fabricated to limit the emission current. The field emission sensors can be fabricated in two designs: “anode-on-membrane” geometry or “cathode-on-membrane” geometry. In the first one, anode is a flexible diaphragm while the cathode consists of fixed emitter arrays and in the second design, the cathode is fabricated on a flexible diaphragm and anode is a fixed plate.

The field emission based sensor can be operated in two modes: 1) constant current mode and 2) constant voltage mode. In both the modes of operation, the sensor sensitivity depends on the distance between the emitter tips and the membrane.

According to Fowler-Nordheim equation, the current density is given by the expression

$$J = A\left(\frac{LV}{Rd}\right)^2 \exp\left(\frac{-B}{\frac{LV}{Rd}}\right) \qquad (2.6)$$

As d →Δd, correspondingly J→ΔJ, therefore the above expression can be re-written as

$$\Delta J = A\left(\frac{LV}{R\Delta d}\right)^2 \exp\left(\frac{-B}{\frac{LV}{R\Delta d}}\right) \qquad (2.7)$$

The sensitivity (S_v or S_i) in both the cases is given by

$$S_v = \Delta V/\Delta d \text{ (I is constant)} \qquad (2.8)$$

$$S_i = \Delta I/\Delta d \text{ (V is constant)} \qquad (2.9)$$

S_v and S_i denote the sensitivity in the constant current and constant voltage modes respectively, ΔV and ΔI denote the change in the turn-on voltage and the emission current respectively and Δd denotes the deflection of the diaphragm.

Having briefly discussed the background of field emission sensing, it will be useful to know the previous research carried in this field. Most of the earlier reports on field emission sensing were based on the modeling and simulation work [46-49]. There are only a few reports in the literature that show some preliminary experimental data [50]. The theoretical and the modeling data provide good background essential for the device fabrication. The below sections will provide a review of the design, fabrication and characterization of field emission sensors reported by other researchers.

Few materials such as boron nitride, silicon, silicon carbide and DLC coatings on silicon have been used for the fabrication of field emission sensors [51, 52]. *N. Badi et al.,* have reported on the field emission based pressure micro-sensors that consist of an emitter array made with sulphur doped boron nitride films and thin membranes of Ti, Si, Ta and TiN as anodes [50]. The device worked in a diode configuration with an inter-electrode spacing of ~ 1 μm. As the electrodes were closely separated, a threshold field of ~ 50 V/μm and an emission current on the order of few milliamperes was achieved. Figure 2.6 shows the pressure vs. current relationship for various membrane materials.

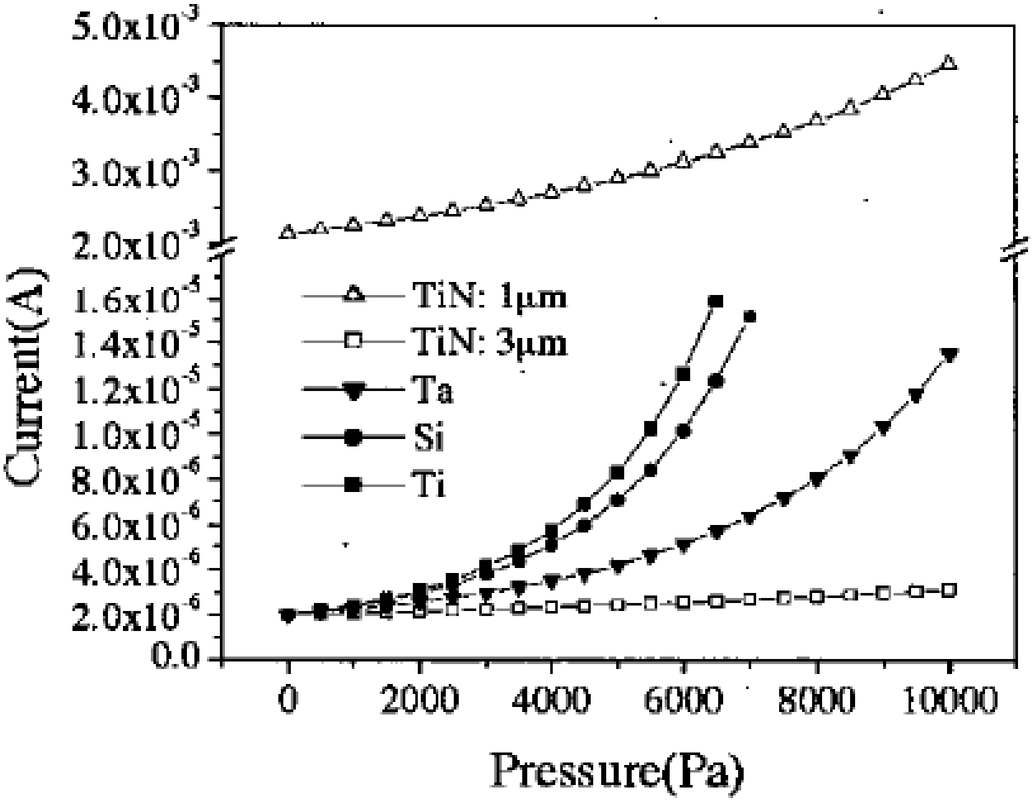

Figure 2.6 Pressure vs. Current Relationship in Field Emission Pressure Sensor [50]

It has been reported that for an emitter to gate separation of 1 μm, the magnitude of the current changed by three orders, maintaining the linearity. Through simulations, it has been found that the sensitivity range of this sensor varies from nA/Pa to μA/Pa. It can be found that Si, Ti and Ta membranes showed non-linear pressure-current characteristics while the TiN membranes showed linear response [50]. It has been reported that when thicker TiN membranes were used as anode, the emission current has not varied up to a pressure of 1000 Pa, while thinner membranes showed a significant change in the current up to 3 mA. The linear response in the TiN membrane characteristics changed to non-linear behavior when the thickness of the membrane was increased from 1 μm to 3 μm.

Dan Nicolaescu et al., [48] have developed a model to analyze the behavior of a pressure sensor using diamond film as a cathode and a flexible silicon membrane as an anode. At a constant emission current, the variation in the anode voltage accounted for the amount of pressure applied on the membrane. The effect of membrane dimensions on the pressure domain range is shown in Figure 2.7. In the analytical model, it was shown that thicker and smaller membranes required higher pressure (107 Pa) for a constant deflection of 4 μm (Figure 2.7). It can be found that as the thickness of the membrane increased from 5 μm to 60 μm, the operating pressure range increased by at least three orders of magnitude.

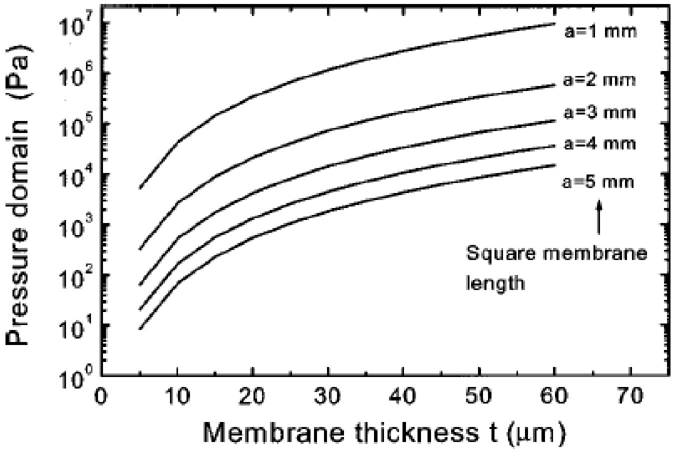

Figure 2.7 Effect of Membrane Thickness and Size on Pressure Domain [48]

Figure 2.8 shows the relationship between the operating voltages vs. the vacuum gap. It can be found that a very strong linear relation exists between the applied voltage and the vacuum gap. For a constant emission current, the anode voltage changes by more than 300 volts for an approximate change in the inter-electrode spacing of 2 µm. This model shows that a field emission based sensor can be highly sensitive even to small changes in the applied pressure or testing conditions.

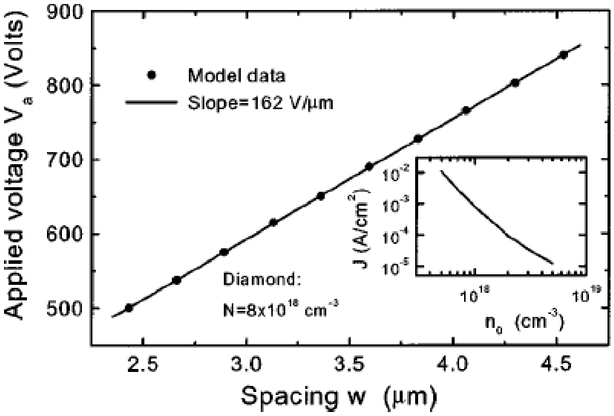

Figure 2.8 Effect of Anode to Cathode Spacing on Applied Voltage [48]

The sensitivity as a function of length of the membrane is shown in Figure 2.9.

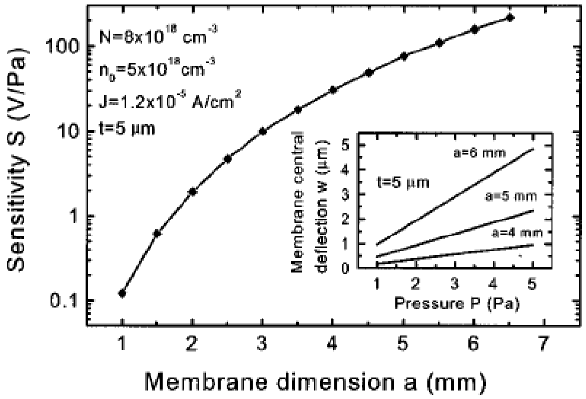

Figure 2.9 Effect of Membrane Dimensions on Sensitivity of Field Emission Pressure Sensor [48]

It has been reported that the sensitivity was inversely proportional to the dimensions of the membrane. If a stress free film can be used as a thin membrane, the sensitivity can be improved by increasing the membrane dimensions. It is evident that the dimensions of the membrane, the design specifications of membrane and emitter array as well as the spacing between the two are key elements to fabricate a reliable and a sensitive emission sensor.

The limitations due to the photo-lithography can be overcome if one can fabricate the membrane and the cathode on two different dice and bond them efficiently in such a way that the vacuum gap is only on the order of few microns, it will be possible to operate the sensor efficiently at lower operating voltage.

2.5. Summary

A background on the evolution of the field emission devices and its applications has been discussed. Though the field emission phenomenon has been observed in various semiconductor materials, the specific advantages of nanocrystalline diamond thin films have put forth its candidature for fabricating field emission devices in both vertical and lateral device geometries. The field emission based sensing has been reported as an alternative sensing technique by detecting the changes in the emission current or the turn-on voltages. The field emission based pressure sensors were fabricated using few materials such as Ti, TiN, and Si. To this end, analytical results and modeling of the field emission diode sensors have been reviewed.

CHAPTER 3. GROWTH AND CHARACTERIZATION OF NANOCRYSTALLINE DIAMOND FILMS

3.1. Introduction

It has been widely accepted by late 1970's and early 1980's that chemical vapor deposition (CVD) is the only suitable technique for growing high quality diamond films. In a CVD process, methane is used as the source of carbon and hydrogen is added to reduce the graphitic content and improve the growth rate. For over three decades, research was primarily focused on "microcrystalline diamond" (MCD) films [53]. Microcrystalline diamond films consist of large grains (grain size: ~ 5-10 μm) and rough surfaces (mean surface roughness: ~ 300-700 nm) thereby limit its application to cutting tools, abrasive coatings and heat sinks [54-56]. The limited applications of microcrystalline diamond (MCD) films have been surpassed by synthesizing a new class of material known as "nanocrystalline diamond" (NCD) films. The nanocrystalline diamond films can be grown by altering the CVD process [57]. Unlike MCD, NCD films consist of small grains on the order of 20-50 nm and a low surface roughness of ~20 nm. Recently, "ultra-nanocrystalline diamond" (UNCD) films having smaller grain size (3-5 nm) than NCD have been developed [58]. The growth of NCD/UNCD films opened a wide window of applications ranging from tribology, MEMS, optics, RF applications and field emission devices [59-62].

3.2. Substrate Pretreatment for the Growth of Diamond Films on Non-Diamond Substrates

Diamond films can be deposited on non-diamond substrates only when the substrates can readily carburize. As all substrates do not form carbide when exposed to the carbon containing precursor gas, a specific sample preparation known as “seeding” is required. Seeding incorporates nucleation sites on the substrate, thereby promoting the growth of diamond films. It can be done by: 1) mechanical scratching of the substrates by diamond micropowder [63], 2) ultrasonication of the substrates in a diamond nanopowder suspension [63], 3) diamond photoresist suspension (DPR) [64], and 4) bias enhanced nucleation (BEN) method [65-67]. When the surfaces are mechanically abraded, the uniformity of the films is poor correspondingly the deposited films are rough due to the scratches induced during abrasion. Due to manual scratching, the nucleation densities vary largely across the sample surface and between the samples. Ultrasonication of the substrates in diamond nanopowder suspension can overcome the problems due to mechanical seeding and can improve the uniformity. But, it is difficult to implement the ultrasonication method if the underlying substrate has features such as thin membranes, or high aspect ratio needles and ultra small features that might be damaged during the actual sonication process. Diamond photoresist (DPR) method may suggest an alternative technique to enhance the nucleation density. Bias enhanced nucleation technique is yet another method of nucleation to produce uniform seeding through out the substrate. Unfortunately, BEN cannot be implemented if the substrate is electrically insulating. *James E. Butler et al.,* at naval research laboratories (NRL) implemented a nucleation process known as *"Rotter's* method*"* of seeding. In this approach, the substrates are initially exposed to CH_4/H_2 plasma followed by the ultrasonication in a diamond nanopowder suspension. The plasma exposure can clean the silicon surface and also etch any native oxide present. Unlike wet etch of silicon in BOE, the in-situ etching provides no subsequent exposure of the wafers to the atmosphere prior to the growth of amorphous carbon layer. It has been reported that the nucleation densities on the order of $10^{12}/cm^2$ can be achieved by this technique [68]. Table 3.1 shows the nucleation densities obtained from various methods.

Table 3.1 Effect of Seeding Method on Nucleation Density

Method of Seeding	Nucleation Density(/cm^2)
Mechanical scratching	10^6-10^7 [63]
Ultrasonic polishing	10^6-10^{10} [63]
Diamond Photoresist suspension	10^{11} [64]
Bias Enhanced Nucleation	10^{10}-10^{15} [65-67]
Pre-plasma exposure	10^{12} [68]

3.3. Selective Nucleation of Substrates

In all of the above mentioned methods, seeding is done through out the substrate. Therefore, when the substrates are exposed to the deposition conditions, diamond films grow completely on the substrate surface. But certain applications might require selective deposition of diamond films. As diamond films need an initial nucleation layer to grow on non-diamond substrates, selective nucleation is carried out by first coating the wafer surface with a diamond loaded photoresist, followed by lithography to define the desired pattern. Development of the photoresist results in leaving the diamond seeds only at the desired regions on the wafer surface. Therefore, diamond films grow at these nucleation sites and forms a continuous film representing the pattern on the substrate. Selective nucleation can also be carried out by fully seeding the wafer in diamond slurry by ultrasonication followed by lithography and etching of the diamond seeds from unwanted regions to define the desired features. When those wafers are exposed to the growth conditions, diamond films can be deposited selectively only in the seeded regions.

3.4. *Cyrannus I* Large Area Microwave Plasma Enhanced Chemical Vapor Deposition (MPECVD) Reactor

MPECVD is the most widely used technique to grow diamond films. Typically all microwave CVD reactors are equipped with a 2.45 GHz generator head. Microwaves have shorter wavelengths or higher frequencies and therefore can produce high density plasma. In a MPECVD reactor, the growth of high quality diamond films are ensued at relatively high pressure and operating temperatures. The cross-section of the commercial plasma source is used in this research is shown in Figure 3.1. Being an electrodeless deposition, the films produced can be free of contamination. The plasma generated by microwaves is stable for a long time.

$$E_{max} = (qe)^2/8\pi^2 f^2 m \quad (3.1)$$

where E_{max} - maximum ion energy, q- ion charge, m- mass of ion and f- frequency

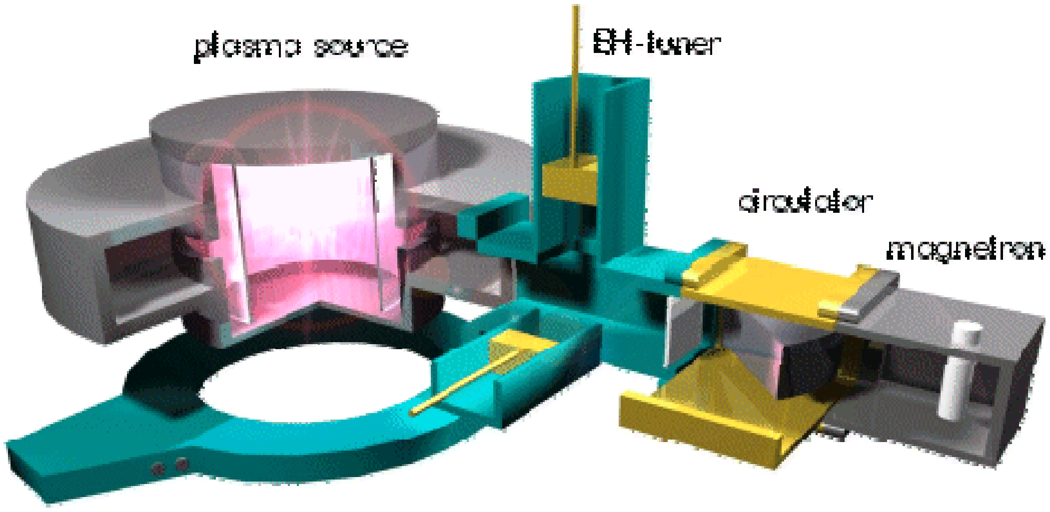

Figure 3.1 Cross-Section Geometry of a *Cyrannus I Iplas* Plasma Source [69]

In this research, Nanocrystalline diamond films have been grown by the microwave plasma enhanced chemical vapor deposition (MPECVD) method in a *Cyrannus I Iplas* reactor. The *Cyrannus I Iplas* system (shown in Figure 3.2) has a 6" plasma source equipped with a 6 kW microwave generator that can produce high density uniform plasma up to 100 mm in size. A manual E-H tuner is used to adjust the plasma density. A graphite heater assembled inside a circular molybdenum substrate holder can be used to heat the substrates up to 800° C. The substrate temperature can be controlled ± (1 to 2°) C using a closed-loop heater controller while the process pressure is controlled by a throttle valve.

Figure 3.2 *Cyrannus I Iplas* Microwave Plasma Enhanced Chemical Vapor Deposition System

3.5. Growth Mechanism of Nanocrystalline Diamond Films

The drastic reduction in the grain size of the diamond films from several microns to few nanometers by changing the gas chemistry suggests that the growth mechanism of nanocrystalline diamond films is different from conventional CVD diamond films. Methyl radicals (CH_3) and acetylene molecules (C_2H_2) are the dominant species in the growth of conventional CVD films using CH_4 and H_2 gas chemistries [70]. NCD films are typically grown in 1% CH_4, with or without 1% H_2 and 98% or 99% Ar. Reduction in the hydrogen concentration from 99% to 1% reduces the grain size of the diamond from several microns to few nanometers. The phase-pure nanodiamond films were grown from a gaseous mixture of C_{60}/Ar in microwave plasma CVD with a total argon pressure of 98 Torr, C_{60} partial pressure of 0.01 Torr, a total flow of 100 sccm, and at a microwave power of 800 watts. A C_2 dimer-based growth mechanism that would result in nanocrystalline structure was proposed [71]. In the films deposited using 5% CH_4 and 95% Ar, the C_2 dimers resulted in the inclusion of an amorphous carbon or graphitic carbon [72-74]. Such non-diamond form of carbon was due to the homogenous nucleation resulted from high ratio of hydrocarbon to carbon dimers. But on the other hand, during the deposition of nanodiamond films, heterogeneous nucleation rate ($>10^{10}$ cm^2sec^{-1}) increases due to highly reactive C_2 species, resulting in the smaller grain size of the diamond films [71]. Figure 3.3 shows the schematic of the growth mechanism of nanocrystalline diamond [58]. According to this model, the feed gases methane and argon disassociate and favor the formation of $(C_2H_2)^+$ at a low ionization potential. The positively charged acetylene radical attracts an electron to form a highly reactive carbon dimer and hydrogen. Hydrogen is then desorbed away while the carbon dimers nucleate at the reconstructed surface. As the reaction continues, the number of carbon dimers in the plasma increase and they join the previously hybridized carbon atoms. In this way, a closely hybridized sp^3 network of carbon atoms forms a continuous film of nanocrystalline diamond.

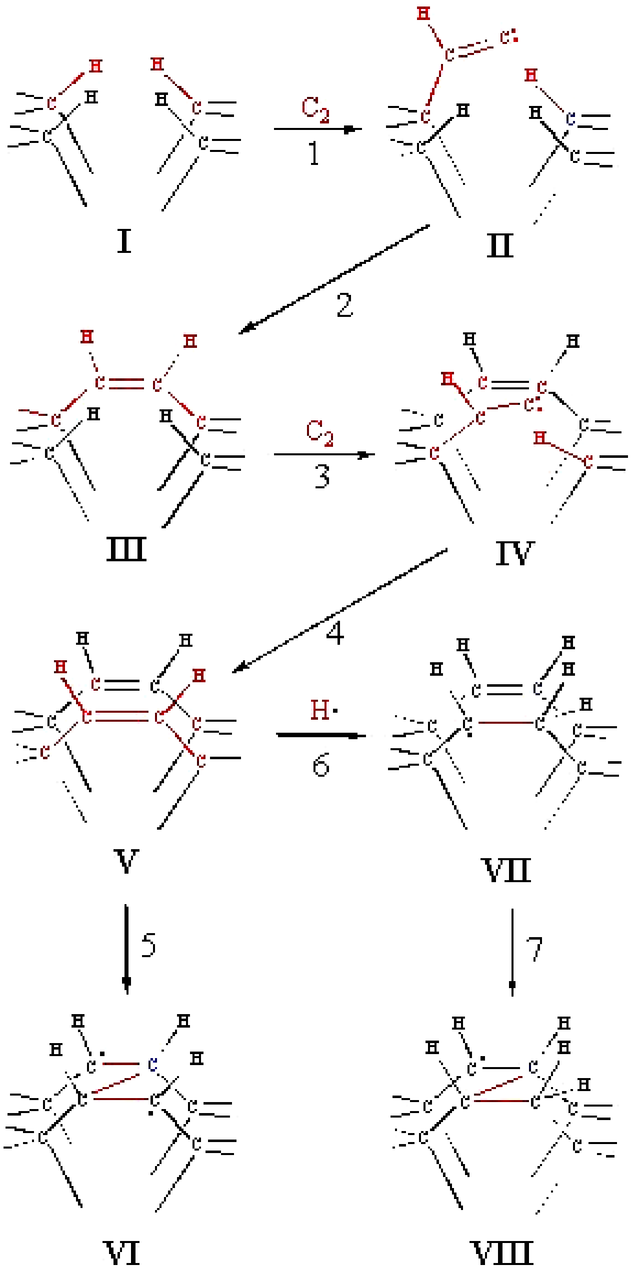

Figure 3.3 Growth Mechanism of Nanocrystalline Diamond [58]

3.6. Experimental Study on the Nucleation Methods

Through out this research, the seeding was implemented by ultrasonic polishing of the samples in diamond nanopowder slurry. During ultrasonication, fine powders (4-5 nm) of diamond suspended in acetone or methanol scratch the surface of the wafer. These diamond seeds are held to the substrate by weak *Vander walls* forces of attraction. Typically, the ultrasonic polishing was carried for 20 minutes, followed by an ultrasonic cleaning in methanol for 40 minutes. In this study, some of the samples were exposed to the growth conditions for 30 minutes prior to the ultrasonication. The process conditions for the growth were: CH_4-0.5%, H_2-1%, Ar-98.5%, total gas flow- 800 sccm, M. W. power-1.8 kW, pressure-135 Torr, substrate temperature-750° C, and deposition time-0.5 hrs. The experimental conditions implemented during the seeding are shown in Table 3.2.

Table 3.2 Experimental Conditions for Seeding With and Without Plasma Exposure

	Acetone + diamond nanopowder	Methanol + diamond nano powder	Nucleation Density (cm^{-2})
Without Plasma Exposure	20 min seeding	20 min seeding	10^8
With Plasma Exposure (30min)	20 min seeding	20 min seeding	10^8

A batch of four samples with two of them exposed to the plasma for 30 minutes, and the remaining two without any plasma treatment, were ultrasonicated in diamond nanopowder slurry. The plasma treated samples were exposed to the above indicated growth conditions. The ultrasonication was carried for 20 minutes in a *Branson* ultrasonic generator followed by the ultrasonic cleaning. SEM micrographs of the samples with and without the plasma exposure and after a 30 minute growth are shown in Figure 3.4. A nucleation density on the order of ~10^8 cm^{-2} was achieved on the samples.

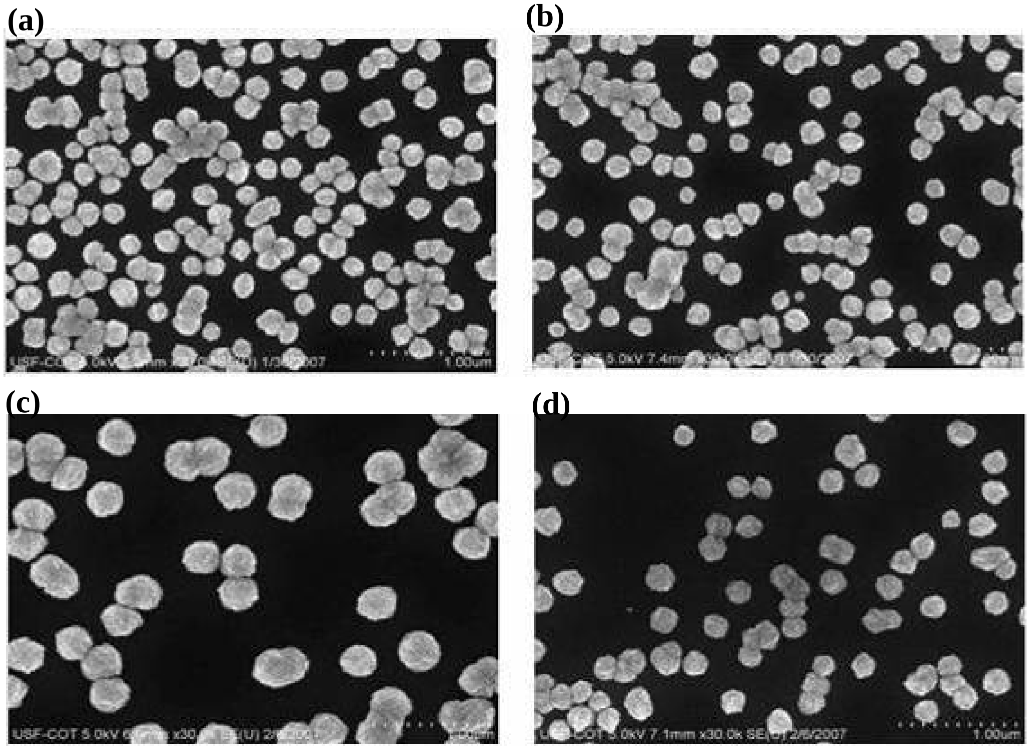

Figure 3.4 Effect of Plasma Treatment on Nucleation Density After Ultrasonicating for 20 Minutes (a) Without Plasma Exposure in a Mixture of Acetone and Diamond Nanopowder Slurry (b) Without Plasma Exposure in a Mixture of Methanol and Diamond Nanopowder Slurry (c) With Plasma Exposure in a Mixture of Acetone and Diamond Nanopowder Slurry (d) Mixture of Methanol and Diamond Nanopowder Slurry

Unlike the *Rotter's* nucleation process [75], which can yield higher nucleation densities after the plasma treatment, in this study, it was observed that the plasma exposure of the samples prior to the growth has not enhanced the nucleation densities. This could be due to several reasons such as the type of gas chemistry, the gas mixture and the process parameters. In *Rotter's* method of seeding, both deposition of NCD films and plasma exposure were carried in CH_4/H_2 gas chemistry. The plasma exposure was carried at relatively higher methane content than the actual deposition, which results in the deposition of a thin amorphous carbon film. After the plasma exposure and during the subsequent ultrasonic seeding, the diamond seeds embed themselves into this amorphous matrix thereby increase the nucleation density. In the current study, the deposition and plasma treatment were conducted in hydrogen poor gas chemistries with only 0.5% methane and excess argon in the gas mixture. The difference in the process chemistry and the experimental conditions explain the difference in the nucleation densities of this experimental study from *Rotter's* method.

It has been reported by *Nevin N. Naguib* [76] *et al.,* that thin metal interlayer (~ 10 nm) of tungsten can enhance the nucleation density and thereby reduce the surface roughness of the films. The improved nucleation density might be due to the formation of a tungsten carbide layer on the surface. Experiments were conducted to observe if the nucleation density could be improved by depositing a thin interlayer of Titanium (~ 10 nm). Like tungsten, Titanium can also form carbide when exposed to carbon-containing gas mixtures. In another experiment, new slurry was prepared by first combining a homogenous mixture of titanium nanopowder and diamond nanopowder. The slurries were prepared both in methanol and acetone by adding the mixture of two powders.

Table 3.3 shows the experimental matrix using titanium metal as an interlayer, and also with the addition of titanium nanopowder and diamond nanopowder to methanol and acetone.

Table 3.3 Experimental Conditions for Seeding With and Without Interlayer

	Acetone + Diamond Nanopowder	Methanol+ Diamond Nanopowder	Nucleation Density(cm^{-2})
With Titanium Interlayer	20 min seeding	20 min seeding	10^8
With a mixture of Titanium nanopowder and diamond nano powder	20 min seeding	20 min seeding	10^{10}
	40 min seeding	40 min seeding	
	60 min seeding	60 min seeding	

Figure 3.5 shows the SEM micrographs of the samples deposited with a thin titanium interlayer. Although, there was no significant improvement in the nucleation density as compared to the previous experimental results, it can be observed that the samples ultrasonicated in acetone suspension show smaller and a higher number of nuclei than those ultrasonicated in methanol. Unlike tungsten, titanium readily reacts with oxygen in the atmosphere and forms titanium oxide [77]. The formation of oxide does not favor the improvement of the nucleation density.

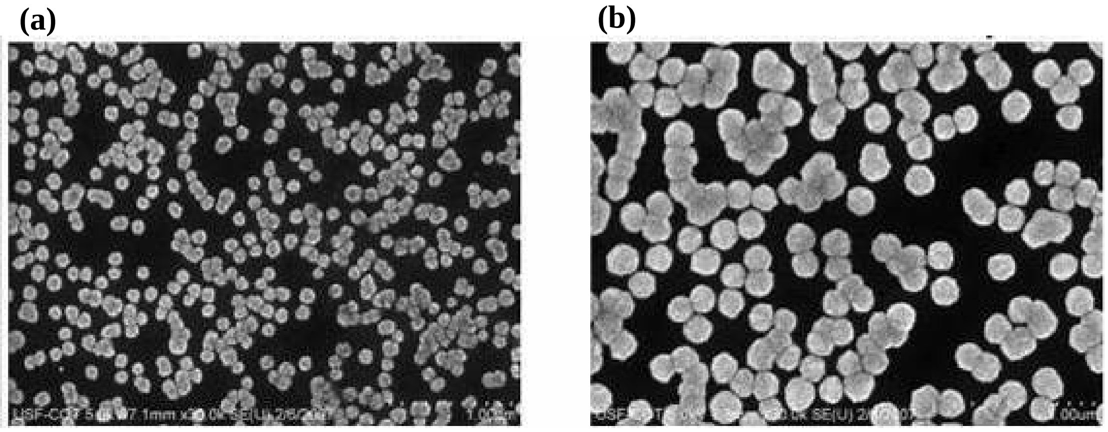

Figure 3.5 Effect of Titanium Interlayer on Nucleation Density After Ultrasonicating for 20 Minutes in (a) Mixture of Acetone and Diamond Nanopowder (b) Mixture of Methanol and Diamond Nanopowder

It has been reported earlier on the pre-nucleation methods for improving the nucleation density of UNCD films deposited in CH_4/Ar gas chemistry at low substrate temperature (~ 400° C) [78]. It was shown that addition of titanium micropowder during the seeding has resulted in the nucleation densities on the order of 5×10^9 cm^{-2}. The role of titanium powder in improving the nucleation density was not addressed clearly. In the present study, it was observed that the addition of titanium nanopowder enhances the nucleation density of the samples ultrasonicated in both acetone and methanol. The SEM micrographs of the samples are shown in Figure 3.6 through Figure 3.8. It can be observed from these SEM images that a continuous film of nanodiamond was formed on the surface after seeding for 20 minutes when the slurry was prepared using acetone. Few voids can be observed on the samples treated in methanol slurry. By increasing the ultrasonic polishing time to 1 hour, the films cover the voids and results in a continuous film.

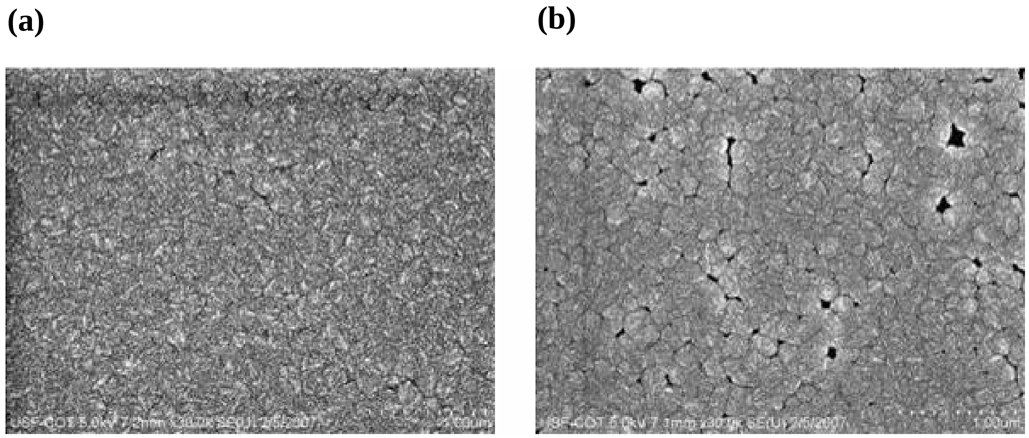

Figure 3.6 Surface Morphology of the Films After Ultrasonicating for 20 Minutes in (a) Mixture of Titanium Nanopowder, Diamond Nanopowder and Acetone (b) Mixture of Titanium Nanopowder, Diamond Nanopowder and Methanol

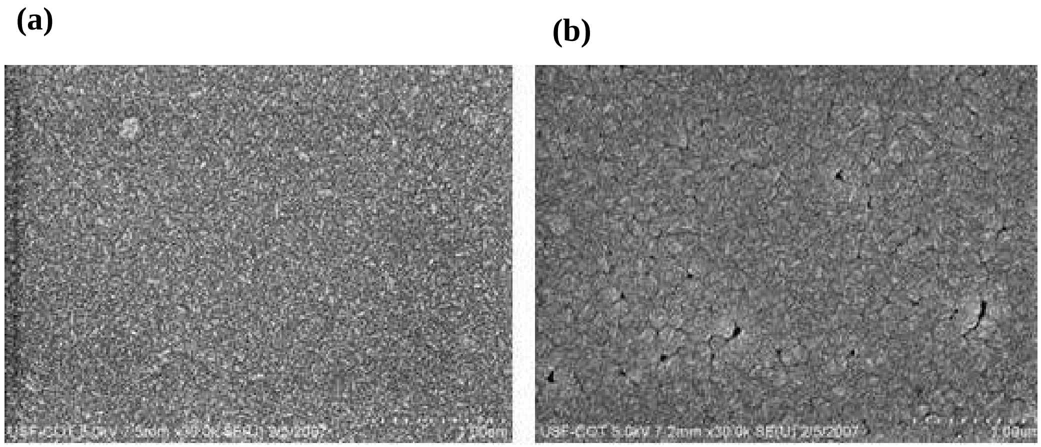

Figure 3.7 Surface Morphology of the Films After Ultrasonicating for 40 Minutes in (a) Mixture of Titanium Nanopowder, Diamond Nanopowder and Acetone (b) Mixture of Titanium Nanopowder, Diamond Nanopowder and Methanol

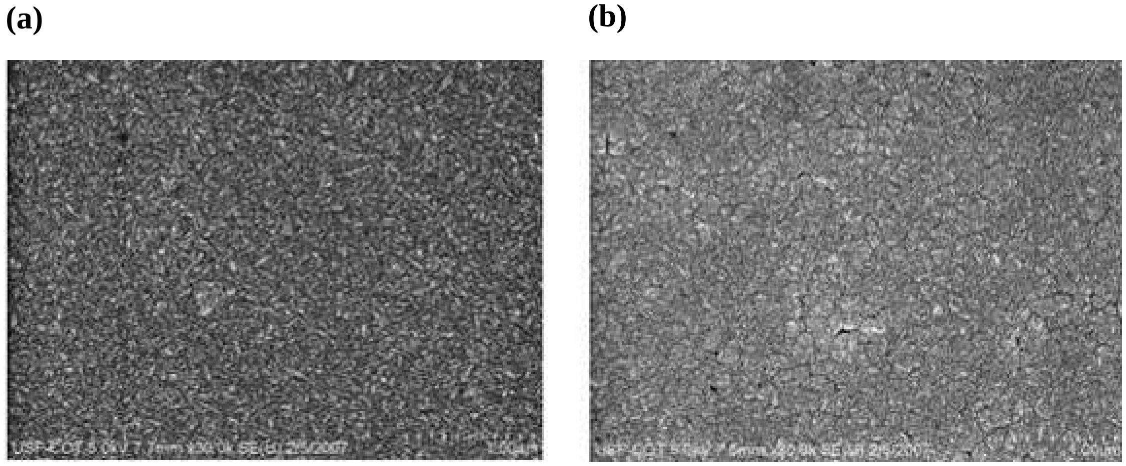

Figure 3.8 Surface Morphology of the Films After Ultrasonicating for 60 Minutes in (a) Mixture of Titanium Nanopowder, Diamond Nanopowder and Acetone (b) Mixture of Titanium Nanopowder, Diamond Nanopowder and Methanol

It can be observed from all the SEM micrographs (Figure 3.4 through Figure 3.8) that the samples treated in slurry consisting of titanium and diamond nanopowder provided a higher nucleation density (at least 10^{10} cm^{-2}). Continuous films were observed on all the samples polished in diamond slurry made using acetone. In general, ultrasonication in acetone suspension has provided slightly higher nucleation sites than the ones seeded in methanol suspension. A slight improvement in the density can be due to the higher dispersion efficiency of the diamond seeds in acetone than methanol [79]. Such a higher nucleation density was not observed on the samples grown with a thin titanium inter-layer (~ 10 nm). The higher nucleation density resulted by seeding in the new slurry was due to a physicochemical surface reaction [80]. The titanium powder activates the surface of the substrate for the incoming carbon dimers to nucleate at the diamond seeds and coalesce into a continuous thin film.

3.7. Effect of Nucleation on the Fabrication of MEMS Cantilevers

The effect of nucleation density on the fabrication of MEMS cantilevers using nanocrystalline diamond films as structural material is discussed in this section [113]. Fabrication of the cantilevers is done by the standard photo-lithography techniques. The process flow is shown in Figure 3.9.

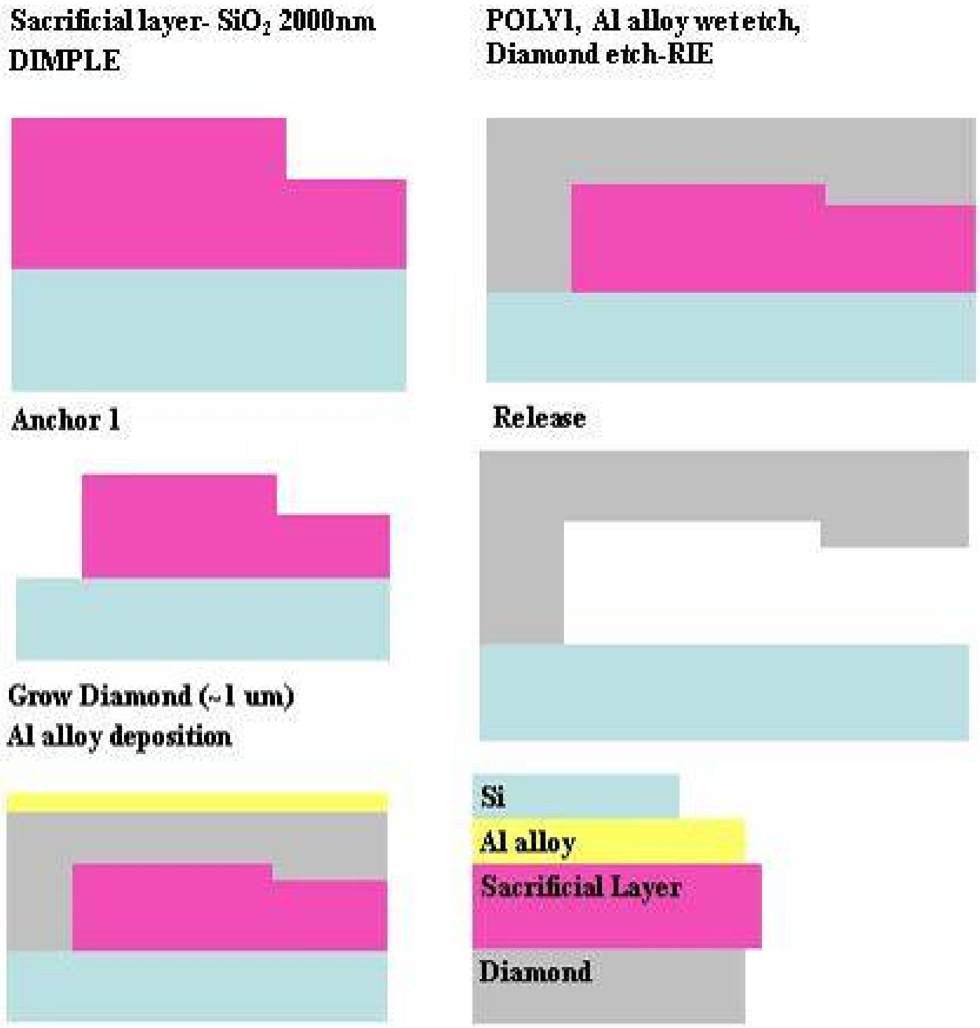

Figure 3.9 Process Steps for the Fabrication of Cantilevers

The fabrication steps involve the growth of a sacrificial SiO_2 layer (2 μm) by LPCVD, followed by a photo-lithography step to form a dimple in the oxide which defines the anchor region. NCD films of thickness ~1 μm were deposited on the patterned substrates. After the growth of NCD films, Al alloy (hard mask) of thickness ~ 300 nm was deposited by sputtering. A photo-lithography step followed by the Al alloy wet etch exposes the unwanted portions of the NCD films. After the reactive ion etch of NCD, the sacrificial oxide was etched in buffered oxide etch (BOE) to release the nanodiamond cantilevers. The SEM micrographs of the cantilevers fabricated using the nanodiamond films treated in a mixture of diamond nanopowder and acetone slurry as well as the mixture of titanium nanopowder and diamond nanopowder in acetone slurry during seeding are shown in Figure 3.10 (a-d), respectively. Due to the lower nucleation density, the nanodiamond films have not deposited uniformly on the anchor pads when the wafers were pretreated in the diamond nanopowder and acetone slurry (Figure 3.10 (a) and (b)). Therefore, during the subsequent sacrificial oxide etch, the structures have detached from the substrate and the cantilevers were found separated from the underlying silicon substrate. The successful fabrication and release of the cantilevers was possible after improving the seeding method. The samples pretreated in a mixture of titanium and diamond nanopowder suspended in acetone has resulted in a uniform and a continuous growth. So, during the subsequent sacrificial oxide etch, the adhesion to the underlying silicon substrate has improved and the cantilevers could hold to the substrate during the release (Figure 3.10 (c) and (d)). It was observed that the Young's modulus and the hardness of the films were ~ (740 ± 80) GPa and (82 ± 12) GPa respectively.

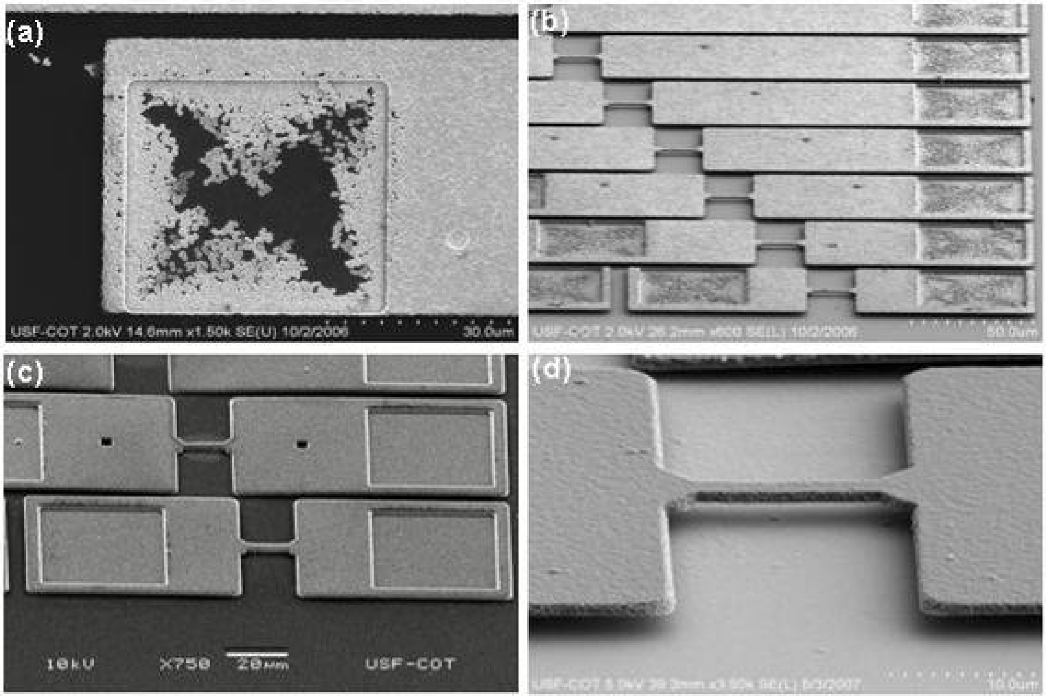

Figure 3.10 SEM Micrograph of Cantilevers (a) and (b) Due to Poor Nucleation Resulting From Seeding in Diamond Nanopowder in Acetone Slurry (c) and (d) Due to Improved Nucleation Resulting From Seeding in Mixture of Titanium Nanopowder and Diamond Nanopowder in Acetone

3.8. Optimized Process Parameters for the Growth of Nanocrystalline Diamond Films

The optimized process recipe for the growth of nanocrystalline diamond films has been achieved by systematically adjusting the process gas compositions, operating pressures, substrate temperatures, and ratio of individual gases. The amount of hydrogen present during the growth affects the properties of the films such as the grain size, grain boundaries and surface roughness. Therefore, the ratio of [Ar]/[H] in the gas composition has to be precisely controlled. The optimized process parameters for the growth of intrinsic NCD films were found to be: CH_4- 0.5%, H_2- 1%, Ar- 98.5%, total gas flow- 800 sccm, M. W. power- 1.8 kW, pressure- 135 Torr, substrate temperature- 750° C.

3.9. Tools and Techniques for the Characterization of Nanocrystalline Diamond Films

The structural properties of NCD films were studied by several analytical and metrology techniques including x-ray diffraction (XRD), atomic force microscopy (AFM), scanning electron microscopy (SEM), transmission electron microscopy (TEM), energy dispersive x-ray analysis (EDAX), Raman spectroscopy, and near edge x-ray absorption fine structure (NEXAFS) studies. Most of these techniques are widely used in characterizing the semiconductor materials. Their operating principles, physics and applications have been extensively covered in the literature [116]. Of the above techniques, Raman and NEXAFS are two spectroscopic methods exclusively employed in characterizing the properties of carbon based materials. As this research is primarily focused on diamond films, it will be useful to understand the operating principles and basics of Raman and NEXAFS Spectroscopy.

3.10. Raman Spectroscopy

Raman spectroscopy is a powerful technique to determine the chemical and structural properties of liquid or solid materials by a simple non-destructive and non-contact method of measurement. It possesses several advantages over other conventional structural characterization techniques such as no sample preparation, rapid and wide measurement range (50 cm^{-1} to 4000 cm^{-1}). It is based on the principle of change in the polarization or electron movement in the material when a laser of a specific wavelength strikes the surface of the sample. When a laser beam strikes the sample, the molecular vibrations result in two types of scattering mechanisms: 1) *Rayleigh* scattering (elastic) and 2) Raman scattering (in-elastic). Due to *Rayleigh* scattering, there is no change in the energy. On the other hand, due to Raman scattering, change in the energy results in anti-stokes-$h(\nu_0+ \nu_n)$ and stokes-$h(\nu_0- \nu_n)$. The change in energy due to the molecular vibration is collected in the Raman spectrum. Figure 3.11 shows the schematic of Raman spectroscopy.

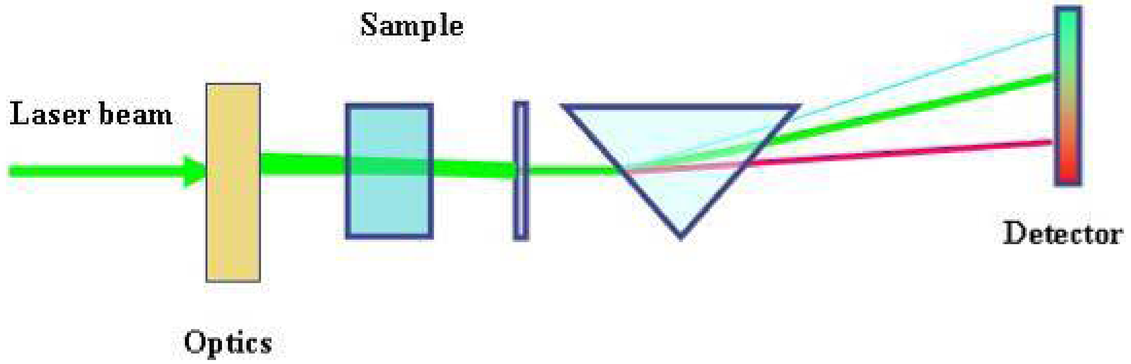

Figure 3.11 Schematic of Raman Spectroscopy

In this research, micro-Raman measurements have been carried in a *Renishaw* 1000 Raman spectrometer using an argon laser (514.5 nm) at a laser power of 24.8 mW and a spot size of 1 µm. The carbon based materials are chemically bonded in *sp, sp^2* or *sp^3* states depending on the type of structure. It is well known that the chemical bonding of graphite and diamond are predominantly *sp*^{2} and *sp*^{3} respectively [81, 82]. As Raman spectroscopy depends on the long-range order of atoms and also due to the wide range Raman scattering for the *sp*^{2} bonded carbon to *sp*^{3} carbon, quantitative information cannot be obtained [86].

The typical Raman spectrum of a single crystal diamond, highly ordered pyrolytic graphite (HOPG), microcrystalline diamond and nanocrystalline diamond are shown in Figure 3.12 (a-d) respectively. It is well known that the Raman spectrum of a single crystal diamond is characterized with a sharp single band at 1332 cm^{-1} corresponding to the *sp*^{3} hybridization of diamond. The Raman spectrum of graphite has two bands representing the dis-ordered carbon (D-band) and graphitic carbon (G-band) at 1350 cm^{-1} and 1580 cm^{-1} respectively. Both the bands are the signatures of *sp*^{2} bonded carbon. A highly ordered pyrolytic graphite (HOPG) consists of hexagonal *sp*^{2} network. The Raman signatures of a microcrystalline diamond has a sharp well distinct feature at 1332 cm^{-1} and a mild background at ~ 1480 – 1550 cm^{-1}, representing the *sp*^{3} and *sp*^{2} characteristics respectively (Figure 3.12 (c)). As MCD consists of large grains, the intensity of the peak at 1332 cm^{-1} is predominant. However, in NCD, as the grain size decreases, a completely different Raman characteristic is observed.

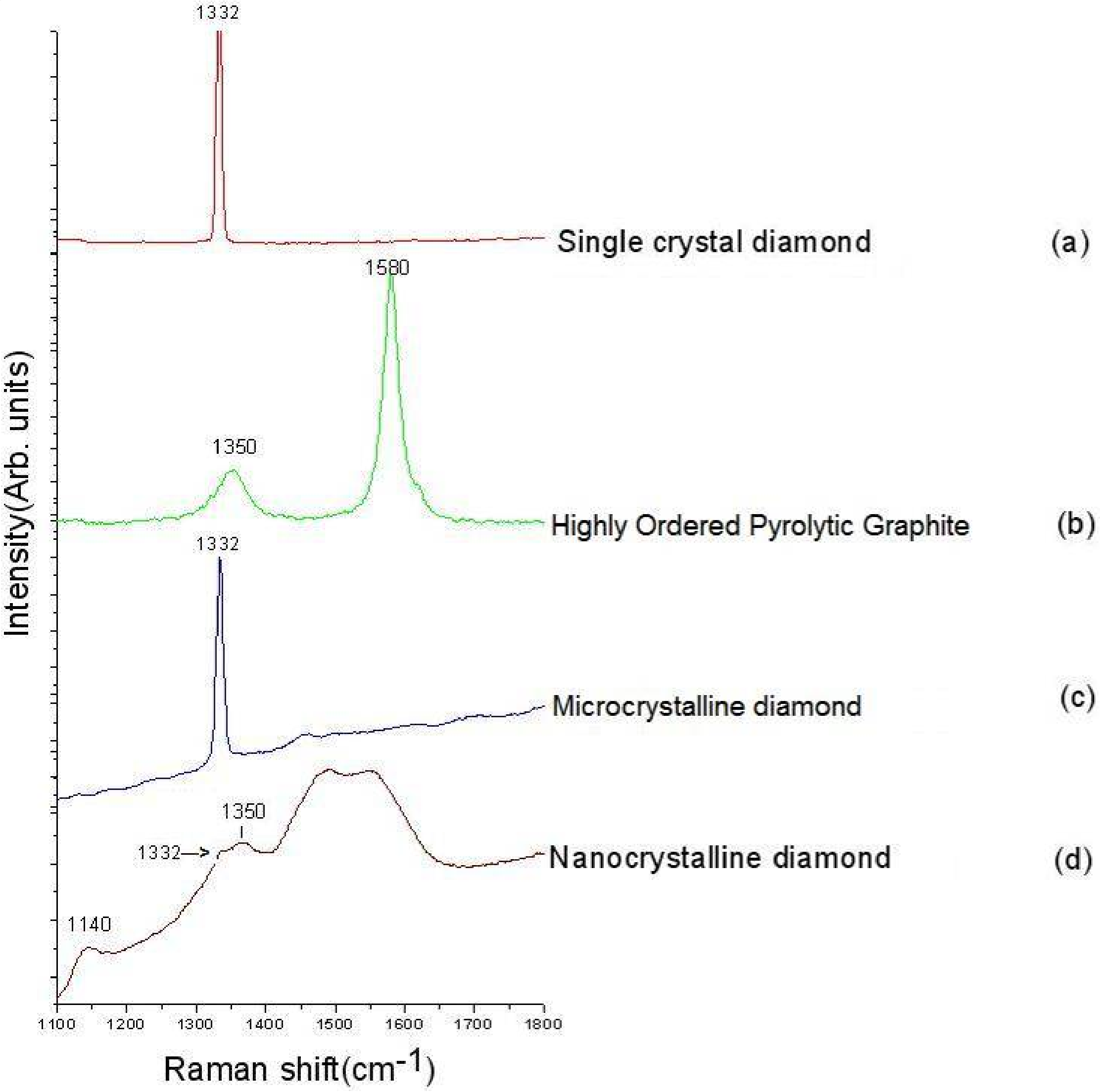

Figure 3.12 Raman Spectra of Carbon Based Materials

Visible Raman being more sensitive (~ order of 50 times) to the sp^2 bonded carbon than is for the sp^3, results in a broader Raman scattering for the former [83]. Hence, the spectra for the NCD films predominantly show the scattering due to sp^2 carbon, even though the majority of the film is sp^3 bonded [84]. Figure 3.12 (d) shows a typical Raman spectrum of NCD film grown in presence of 1% hydrogen in the gas chemistry. The

Raman spectra of NCD films consist of three features: D-band, G-band, and a feature at 1140 cm^{-1} indicating the presence of *trans-polyacetylene* (TPA) states [87-89].

3.11. Near Edge X-ray Absorption Fine Structure (NEXAFS) Spectroscopy

Near edge x-ray absorption fine structure technique was developed in 1980's to study the surface chemistry of low-*Z* molecules. This is a powerful technique to study the nature of chemical bonding in molecules such as hydrogen, carbon, nitrogen and oxygen. NEXAFS specifically selects the atomic species through its *K*-edge and probes its bonds to intra-molecular and surface atoms. It can efficiently detect the existence of various bonds such as hydrocarbons (C-H), C-C, C=C and C≡C bonds. It provides information related to the inter-molecular bond length, orientation, and functional groups attached to the surfaces. The NEXAFS spectra of carbon based materials are dominated by π and σ resonances [85]. The measurements are made in two modes: 1) Total electron yield (TEY) mode and 2) Photon yield (PY) mode. It is based on the principle of absorption of an x-ray photon by a core level atom and a corresponding emission of a photoelectron. The resulting core hole is filled with an electron from a different shell or through an Auger emission process. In TEY mode, the current is monitored through an ammeter while in the PY mode the photon count is monitored.

Typical NEXAFS spectra of a single-crystal diamond and a HOPG reference sample are shown in Figure 3.13. The NEXAFS spectra of HOPG sample is characterized by a peak at 284.5 eV corresponding to π* resonance. A single crystal diamond is characterized by a peak at 289.5 eV corresponding to σ* resonance and a second order band gap of diamond at 302.5 eV.

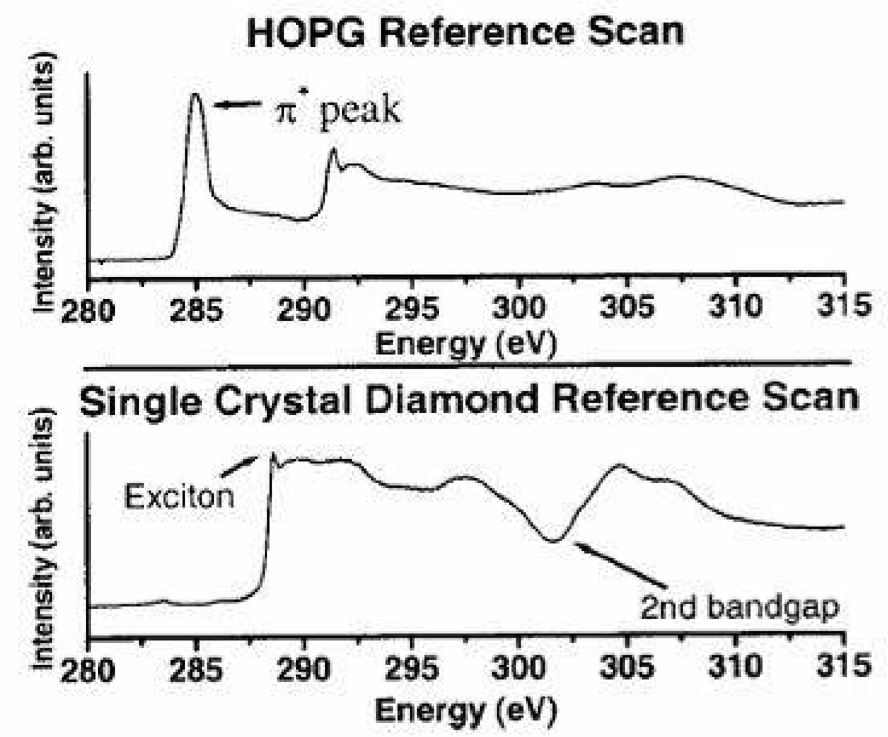

Figure 3.13 NEXAFS Spectra of Single Crystal Diamond and HOPG Reference Sample [113]

Figure 3.14 shows the *HERMON* beam line at the *Syncrotron Raidation Center, University of Wisconsin, Madison* and the test chamber [117] for conducting the NEXAFS measurements.

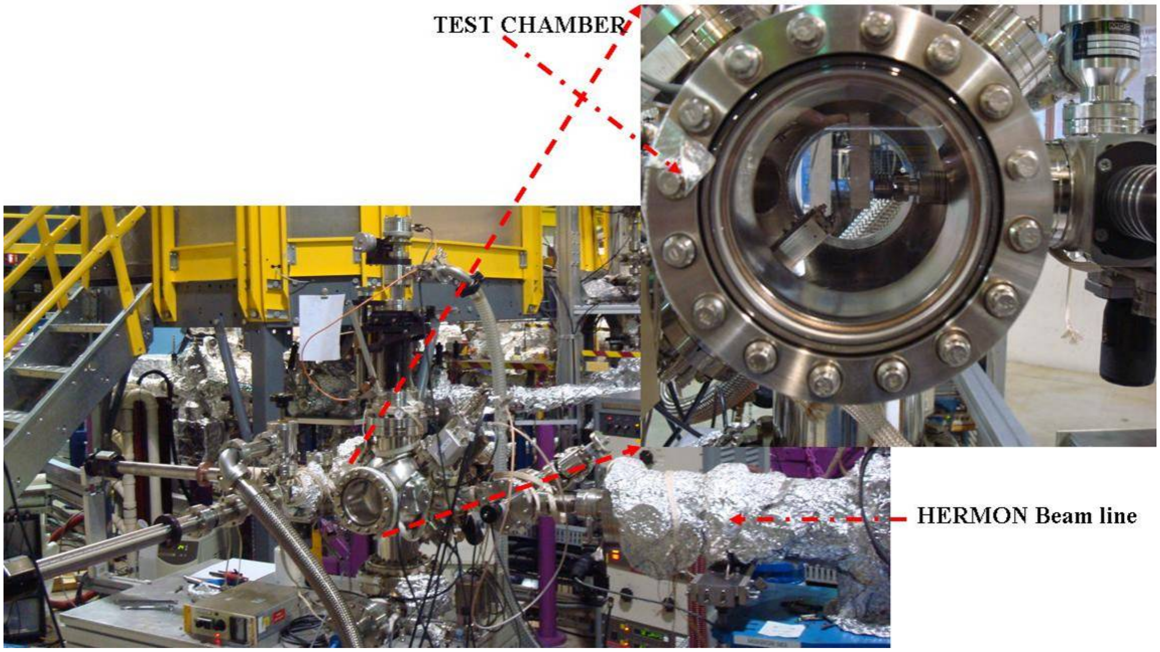

Figure 3.14 HERMON Beam Line at the University of Wisconsin Madison [117]

3.12. Micro-Structural Analysis of Intrinsic NCD Films

The top-view and the cross-sectional SEM images of the NCD films are shown in Figure 3.15 (a) and (b), respectively. The medium and high-resolution SEM images are shown in Figure 3.15 (c) and (d) respectively, where the surface morphology and the grain distribution can be noticed. The top-view SEM micrographs show that the surface of the film is uniform and continuous without any disparities. The SEM images taken at several locations on a 4″ wafer showed similar surface morphology. The growth rate of the films deposited using standard conditions (CH_4- 0.5%, H_2- 1%, Ar- 98.5%, total gas flow- 800 sccm, M. W. power- 1.8 kW, pressure- 135 Torr, substrate temperature- 750° C, deposition time-3 hrs) was approximately 0.17-0.2 µm/hr. Such a low growth rate is reported on all NCD films grown using same gas chemistry in similar CVD reactors.

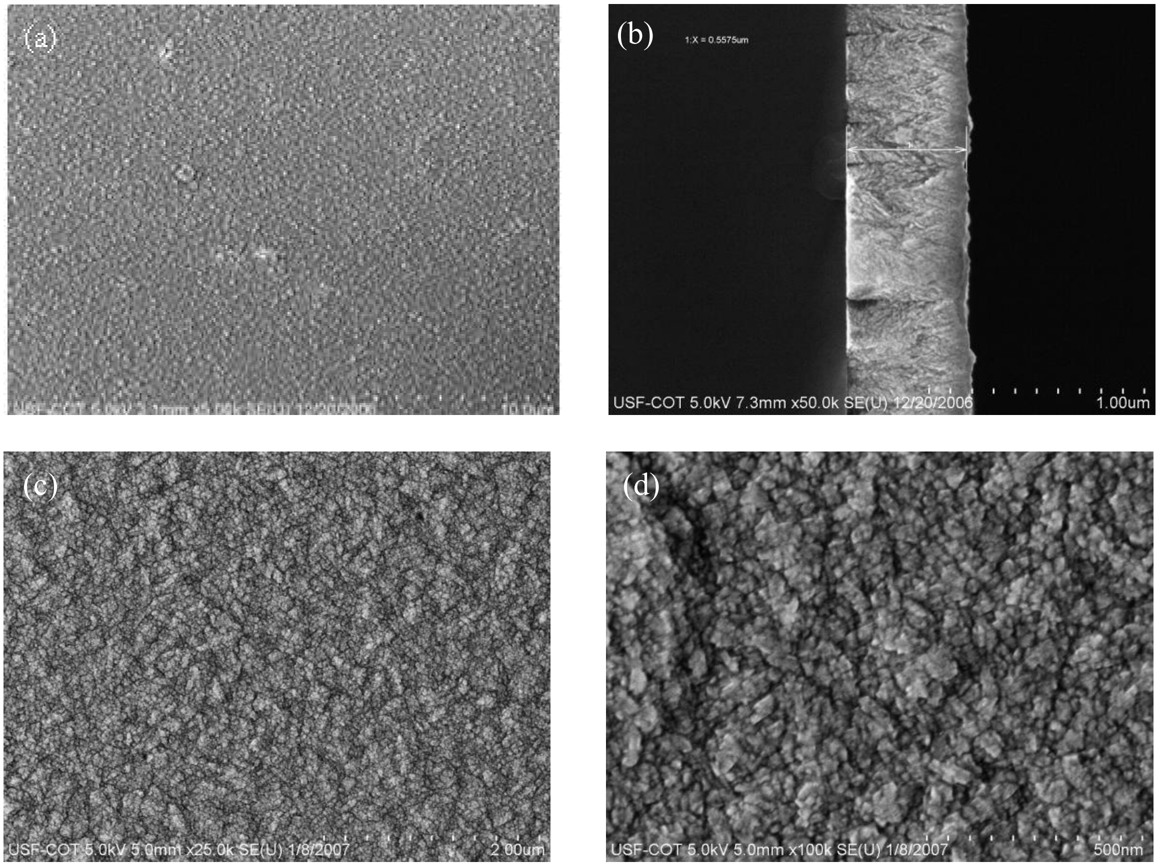

Figure 3.15 SEM Micrograph of Nanocrystalline Diamond Film Deposited Using 1% Hydrogen in the Gas Chemistry (a) Low-Resolution (b) Cross-Section (c) Medium-Resolution (d) High-Resolution

The average surface roughness (R_a) of the films was estimated by atomic force microscopy (AFM). Figure 3.16 shows the AFM micrograph on a 5 μ X 5 μ scan size, where the average surface roughness (R_a) was found to be ~ 12 nm. The surface roughness measured at several locations on a 4″ sample area was consistent. On a 25 μ X 25 μ scan size, the average surface roughness was below ~ 18 nm.

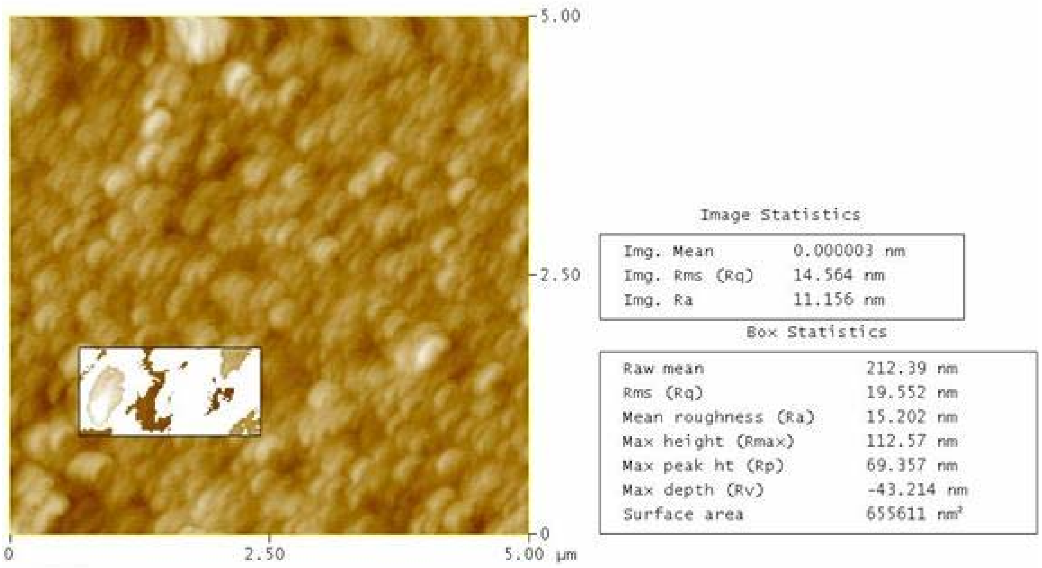

Image Statistics

Img. Mean	0.000003 nm
Img. Rms (Rq)	14.564 nm
Img. Ra	11.156 nm

Box Statistics

Raw mean	212.39 nm
Rms (Rq)	19.552 nm
Mean roughness (Ra)	15.202 nm
Max height (Rmax)	112.57 nm
Max peak ht (Rp)	69.357 nm
Max depth (Rv)	-43.214 nm
Surface area	655611 nm^2

Figure 3.16 AFM Micrograph of Nanocrystalline Diamond Film Deposited Using 1% Hydrogen in the Gas Chemistry

In order to gain understanding of the grain structure at atomic level, the transmission electron microscopy (TEM) studies were conducted. TEM samples were prepared by focused ion-beam (FIB) technique. Figure 3.17 shows the TEM image of intrinsic NCD sample. The electron diffraction pattern is shown in Figure 3.17 (a). The diffraction spectra shows that the film is polycrystalline in nature with (111), (220) and (311) reflections corresponding to the diamond crystal lattice. The low-resolution image (Figure 3.17 (b)) shows dark and bright regions on the sample indicating the contrast between the grains and the grain boundaries. The average grain size was estimated to be ~10 nm. The variation in the grain size was between 10-15 nm. The high-resolution image taken at the same spot clearly shows the atomic planes of the carbon.

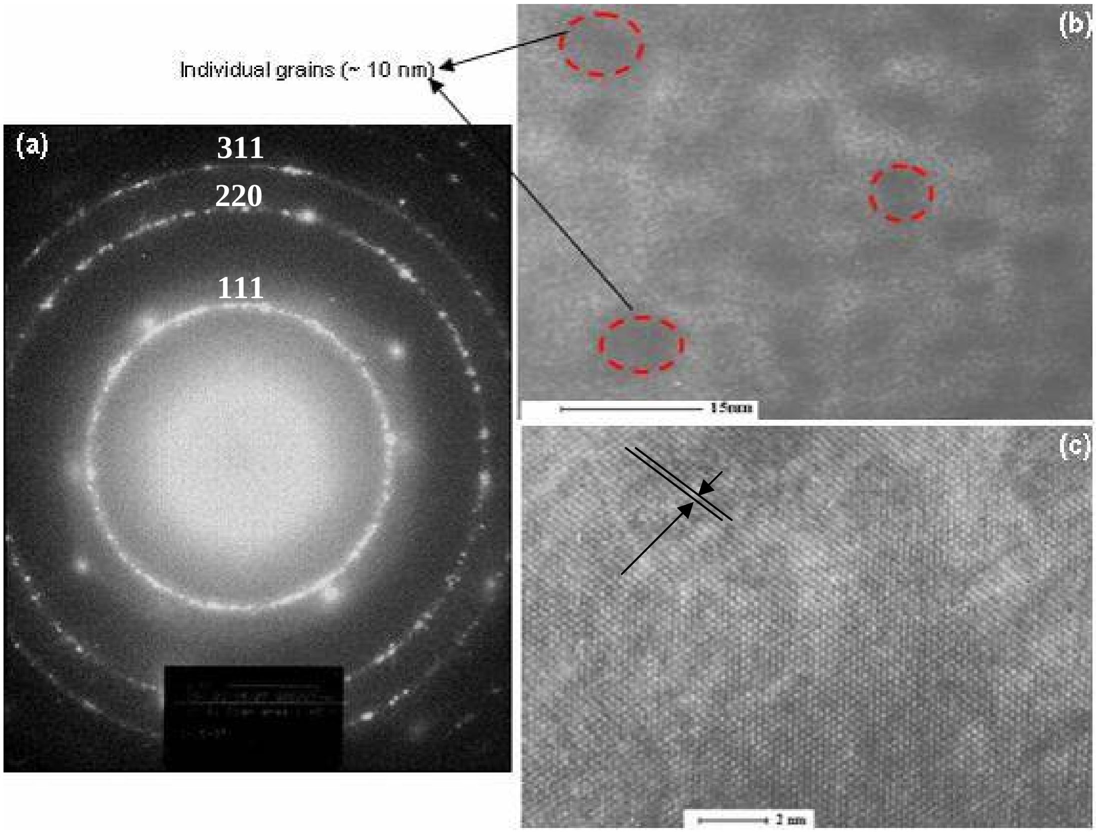

Figure 3.17 TEM Micrographs (a) Electron-Diffraction Pattern (b) Low-Resolution TEM Image (c) High-Resolution TEM Image

3.13. Nitrogen Doping of Nanocrystalline Diamond Films

The intrinsic diamond films are electrically insulating with resistivity on the order of 10^{13}- 10^{16} ohm.cm. Electrical conductivity can be achieved by doping the films during the deposition. The diffusion of dopants into the diamond films is not a practical method of doping as the surface is not diffusive to most of the impurities. Though there are few reports on the ion-implantation of diamond films [90], it is an expensive technique and can damage the surface. Therefore, dopants such as boron (p-type), nitrogen, phosphorous and sulphur (n-type) are incorporated in the gas chemistry during the growth [87]. The most widely used dopants are boron (p- type) and nitrogen (n-type), as these are readily soluble with diamond. It was observed that the quality of the films improve with the incorporation of trace amounts of boron by reducing the point defects. On the other hand, excess concentration of boron promotes graphitization due to the incorporation of boron interstitial sites. Incase of single crystal or microcrystalline diamond, p-type conductivity can be easily achieved. But, it is difficult to obtain n-type conductivity at room temperature in these films as nitrogen forms a deep donor (~1.7 eV). On the other hand, nitrogen forms a shallow donor level (~ 0.4 eV) [91] in NCD/UNCD films and results in high n-type conductivity (~143 Ω^{-1} cm^{-1}). The energy band diagrams of nitrogen doped single crystal diamond and NCD is shown in Figure 3.18.

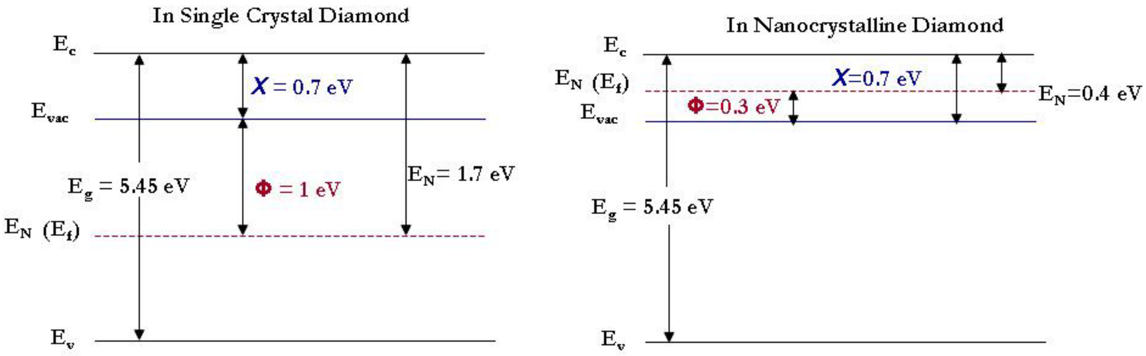

Figure 3.18 Energy Band Diagram of Nitrogen Doped Single Crystal Diamond and Nanocrystalline Diamond

The electron affinity (χ) in both single crystal diamond and NCD is ~ -0.7 eV. As nitrogen forms a donor level at 1.7 eV in single crystal diamond, the resulting work function (Φ) is ~ 1 eV. On the other hand, nitrogen in NCD forms a shallow donor level at 0.4 eV and therefore results in a small and a negative work function. The conduction in the NCD films is via grain boundaries by hopping mechanism [91]. The electrically conductive NCD films have gained special interest in field emission, high power devices and diamond electrodes for bio-sensing applications [91-93].

In the current research, nitrogen incorporated NCD (n-NCD) films have been grown on n-Si (100) substrates using $CH_4/Ar/N_2$ gas chemistry. The optimized process parameters are: CH_4- 1%, Ar- 79%, N_2- 20%, total gas flow- 200 sccm, power- 800 watts, pressure- 100 Torr, and substrate temperature- 750° C. For a deposition time of 3 hours, the thickness of the films was estimated to be approximately 2.7 µm. The electrical contacts were formed by sputtering and patterning a bi-layer of Ti/Au or Cr/Au on n-NCD films. The room temperature electrical conductivity measurements were made in plane by *Jandel* manual multi-position four-point probe tool. The electrical conductivity (measured at 25° C) of these films deposited under standard conditions was found to be approximately 100 $(\text{ohm.cm})^{-1}$.

3.14. In-situ Plasma Diagnostics of NCD Films by Optical Emission Spectroscopy

Optical emission spectroscopy (OES) provides information about the chemical species present in the plasma environment. The relative intensities of the species in the emission spectra suggest the dominant chemical constituents present in the gas chemistry. It has been mentioned earlier that carbon dimers (C_2) are the prominent chemical species in hydrogen poor CH_4/Ar gas chemistries. The color of the plasma is intense lilac green due to the excitation of the argon gas. As the emission spectra of different chemical constituents vary, this technique is useful to detect any impurities present in the reaction chamber. Moreover, significant changes in the spectra can be observed if impurities or dopants are intentionally introduced during the growth. The OES spectra of $CH_4/Ar/H_2$ and $CH_4/Ar/N_2$ plasma chemistries are shown in Figure 3.19 (a) and (b) respectively.

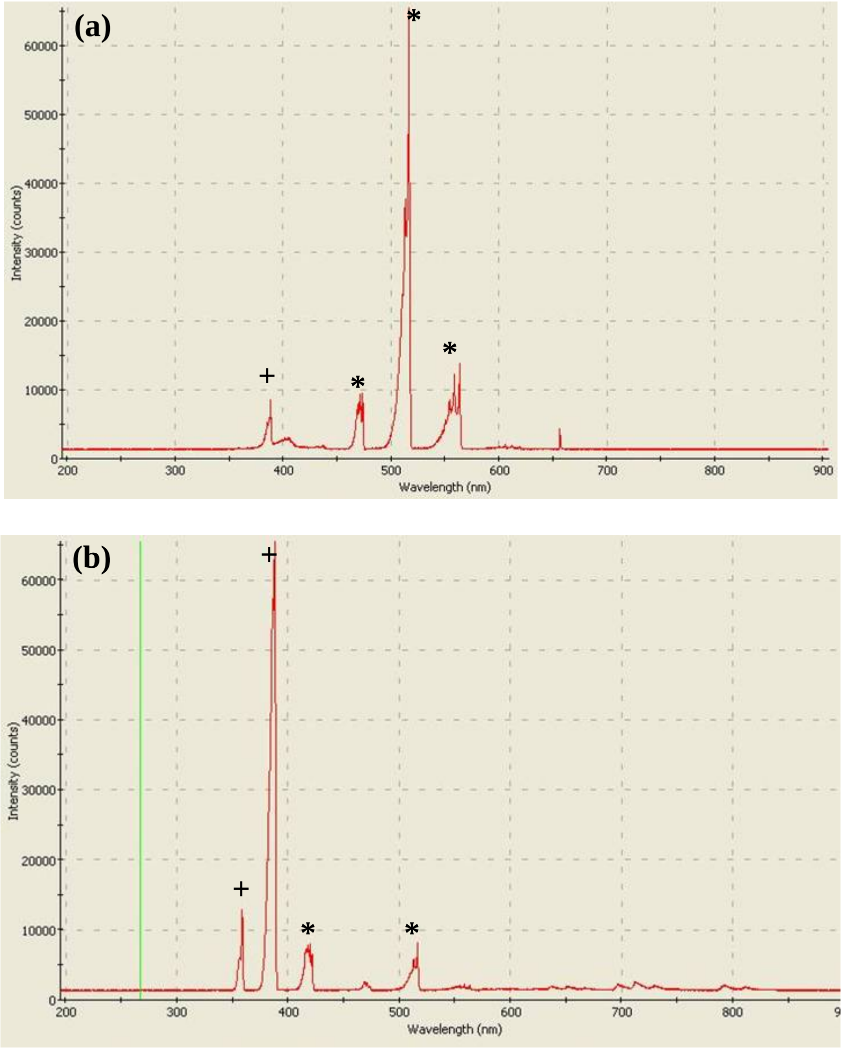

Figure 3.19 Optical Emission Spectra of Plasma Chemistry (a) $CH_4/Ar/H_2$ (b) $CH_4/Ar/N_2$

All the peaks (466, 516 and 556 nm) in Figure 3.19 (a) correspond to the C_2 bands, indicating the high concentration of these species [94]. A trace amount of nitrogen is present in the gas ambience. Hence, a small feature at 388 nm indicating the presence of CN species is observed. When 20% nitrogen (Figure 3.19 (b)) is introduced in the gas chemistry, plasma turns milky white and the intensity of the CN peak increases by several orders, as compared to other peaks. The increase in the CN/C_2 ratio affects the structural morphology and the electrical properties of n-NCD films.

3.15. Structural Analysis of Nitrogen Incorporated Nanocrystalline Diamond Films

A systematic study has been conducted by first growing nitrogen incorporated NCD films with varying nitrogen compositions between 5% and 40% in the total gas mixture. The room temperature electrical conductivities of all the films have been measured and it was observed that the highest electrical conductivity of 100 $(ohm.cm)^{-1}$ was achieved in the films grown using 20% nitrogen in the gas chemistry. Therefore, further study was conducted only on those films. The below section presents AFM, SEM, TEM, and EDAX analysis of nitrogen incorporated NCD films. Figure 3.20 shows the AFM image of n-NCD film. The average surface roughness on a 5 μm X 5 μm scan size was found to be ~ 12 nm. Such a smooth surface indicates the uniform growth of the NCD film deposited by the present technique.

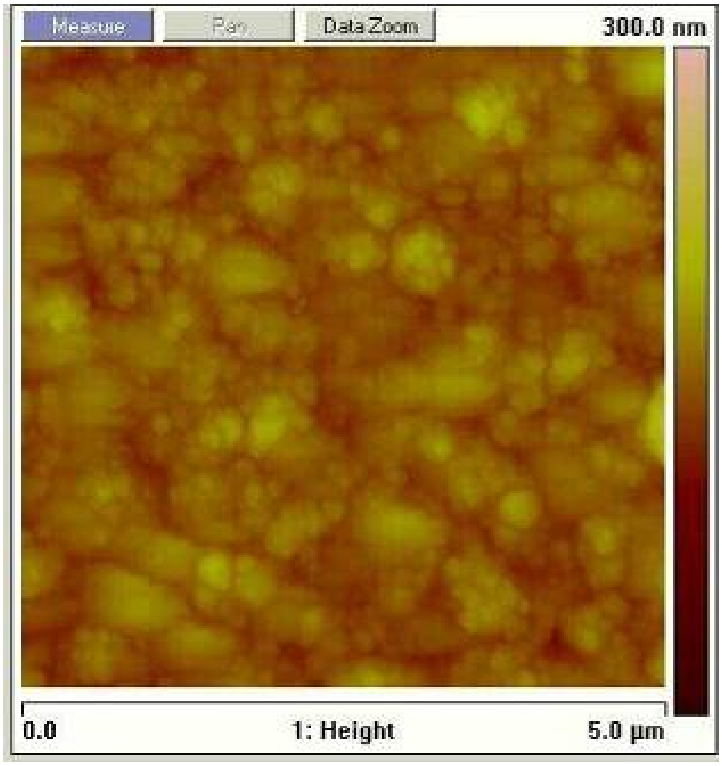

Figure 3.20 AFM Micrograph of n-NCD Film

The top-view and cross-section SEM micrographs of n-NCD films are shown in Figure 3.21 (a) and (b), respectively. It can be observed from the top-view image that the surface of the film is uniform and homogenous. After 15 hour deposition, the thickness of the film was found to be ~ 13.8 µm. It was found that the growth rate of the nanodiamond increased from 0.2 µm/hr to 0.9 µm/hr when 20% nitrogen is added to the gas composition. The CN species produced by the addition of nitrogen do not actively contribute in the growth; instead, they reduce the heterogeneous secondary renucleation rate, and increase the grain size and the growth rate [95].

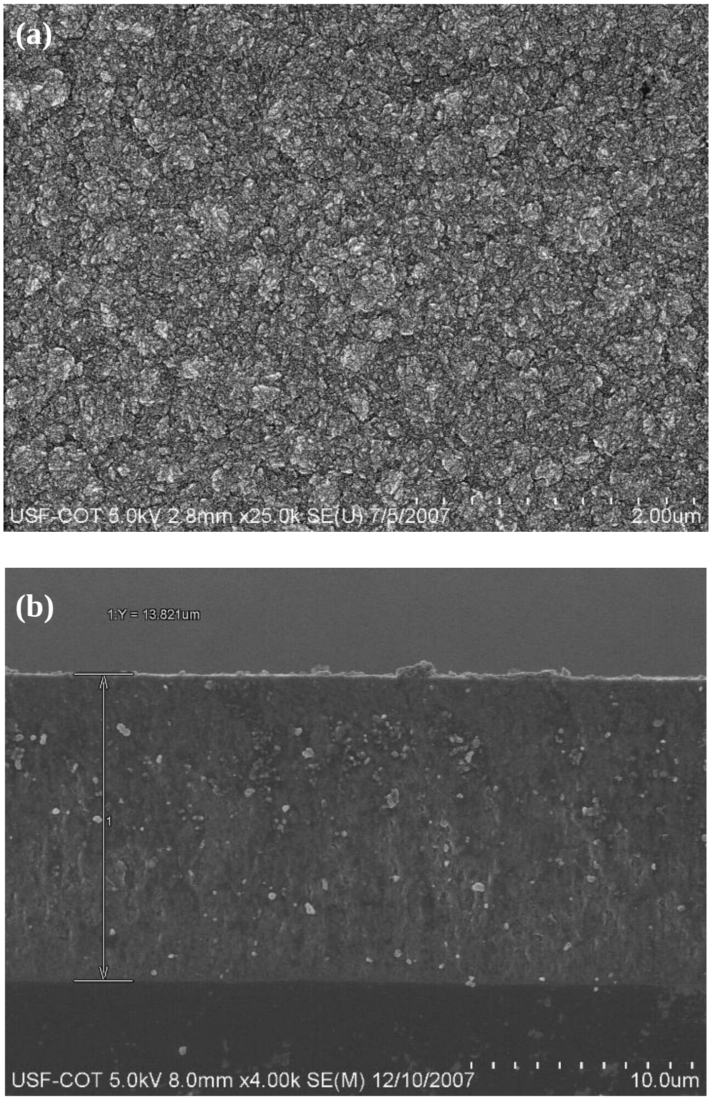

Figure 3.21 SEM Micrograph of n-NCD Film (a) Top-View (b) Cross-Section

The TEM analysis was conducted on n-NCD films for determining the grain size and crystal orientation. The TEM specimens of thickness ~ 100-120 nm were prepared by FIB milling. The high-resolution images of the sample are shown in Figure 3.22 (a-c) respectively. The dark regions of the diamond area in Figure 3.22 (a) indicate the grains, and the bright regions indicate the grain boundaries. It can be noticed from Figure 3.22

(a) that the interface between the underlying silicon substrate and the diamond film is ~ 10 nm. From the high-resolution images, the grain size was estimated to be approximately on the order of 15-20 nm.

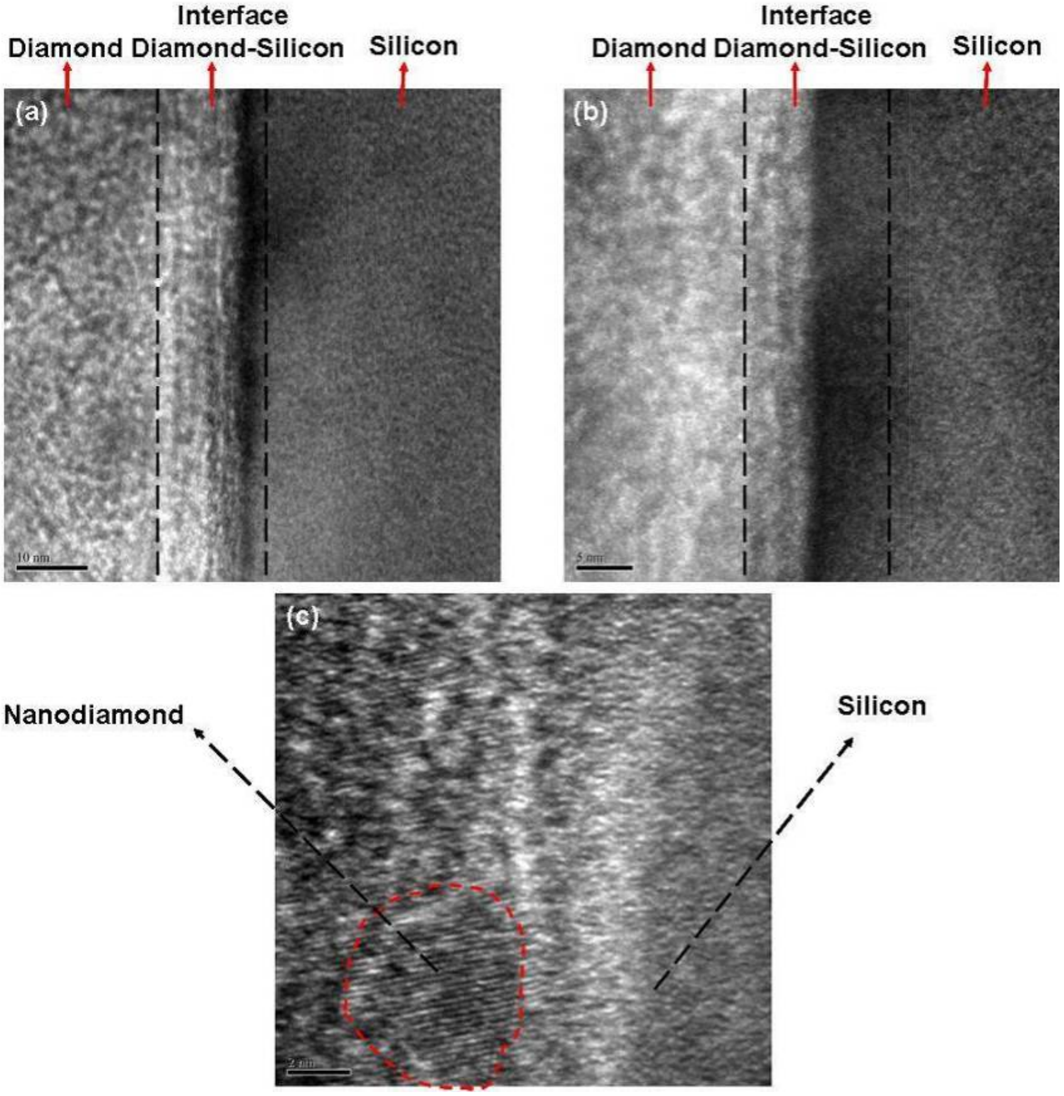

Figure 3.22 TEM Micrograph of Nitrogen Incorporated Nanocrystalline Diamond Film and Interface Between Silicon Substrate and Diamond Film (a) Low-Resolution (b) High-Resolution (c) High-Resolution Showing the Nanocrystalline Diamond Grains

The electron diffraction pattern at different regions on the sample, including silicon, diamond, and the interface between silicon and diamond areas are shown in Figure 3.23 (a-d) respectively.

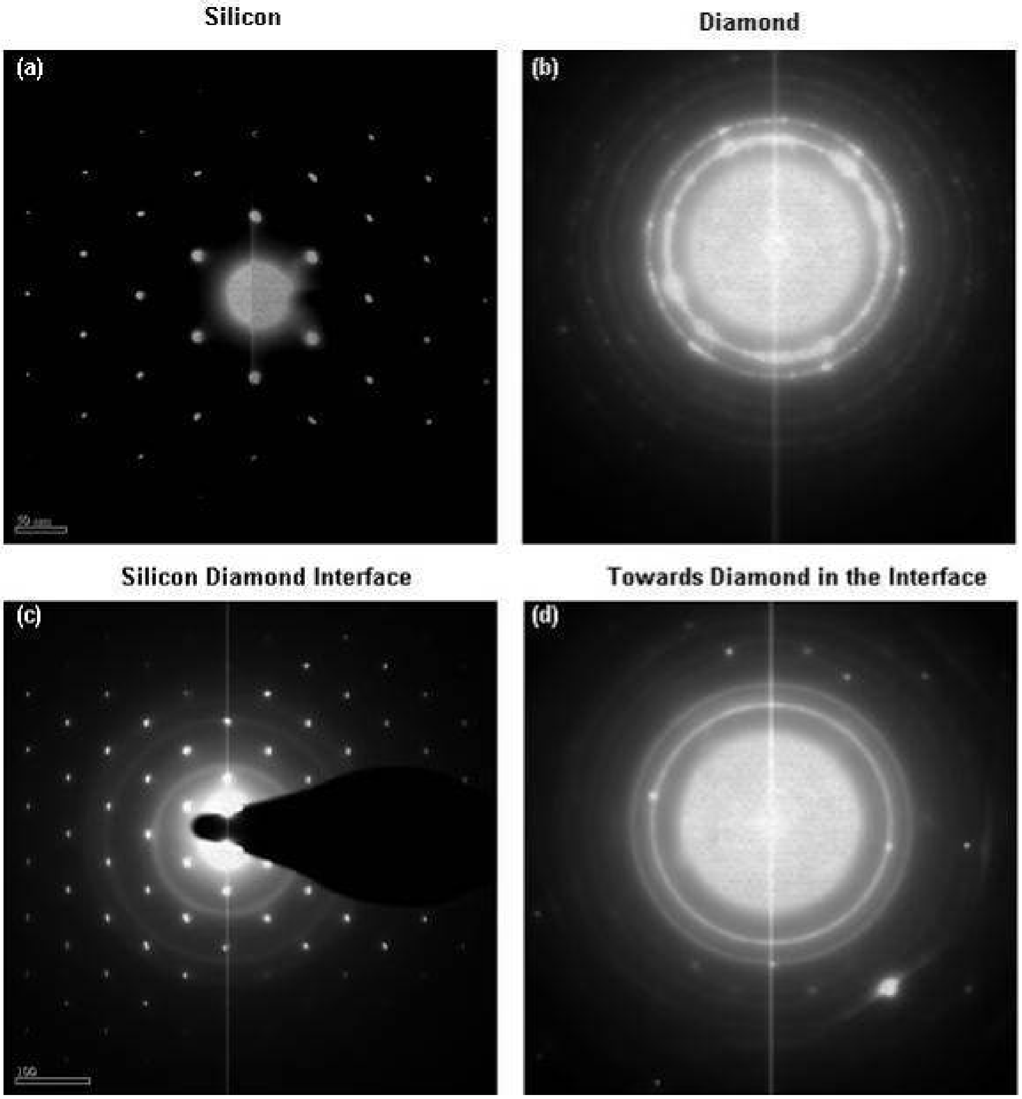

Figure 3.23 Electron-Diffraction Pattern (a) Silicon Substrate (b) Nanocrystalline Diamond Film (c) Interface Between Silicon and Diamond (d) Toward the Diamond Surface Near the Interface

The well defined point reflections in Figure 3.23 (a) indicate the planes of silicon lattice. On the other hand, in Figure 3.23 (b) the circular pattern with point reflections on the *Debye* fringes indicate the polycrystalline nature of the diamond film. The first two fringes from the center of the electron beam represent the (111) and (220) planes of the diamond crystal. Figure 3.23 (c) shows the electron diffraction pattern of the interface between silicon and diamond, where the point reflections of the silicon and the circular patterns of the diamond can be observed. Figure 3.23 (d) shows the electron diffraction pattern of the diamond areas away from the interface, hence well defined circular fringes can be observed prominently.

Figure 3.24 (a) shows the cross-section scanning profile image of the TEM sample. Figure 3.24 (b) and (c) show the line scan images of silicon and carbon spectra. In the EDAX spectra of Figure 3.24 (d), the signatures of elemental silicon and carbon were observed. All these results show that by the addition of nitrogen, the crystalline nature of the NCD is not damaged and the films consist of nanodiamond grains with an average grain size ~ 20 nm.

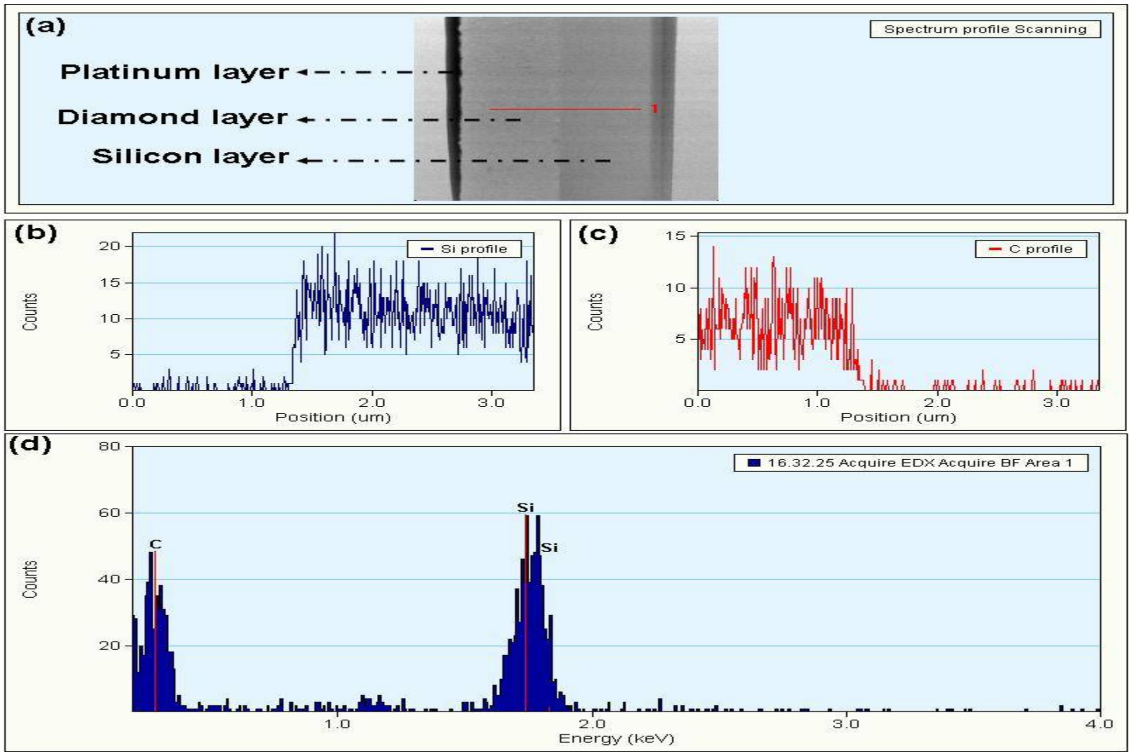

Figure 3.24 Line-Scan Profile Images (a) Cross-Section of the TEM Sample (b) Silicon (c) Carbon (d) EDAX Spectra Showing Silicon and Carbon Peaks

In this section, the visible Raman, NEXAFS and XRD results of the nitrogen incorporated NCD films are discussed. For comparative purposes, the structural analysis of pure NCD film (0% N) is also discussed. The Raman and the NEXAFS spectra of the samples are shown in Figure 3.25 (a) and (b) respectively. The Raman spectra of both intrinsic and conductive NCD films show three important features. The assignment of each of the features has been discussed earlier. It can be observed that when nitrogen is introduced in the gas chemistry, a significant change in the G-band can be observed. As the sp^2 content in the films determine the mechanical and electrical properties, it is important to estimate the amount of sp^2 present.

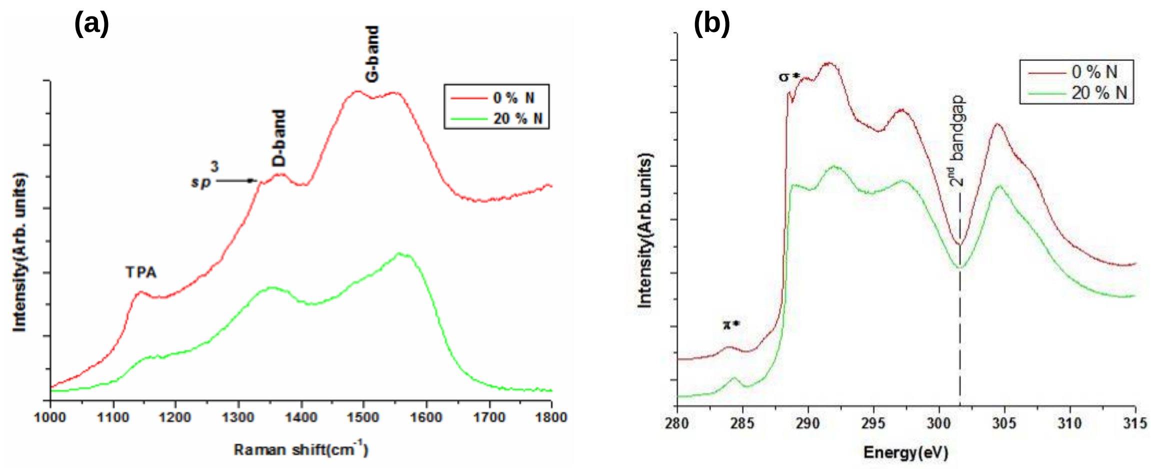

Figure 3.25 (a) Raman Spectra and (b) NEXAFS Spectra of Nanocrystalline Diamond Films Grown Using 0% and 20% Nitrogen in the Gas Chemistry

In the NEXAFS spectra, three features, corresponding to π*, σ* and the second order band gap of diamond, can be observed at ~284.7 eV, ~289 eV and ~302 eV, respectively. The π* and σ* features correspond to the sp^2 and sp^3 bonded carbons, respectively. From the NEXAFS spectra of intrinsic films, a sharp and well defined peak corresponding to σ* bonding can be observed. The π* peak is weak and the FWHM of second-order band gap of diamond is narrow. With the addition of 20% nitrogen in the gas chemistry, the area under the π* peak increased, σ* peak is not as distinct as intrinsic diamond film, and FWHM of the second order band gap increased. These changes in the NEXAFS spectra suggest that the sp^2 content increases with the addition of nitrogen. The fraction of sp^2/sp^3 was estimated by using the following expression.

$$F_{sp2} = \frac{I^{\pi*}_{SAMPLE}}{I^{\pi*}_{REFERENCE}} \frac{I_{REFERENCE}(\Delta E)}{I_{SAMPLE}(\Delta E)} \tag{3.2}$$

where F_{sp2} represents the fraction of *sp*^{2} in the films, $I_{SAMPLE}^{\pi*}$, $I_{REFERENCE}^{\pi*}$ represent the areas of the π* peak of the sample and the HOPG reference. $I_{REFERENCE}(\Delta E)$ and $I_{SAMPLE}(\Delta E)$ represent the remaining area under the spectrum that is contributed by the *sp*^{3} bonded carbon [68]. It was estimated that the films grown without any nitrogen have approximately 7% *sp*^{2} and this fraction has increased to ~ 14% when 20% nitrogen was added in the total gas mixture. Therefore, the nitrogen doped NCD films consists of a considerable fraction (~86%) of *sp*^{3} bonded carbon. With the addition of the deliberate amount of *sp*^{2}, the electrical conductivity of these films increases by four orders.

The x-ray diffraction spectra of pure and nitrogen incorporated NCD films are shown in Figure 3.26. It can be observed that the spectra of both the films represent the diffraction lines of (111), (220), and (311) peaks respectively. The strong match in the diffraction data of both the films further support that by the addition of nitrogen, the damage incurred to the crystal lattice of the diamond is minimal. Table 3.4 and Table 3.5 shows the diffraction data of undoped and nitrogen incorporated nanocrystalline diamond films respectively.

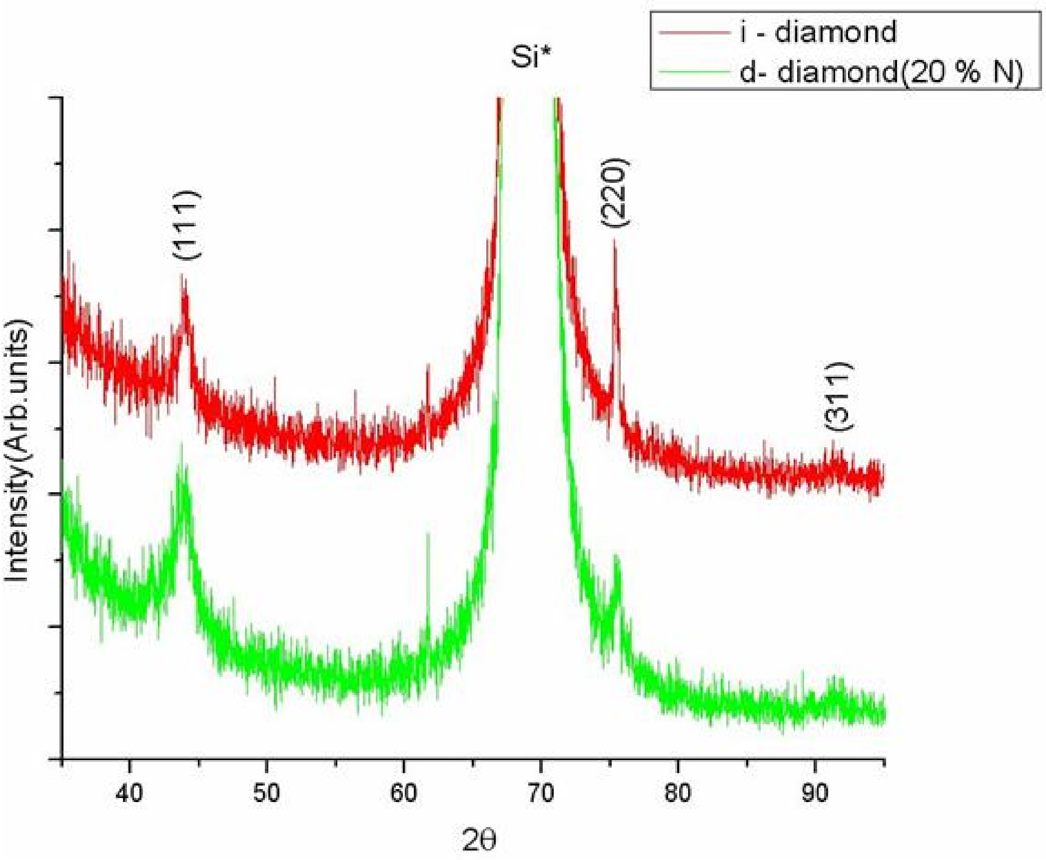

Figure 3.26 X-ray Diffraction Spectra of Undoped and Nitrogen Incorporated Nancorystalline Diamond Films

Table 3.4 XRD Data of Undoped Nanocrystalline Diamond Films

Peak	Position(2θ)	Counts	d-spacing(Å)
(111)	43.9929	32.8	2.058
(220)	75.3532	55.72	1.26
(311)	91.5874	2.95	1.15

Table 3.5 XRD Data of Nitrogen Doped Nanocrystalline Diamond Films

Peak	Position(2θ)	Counts	d-spacing(Å)
(111)	43.5068	39.83	2.08017
(220)	75.592	21.75	1.25691
(311)	91.5674	1.63	1.13

3.16. Electrical Contacts to Nitrogen Incorporated Nanocrystalline Diamond Films

The electrical properties of nitrogen incorporated NCD films were measured by forming suitable electrical contacts to the films. A bi-layer of Ti/Au films were deposited by sputtering and later patterned to form metal electrodes on n-NCD films. The current-voltage properties were measured by making electrical contacts to the front and back side of the dice. Figure 3.27 shows the current-voltage response when the bias voltage was varied from -8 V to + 8 V. The strong linear I-V characteristics indicate that the high quality ohmic contacts were formed on these films [112]. It has been reported that Ti/Au metal electrodes on the boron doped polycrystalline diamond films failed to form ohmic contacts without any post deposition annealing due to the absence of the formation of a carbide layer [96]. Ohmic contacts to phosphorous doped films could not be formed even after annealing the Ti metal contacts; on the contrary they have shown rectification [97].

Before Hydrogen Plasma Treatment

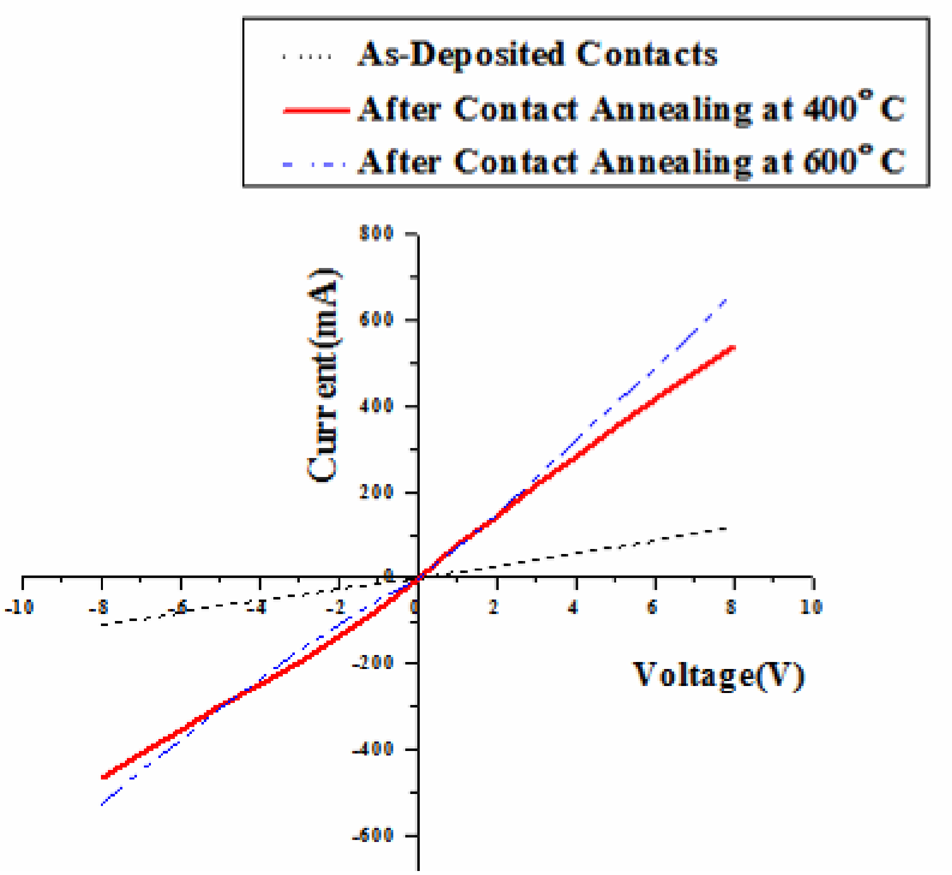

Figure 3.27 Current-Voltage Characteristics of Nitrogen Incorporated Nanocrystalline Diamond Films

In this research, low resistive ohmic contacts could be formed easily on conductive nitrogen doped NCD films, even before annealing. The annealing was done to understand the effect of temperature on the electrical contacts and the contact resistivity. It suggests that the conduction mechanism in the nitrogen and phosphorus doped diamond films is different. The introduction of nitrogen in the diamond films increases the defect density of states in the Fermi level [98]. It can be stated that the defects in these films play an important role in the formation of ohmic contacts.

To further study the role of defects on the type of electrical contact and the electrical conductivity, the as-grown samples were exposed to hydrogen plasma for about 30 minutes prior to the deposition of metal electrodes. It is well known that the surface conductivity of polycrystalline diamond films can be increased by the hydrogen plasma treatment due to "surface transfer doping" mechanism [113, 92, 93, 114]. As polycrystalline diamond films have large grains, higher amount of hydrogen termination and consecutively a greater reduction in the electrical resistivity can be achieved by the plasma treatment. But, the electrical properties of NCD films are different as they have small grains and tight grain boundaries. In fact, it has been reported that the electrical conductivity of pure NCD films has changed only from $10^{-6}\ \Omega^{-1}\mathrm{cm}^{-1}$ to $10^{-8}\ \Omega^{-1}\mathrm{cm}^{-1}$ after hydrogenation [114]. As the electrical conductivity of the n-type NCD films is expected to be due to sp^2 bonded carbon, defects and other impurities [91, 115], the surface conductivity induced by the plasma treatment may be different. The hydrogen plasma treatment is also known to reduce the electron-affinity of the diamond surfaces; thereby the electron emission characteristics can be improved. As one of the applications of the conductive NCD films in this research is to fabricate NCD based field emission devices, therefore, this experimental study is important to know if the field emission properties of nitrogen incorporated NCD films could be improved. Figure 3.28 shows the top-view

SEM of the as-grown (20% N doped) NCD films before and after they were exposed to the hydrogen plasma.

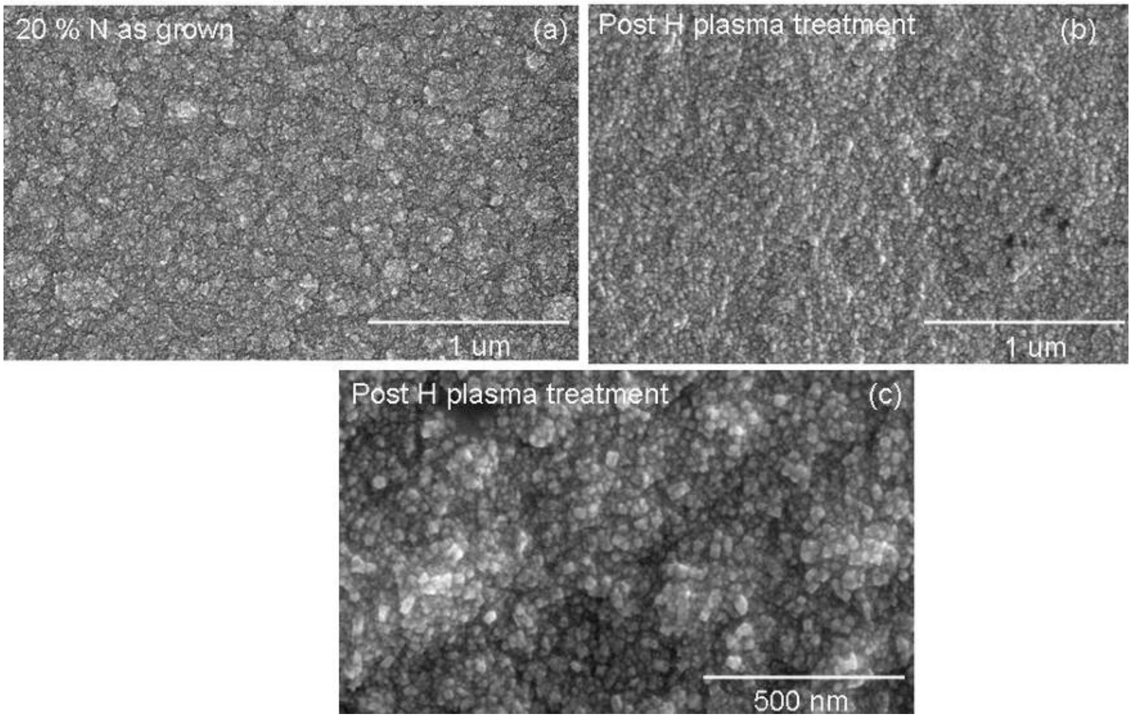

Figure 3.28 Surface Morphology of Nitrogen Incorporated Nanocrystalline Diamond Film (a) as-grown (b) Post Hydrogen Plasma Treated Surface (Low-Resolution) (c) Post Hydrogen Plasma Treated Surface (High-Resolution)

A “cauliflower-like” structure was observed on the as-grown sample (Figure 3.28 (a)), which later disappeared after a subsequent exposure to the hydrogen plasma (Figure 3.28 (b)). After the hydrogen plasma treatment, the crystals of the nanodiamond on the surface of the film were revealed due to the etching of a part of sp^2 bonded surface carbons. The AFM images of the as-grown and hydrogen plasma treated n-NCD films is shown in Figure 3.29 (a) and (b) respectively. The average surface roughness of the as-grown films was before and after the hydrogen plasma treatment was found to be ~ 13 nm and ~ 24 nm respectively. The increased surface roughness is due to the uneven surface morphology, resulting from etching of the surface carbon (*sp*^{2}).

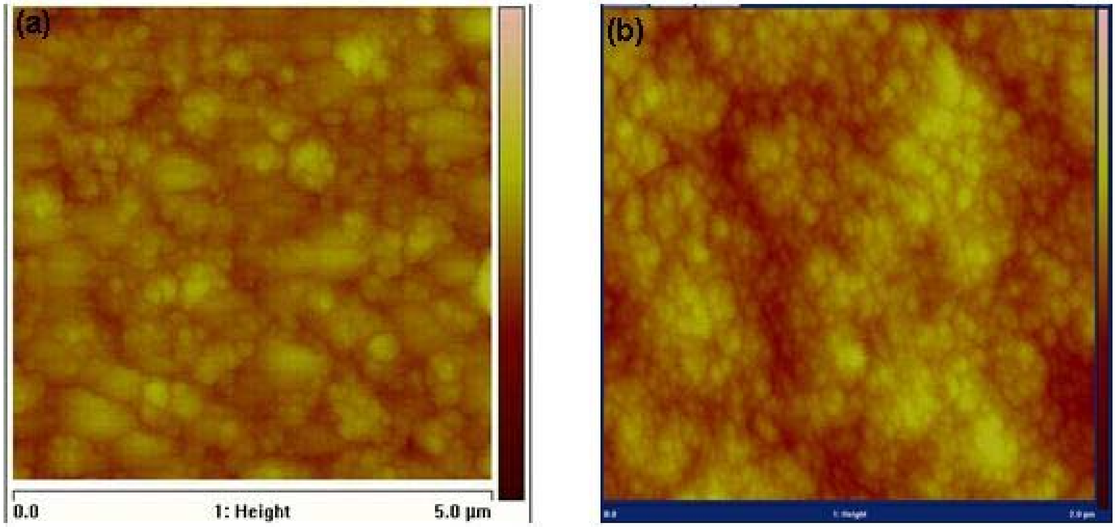

Figure 3.29 AFM Image of Nitrogen Incorporated Nanocrystalline Diamond Film (a) as-grown (b) After the Hydrogen Plasma Treatment

Figure 3.30 shows the visible Raman spectra of both as-grown and hydrogen plasma treated nitrogen incorporated NCD films. The signatures of the Raman bands are identical in both the curves. The important features in the spectra are at ~1145 cm^{-1}, 1348 cm^{-1}, 1486 cm^{-1} and 1564 cm^{-1}, respectively. The features at ~1145 cm^{-1} and ~1480 cm^{-1} indicate the presence of trans-polyacetylene states in the grain boundaries of NCD films [108]. In the as-grown films, the shoulder at ~ 1486 cm^{-1} is more predominant than the plasma treated ones. The amount of TPA states present in the films is related to the presence of hydrogen [109]. As TPA states are unstable at high temperatures, these features disappear when the films are heated to ~1200° C [110]. But in this study, the films were exposed to the hydrogen plasma at relatively lower temperatures (~700°C-750°C). Therefore, the TPA states have not completely disappeared; instead, their relative intensities only decreased.

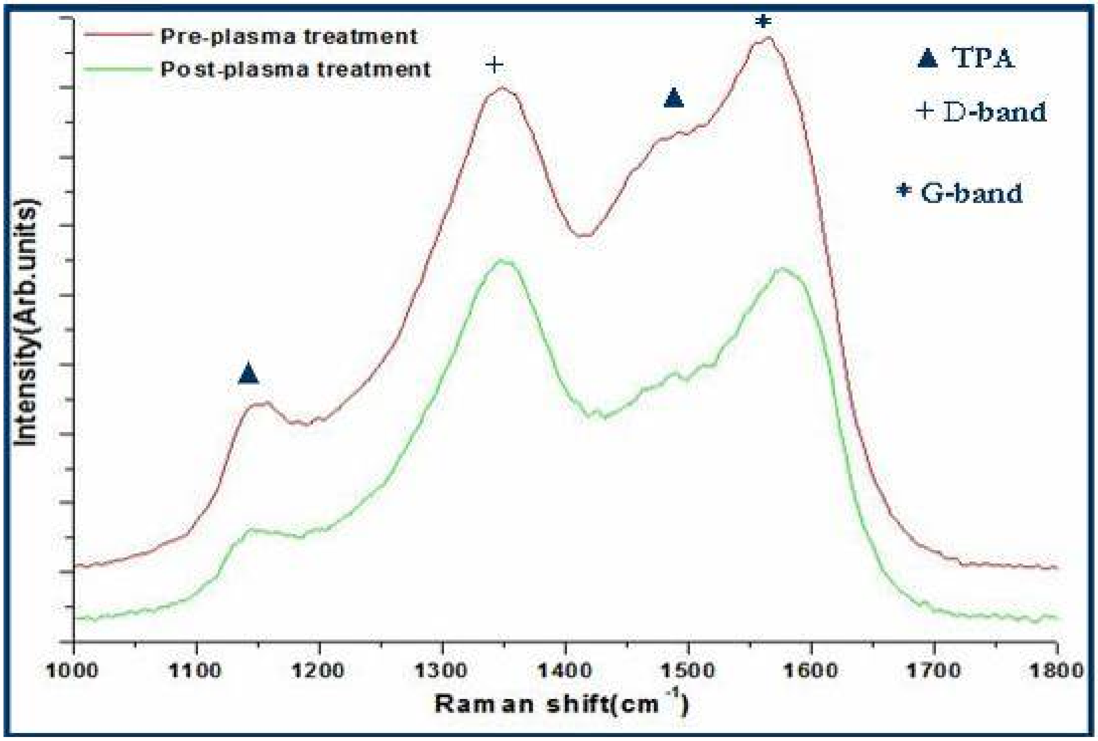

Figure 3.30 Raman Spectra of as-grown and Hydrogen Plasma Treated Films

The shift in the position of the G-band (1564 cm^{-1}) to a higher wave number (1577 cm^{-1}) suggests the possibility of changes in the bonding configuration of the sp^2 bonded carbon. It can also be observed that after the plasma treatment, the relative intensity of the G-band decreased than D-band. We have also observed from the NEXAFS measurements that the sp^2 content in the films reduced after the plasma treatment. These changes in the bonding characteristics of the plasma-treated films have shown significant influence on the electrical properties of these films. In Figure 3.31, the I-V response of nitrogen doped

NCD films after they were subjected to the hydrogen plasma and subsequent metal contact annealing is shown.

After Hydrogen Plasma Treatment

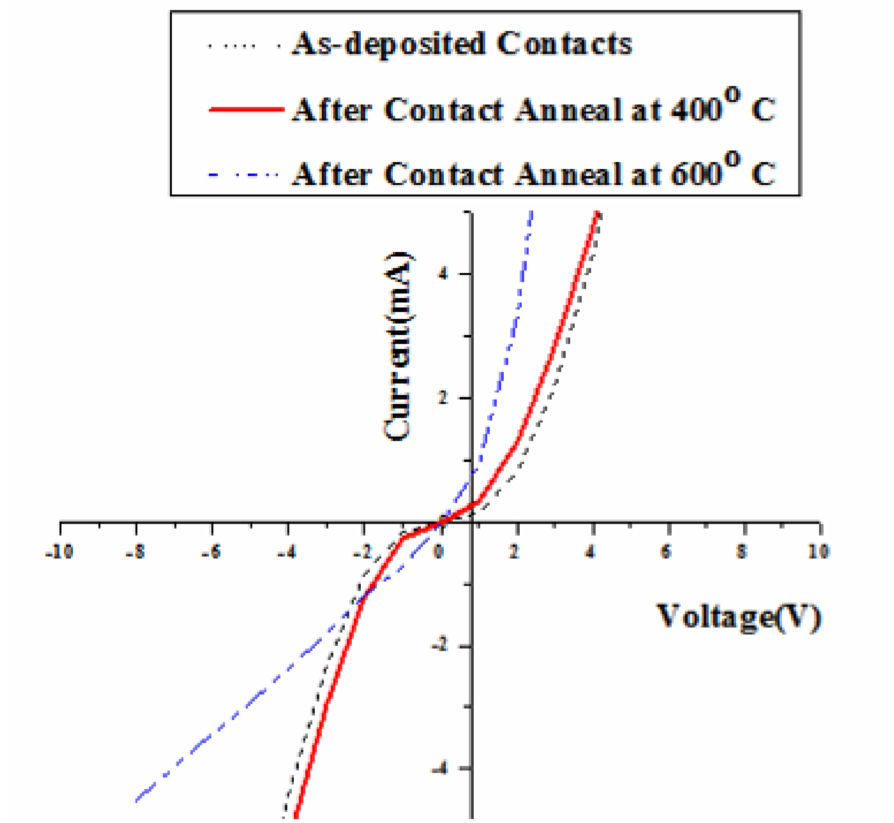

Figure 3.31 Current-Voltage Characteristics of Nitrogen Incorporated Nanocrystalline Diamond Film After the Hydrogen Plasma Treatment

The type of electrical contact formed between a metal and semiconductor depends on the properties of the interface. In all the cases, it can be observed that Ti/Au, which originally showed linear I-V characteristics on the as-grown films, changed their behavior after the plasma treatment. The same metal contacts do not form a true ohmic or a Schottky junction. Further, the post deposition annealing (PDA) of these contacts has not improved the linearity in their current-voltage response. It is known that the hydrogen treatment passivates the surface and compensates the defects present in a semiconductor. In a similar way, exposure of the diamond films to the hydrogen plasma could passivate the defects containing graphitic carbon and alter the electrical properties of these films. It has been reported that at room temperature, hydrogenation of HPHT synthetic type IIA (001) diamond substrates created a defective surface [93]. But, in this study, the samples were exposed to the plasma at temperatures (~700-750 °C) which removed the graphitic content [99]. It suggests that the formation of ohmic contacts in these films is definitely due to the presence of defects and graphitic carbon. It further supports that the electrical conduction in the films is through the defects in the grain boundaries [100].

3.17. Summary

With a brief introduction on the nucleation, growth of intrinsic and conductive NCD films, and growth mechanism of the nanocrystalline diamond films, this section has discussed the MPECVD growth reactor used for this research, along with various experiments performed to study the nucleation and optimization of the process chemistry for the growth of both intrinsic and nitrogen incorporated NCD films. The structural properties of both intrinsic and conductive NCD films have been evaluated. Several analytical techniques have been used to characterize the films and optimize the growth chemistry. The electrical properties of the conductive NCD films have been evaluated by forming suitable ohmic contacts and the effect of the surface plasma treatment on the nature of the electrical contacts have been discussed.

CHAPTER 4. FIELD EMITTER DEVICE FABRICATION APPROACH

4.1. Introduction

The current research is aimed at the application of nanocrystalline diamond films as a structural material for the fabrication of micro-electromechanical system (MEMS) devices and sensors. In spite of the extraordinary properties of diamond films, only a few diamond based MEMS applications have been reported due to the limitations in micromachining of complex MEMS structures. The fabrication and testing of MEMS devices such as cantilevers, and beams etc, have been reported [53, 101]. Other devices such as resonators, accelerometers and pressure sensors [102] have been fabricated as well. The inability to successfully grow n-type diamond films has limited the MEMS applications to use only intrinsic NCD or boron doped polycrystalline diamond [103]. The capacitive type pressure sensors and accelerometers using intrinsic diamond films were also under investigation. Though both capacitive [43] and piezo-resistive mechanisms [44] have drawn much attention due to their potential advantages, there are certain limitations with the current sensing technologies that should be paid attention.

Table 4.1 summarizes some of the fundamental differences and limitations with the capacitive and piezoresistive sensing mechanisms.

Table 4.1 Comparison Between Piezoresistive and Capacitive Sensing Mechanisms

Piezoresistive sensing	Capacitive sensing
Good linearity	More sensitive
Highly prone to temperature instability	Low temperature sensitivity
	Highly accurate and repeatable
	Consumes less power
	Requires on-chip complex circuitry

Due to the above limitations, other sensing mechanisms have attracted. Field emission based detection can be an alternative and effective method for sensing in terms of its temperature insensitivity, minimal resonance effects, and possibility to integrate with microelectronic circuits. The negative electron affinity (NEA) nature of diamond is an important property for its use in the both field and thermionic emission sources [62]. In addition to its NEA, the high thermal conductivity, robustness and chemical inertness play a significant role in enhancing the performance of diamond based devices. Both vertical and lateral field emission devices were fabricated using nitrogen doped NCD films [42, 51]. Field emission based magnetic sensors have been demonstrated previously [104]. The proposed work is aimed to develop vertical field emission devices using nitrogen doped NCD films as a structural material. Both free standing and capped field emission devices are fabricated and tested. The capped field emission source can act as a microelectronic field emission sensor.

4.2. Fabrication of Vertical Field Emission Source and Sensor

The processing steps involved in the fabrication of a vertical field emission sensor are shown in Figure 4.1.

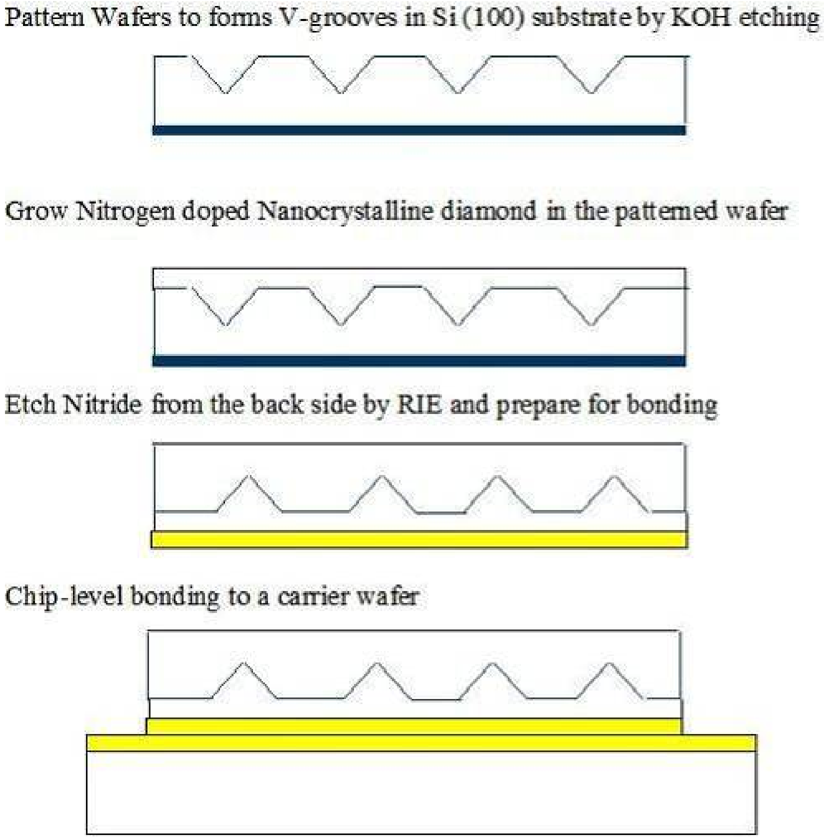

Figure 4.1 Process Steps for the Fabrication of Vertical Field Emission Sensor

Silicon etch to expose the diamond emitter tips

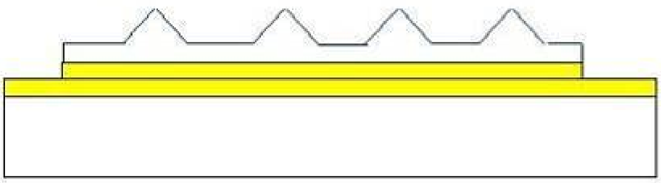

Etch Silicon to form Membrane

Wafer-level bonding of the membrane to the emitter array

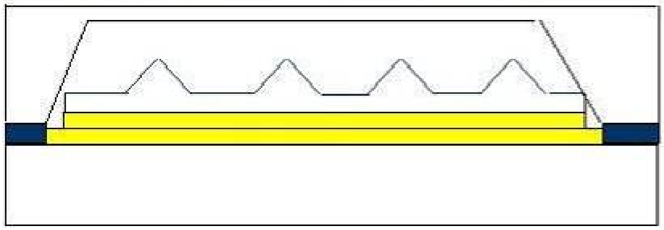

Figure 4.1 (Continued)

The first step involves patterning and etching the silicon (100) starter wafer in KOH to form the patterns for the emitter tips, followed by the deposition of a layer of conductive NCD film. A blanket film of metal is deposited on NCD as an intermediate metal layer for thermo-compression bonding. After bonding, the silicon mold is etched back to obtain free standing diamond emitters. This completes the fabrication of free standing field emitter array, which forms the cathode in the emission source. To fabricate the capped device, the next step is to form an anode on top of the cathode for collecting the electrons. Several techniques, such as self-aligned gates [42], silicon-on-insulator (SOI) wafers [105] etc., for the formation of gated structures have been reported. However, most of these methods involve complex fabrication steps due to the limitations of the photolithography. Fabricating the anode independently and integrating it with the cathode array is another technique to form the capped devices.

In order to accomplish this, a nitride layer is thermally grown on another silicon wafer and later patterned to open square windows and etched to form a thin membrane. This wafer containing membranes is bonded to the bottom wafer to form a complete field emission structure. Both free standing and capped field emission devices are tested for their emission characteristics in a high vacuum test chamber. By finite element modeling and simulations using *Coventorware*^{TM}, the deflection of the membranes are determined as they are subjected to external load. This data is useful to determine the inter-electrode separation and safe operating range of the sensor.

4.3. Testing of Field Emission Source and Sensor

The field emission testing of the devices is conducted in an ultra-high vacuum test chamber equipped with high voltage feed-throughs for electrical probing. The substrate holder is custom made with a conductive metal plate through which the emitter is made contact and the collector is connected to another thin metal plate isolated from the emitter plate. Both free standing and capped field emission devices are tested for their field emission characteristics in diode configuration after the test chamber is pumped-down to a base pressure of 5 X 10^{-8} Torr. In free standing devices, the emitted electrons are collected at the metal plate. In the capped devices, the field electrons are collected at the membrane which forms the anode. A sufficiently high voltage is applied to the cathode for the emission to initiate, and the emission current is recorded. Once the emission current is stabilized, the voltage is increased gradually and the corresponding emission current is measured. A low turn-on voltage and a stable emission current indicate desirable field emission properties. Once the field emission source is optimized to operate under stable conditions, the emission current at any instance should be constant at a constant applied voltage. At this instance, the membrane can be deflected. The variation in the field emission current can provide an estimate of the deflection which in turn can be correlated to the applied pressure. This type of pressure or a vibration sensor will be a proof of concept for detecting the changes in the vacuum level.

4.4. Summary

To summarize this section, the principle of field emission based sensing has been discussed along with the fabrication details of both free standing and capped field emission sources. Method of testing the field emitter device in a high vacuum environment using diode configuration is mentioned. The research on the vertical field emitter array acting as a cathode with a thin silicon membrane as an anode is proposed. The possibility of testing the capped field emission source as a sensor is discussed.

CHAPTER 5. DESIGN AND ANALYSIS OF VERTICAL FIELD EMITTER DEVICES

5.1. Introduction

A diode model of a field emission source/sensor consists of an array of emitter tips as cathode and an electron collector that acts as an anode. In capped field emission devices, the anode is made of silicon membranes which can function as a mechanical element (for deflection) in the sensor. In this section, the design of both the components is discussed and the finite element modeling and simulations were conducted using MEMS simulation software (*Coventorware*^{TM}).

5.2. Design of Diamond Field Emitter Array

The process flow for the fabrication of the field emitter array was shown in Figure 4.1. The details of the features on the emitter mask are listed in Table 5.1. The mask consisted of arrays of circular patterns with varying radii from 2 μm to 5 μm. The length of the trapezoidal base is equal to the diameter of the circular pattern; the height (L) of the tip can be calculated from the base width (W) by the expression W= √2 X L. Therefore, with the existing mask set, the height of the tips vary between 5.6 μm and 14 μm as the base width changes from 4 µm to 10 µm respectively. The dimensions of the field emitter dice are listed in Table 5.2.

Table 5.1 Design Specifications of the Field Emitter Mask

Size(µm)							Pitch
	4	5	6	7	8	10	
Array #	15	11	17	21	25	2C(Pitch-20)	15
Array #	35	12	1C	22	27	57(Pitch-20)	15
Array #	75	13	37	51	55		15
Array #		31	3C	52			15
Array #		32					15
Array #		33					15
Array #		71					15
Array #		72					15
Array #		73					15

Table 5.2 Design Specification of the Cathode

Cell	Area (μm^2)
A	5000 X 5000
B	7000 X 7000
C	10000 X 10000

A 3D solid model generated in *Coventorware*^{TM} (not to the scale) of a single cell demonstrating the field emitter array is illustrated in Figure 5.1.

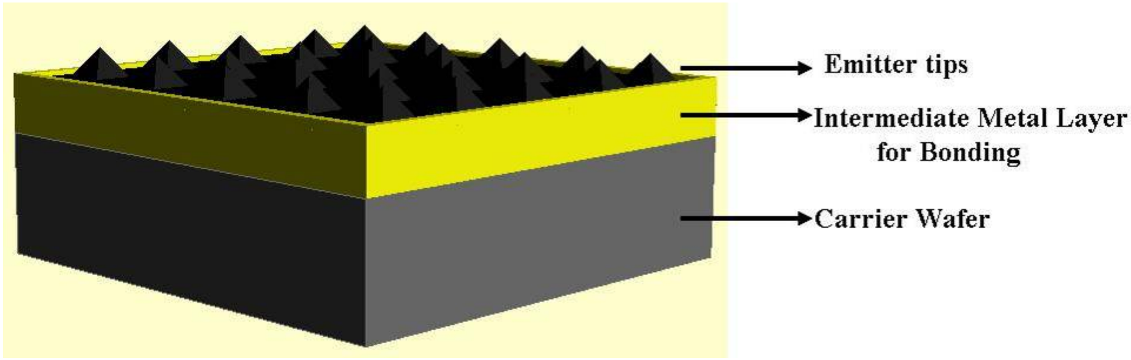

Figure 5.1 3D Model of a Free Standing Vertical Field Emitter Array Bonded to a Carrier Wafer

A 3D solid model representing the capped field emission device is shown Figure 5.2. The mechanical simulations have been conducted by parametric study in the MEMmech module of the *Coventorware*^{TM}.

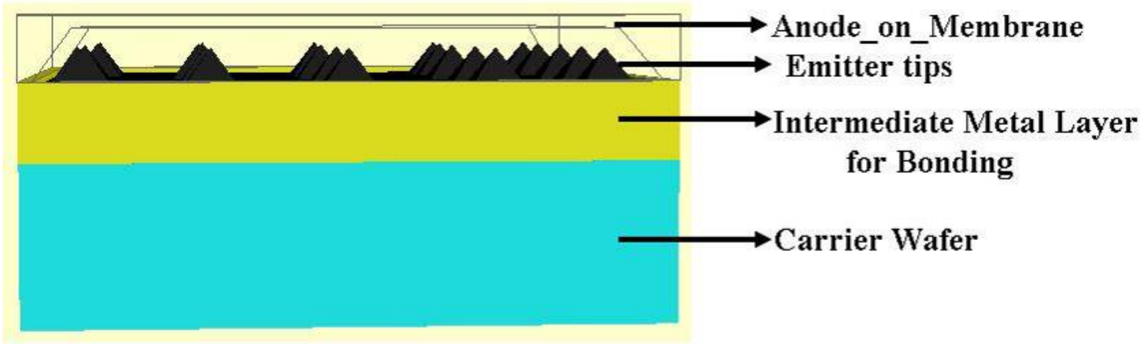

Figure 5.2 3D Model of a Capped Field Emitter Device

5.3. Design and Analysis of Anode-on-Membrane Using Generation I Mask

Anode of the field emission sensor is fabricated using thin silicon membranes flexible to external pressure and/or acceleration. Displacement of the anode depends on the magnitude of the applied pressure, and the dimensions of the membrane. As per the dimensions of the cathode (listed in Table 5.2), the anodes were designed to have square patterns of dimensions listed in Table 5.3.

Table 5.3 Design Specification of the Anode in the Generation I Mask

Cell	Area (μm^2)
D	8000 X 8000
E	10000 X 10000
F	12000 X 12000
G	14000 X 14000

The dimensions of the square patterns have been chosen to account for the undercut in the Si (100) plane during the anisotropic KOH etch. The boundary conditions applied for conducting the simulations on the diaphragms include fixing the deflection of the diaphragm frame along *x, y* and *z* directions while the load was applied gradually on the top face. For a fixed length and breadth, the effect of membrane thickness on the deflection was estimated to be a function of pressure. The thickness of the membranes was varied from 10 μm to 40 μm.

As the dimensions of the membranes were on the order of few millimeters, the deflection of the membranes was large and the response was non-linear when the pressure exceeded 0.2 MPa. Taking into account the processing limitations, loads exceeding 0.2 MPa cannot be exerted on these membranes. By using the design I masks, the anode and the cathode can be fabricated with a maximum separation of 260-270 μm depending up on the thickness of the diaphragm. To be realistic, if the deflection exceeds a safe value of 250 μm, there is a high probability for the anode and cathode to form a closed circuit and result in the device failure. Therefore, considering a 3% variation in the thickness of the membranes resulting from wet etching, the maximum deflection was limited to 250 μm. Thinner and larger membranes deflect more than 250 μm, and so pressures beyond 0.17 MPa (for cell # E, F, and G) cannot be applied. Devices with thinner and larger membranes as anode can be more sensitive to the changes in the pressure while the thicker and smaller membranes can be useful to increase the operating range.

Figure 5.3 shows the effect of membrane dimensions on the deflection as an external load up to 0.25 MPa was applied gradually. Though simulations have been conducted on membranes with thickness between 10 μm to 40 μm, the anode of the final device was fabricated with a 20 μm thick silicon membrane. Therefore, the simulation results of only those membranes are documented here.

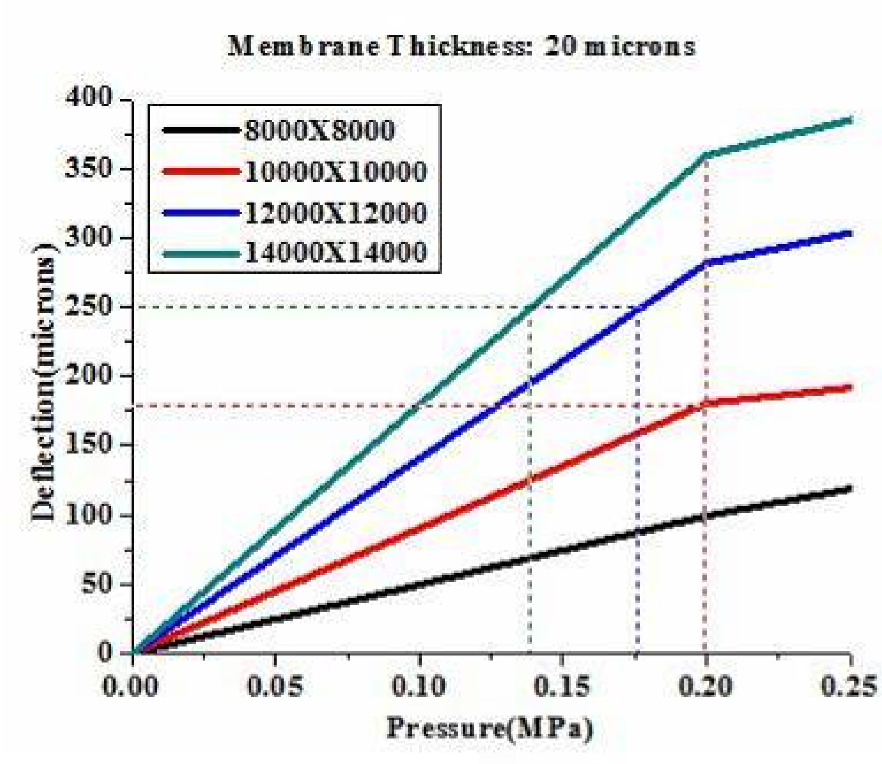

Figure 5.3 Effect of Membrane Dimensions on the Deflection of a 20 µm Thick Silicon Diaphragm

From the above graph, it can be noticed that devices with largest membranes as anodes can be operated below 0.15 MPa while pressures exceeding 0.2 MPa can be exerted on the smallest membranes (cell # D). Due to the above limitations, the devices fabricated using the generation I mask can function only as low pressure field emission sensors. In order to increase the operating range, second generation masks which include a boss structure in the center were designed. The incorporation of the center mass increases the net weight of the membrane thereby increases the measurement range.

5.4. Design and Analysis of Anode-on-Membrane Using Generation II Mask

The second generation design included a center boss structure with the membrane acting as four suspended springs. The first layer consists of the generation I mask, which defines the complete areas of the anode, and the second layer in the mask was used to define the regions of the center boss and form the membranes. The dimensions of the center boss and the outer membrane are listed in Table 5.4. A shallow etch after the exposure of the first mask determines the separation between the emitter tips and the anode. A deep etch followed after the exposure of the second mask determines the thickness of the membranes. A snapshot of the photo-masks used in the generation II membrane design is shown in Figure 5.4 (a) and (b) respectively.

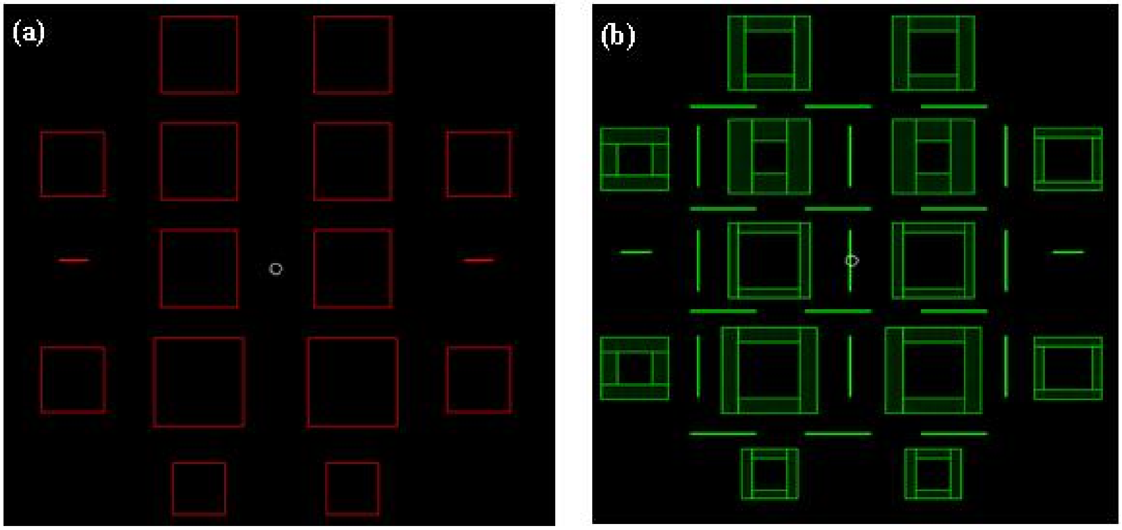

Figure 5.4 2D Image of Generation II Mask for the Fabrication of Membranes

Table 5.4 Design Specifications of the Anode and Proof-Mass in Generation II Mask

Cell	Area of Proof-mass(μm^2)	Total Area (μm^2)
D	5000 X 5000	8000 X 8000
E	7000 X 7000	10000 X 10000
F	9000 X 9000	12000 X 12000

A snap shot of the 3D solid model showing one individual cell is shown in Figure 5.5.

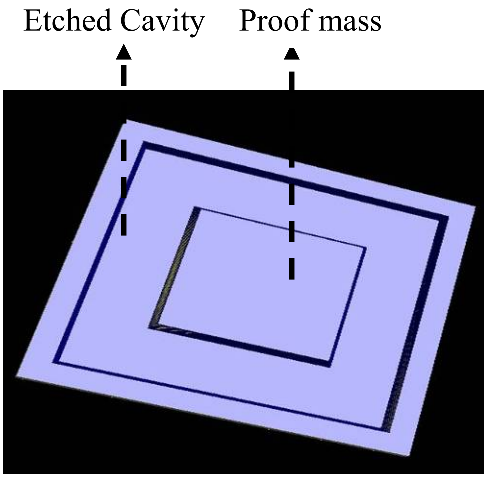

Figure 5.5 Snapshot of 3D Solid Model of a Single-Cell Using Generation II Mask

The simulations for the second generation membranes were carried with identical boundary conditions as the first generation. The depth of the shallow etch was approximately 50 µm. Therefore, the maximum safe operating deflection was limited to 40 µm. It can be observed that the linear range of operation is extened by incorporating a silicon boss structure within the membrane. As the anode and the cathode are seperated by ~ 50 µm, if pressures exceeding 0.8 MPa were exerted on the smaller membranes, the deflection exceeds the safe operating limits. Therefore, these devices can operate only up to 0.8 MPa *i.e.,* four times increase in the full-scale range as compared to the first generation devices. Figure 5.6 shows the effect of thickness of the membranes on the deflection as the pressure was varied. When the dimensions of the proof mass are increased and the net diaphragm area was kept constant, the operating range can be increased (Figure 5.6(b) and (c)). On the other hand, if the dimensions of the proof mass are kept constant and the total area of the diaphagm is increased, the converse appeared to be true (Figure 5.6 (a) and (b)).

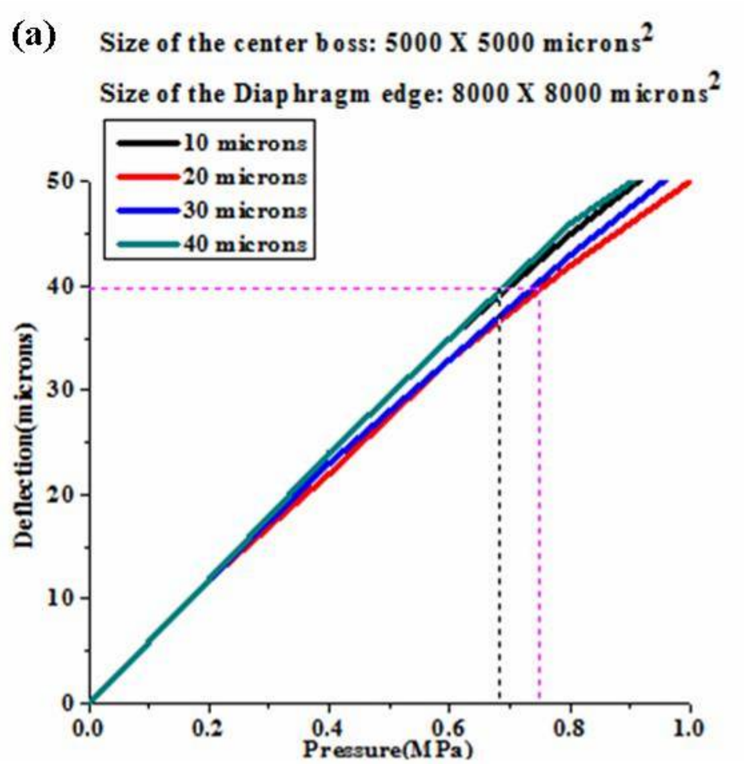

Figure 5.6 Effect of Membrane Thickness on the Deflection of Membrane (a) 5000 X 5000 μm^2_8000 X 8000 μm^2 (b) 5000 X 5000 μm^2_10000 X 10000 μm^2 (c) 7000 X 7000 μm^2_10000 X 10000 μm^2 (d) 7000 X 7000 μm^2_12000 X 12000 μm^2

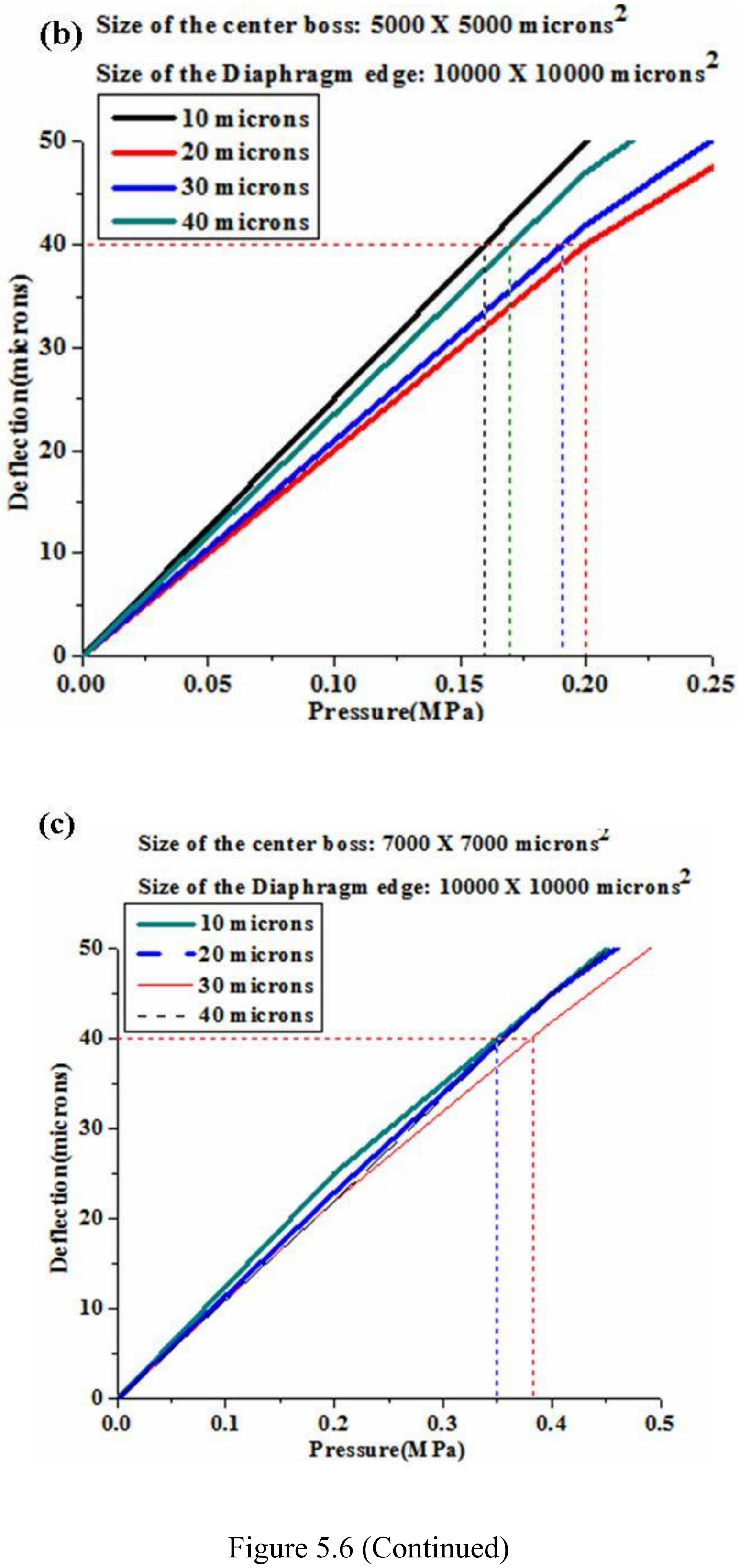

Figure 5.6 (Continued)

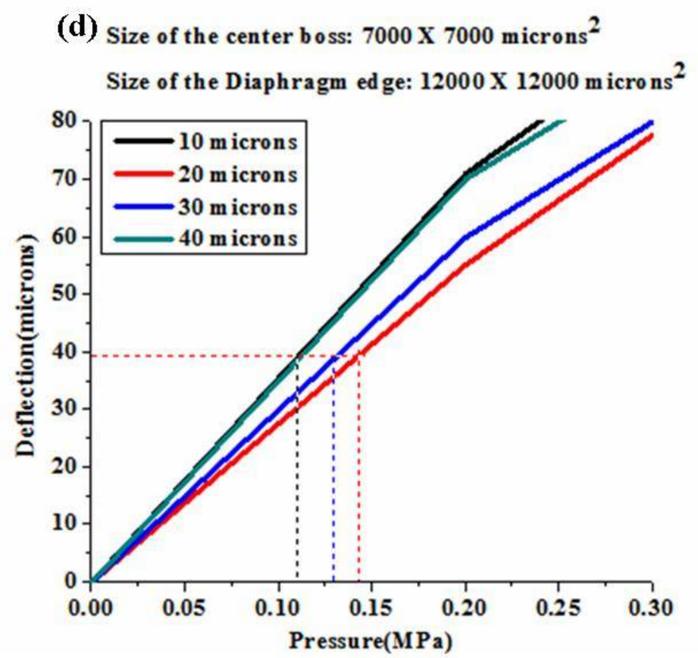

Figure 5.6 (Continued)

5.5. Summary

In this chapter, the design aspects of the field emitter arrays and the anode consisting of silicon membranes were discussed. The emitter mask has features with base widths varying between 4 μm and 10 μm. The height of the tips varied between 5.6 to 14 μm respectively. For the anode, two designs - Generation I consisting of free standing membranes and Generation II consisting of free standing membranes with center bossed structure were presented. The simulation results and the mechanical analysis of the membranes were done using *Coventorware*^{TM}. The effect of thickness and length of the membrane edges on the deflection were studied as a function of external pressure. The safe operating range of the devices was found by simulations. It was found that the operating range can be increased by at least four times on some of the devices when the anode consists of boss structure.

CHAPTER 6. FABRICATION AND CHARACTERIZATION OF FIELD EMITTER DEVICES

6.1. Introduction

This chapter describes the process techniques and characterization methods implemented in the fabrication of a field emission source and a sensor. The first part of the chapter discusses the fabrication of a vertical field emitter array by mold technique. The second part of the chapter presents the process implemented for the fabrication of anode array, and the third part details the integration of the cathode array and the anode to form a capped field emission device. The last part of the chapter provides the characterization results of the field emission devices.

6.2. Fabrication of Vertical Field Emitter Array by Mold Technique

The process flow for the fabrication of a vertical field emitter array by mold technique is shown in Figure 6.1. Single-side polished Si (100) wafers (n-type, thickness: 500-550 μm, resistivity: 5-10 ohm.cm) were used as substrates for this application. Prior to the fabrication, the wafers were cleaned in 30:1 BOE to etch native oxide. A SiN_x layer of thickness ~120 nm was grown by low-pressure chemical vapor deposition (LPCVD) method. The SiN_x layer acts as a good hard mask for the subsequent KOH etch. A positive resist PR1 2000 was spun on the wafers, followed by a subsequent pre-bake at 120° C for 60 seconds. The photoresist acts as hard mask during the SiN_x etch in a reactive-ion etcher (RIE) and the pattern on the silicon substrate is exposed for the subsequent KOH etch. The Si (100) wafers are etched by anisotropic KOH etch (30% KOH (269.5 ml) in DI water (229.5 ml), 80°C, 450 rpm) to form the inverted pyramidal grooves with an angle of 54.7° between the (100) and (111) planes.

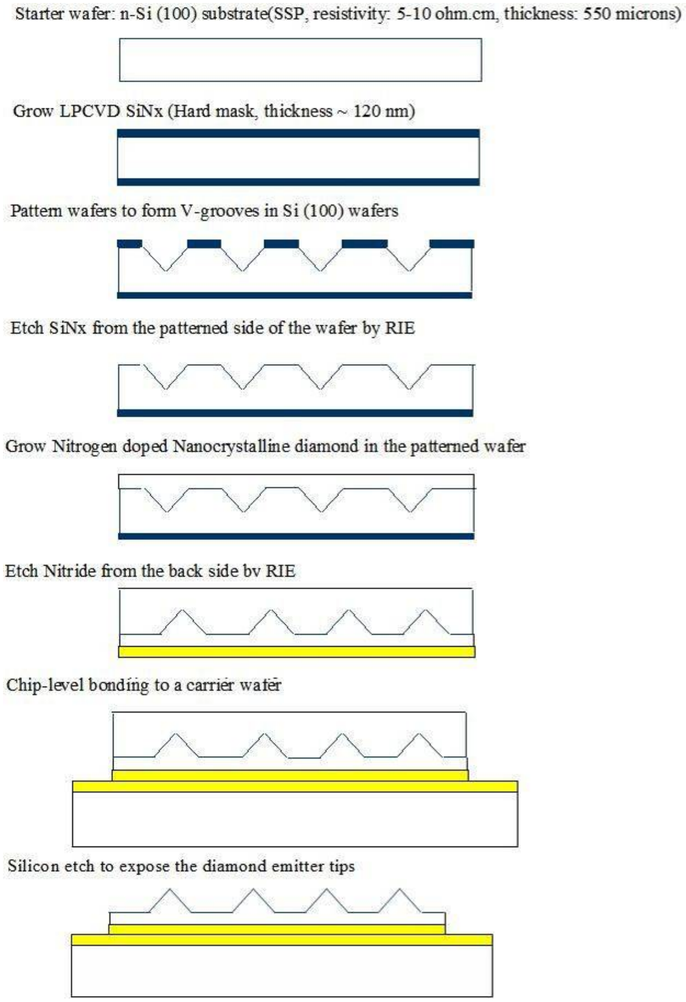

Figure 6.1 Process Steps for the Fabrication of Vertical Field Emitter Array

6.3. Challenges in the Processing of Vertical Field Emitter Devices

Unlike the fabrication of lateral field emission devices, the fabrication of vertical field emission devices involves many processing steps. As the number of fabrication steps increase in a process, the corresponding yield will be low unless the process is extremely controlled. Anisotropic KOH etching is very widely implemented in most silicon MEMS fabrication methods. It was observed that after the KOH etch, the surface of the patterned pyramidal structures was covered with some particulates that appear as “sugar-crystals”. The size of these particulates varied between 50-200 nm. The scanning electron micrograph of a pyramidal pattern after the KOH etch is shown in Figure 6.2. It was found that the source of contamination was not from the experimental set-up or the glassware but from the KOH pellets used for preparing the commercial KOH solution. A similar observation reported by another group stated that the particulate precipitation occurs only after the removal of the wafers from the KOH bath and was found to be independent of the duration of etching [106].

It was confirmed by energy dispersive x-ray (EDAX) analysis that the crystals inside the etched cavities are indeed the precipitates of iron particles. The particles were present only in the etched cavities and not on the SiN_x hard mask confirming that the source of the particles was not from the experimental set-up but instead the dissolved impurities in the KOH solution which adhere only to the silicon surface. The area scan EDAX spectrum obtained is shown in Figure 6.3.

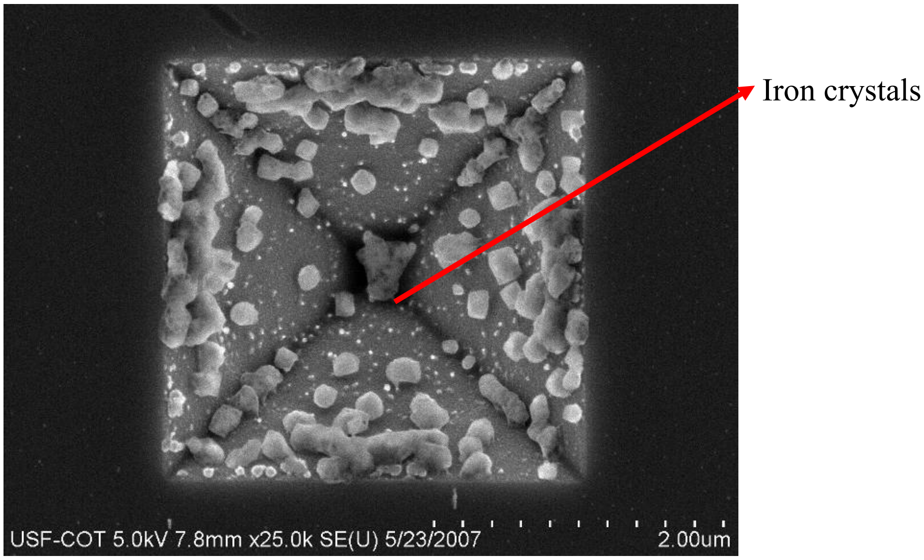

Figure 6.2 SEM Micrograph of KOH Etched Inverted Pyramidal Mold Containing Iron Particulates

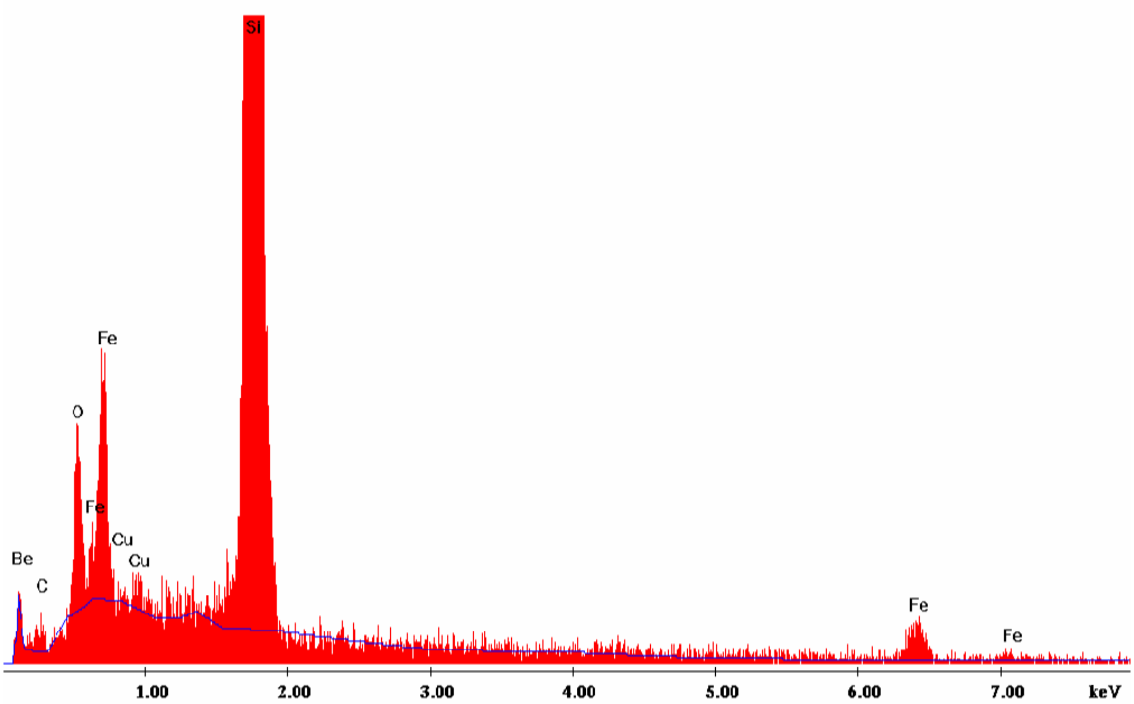

Figure 6.3 EDAX Area Scan of the Pyramidal Mold Containing Iron Particulates

The EDAX spectrum represented the peaks corresponding to elements-Be, C, O, Fe, Cu and Si. The intensity of the peaks corresponding to Be, C and Cu were negligible and their source could not be identified. On the other hand, the intensities of K_α, L_α, K_β and L_β lines corresponding to the elemental Fe and K_α line of elemental O were pronounced. The presence of this unwanted precipitate in the pyramidal etched cavities had detrimental effects during the nucleation and the growth of diamond films. Consequently, after the KOH etch, the wafers were soaked in iron-oxide etchant for about 15 minutes. The SEM micrograph of a sample after iron-oxide etching is shown below in Figure 6.4.

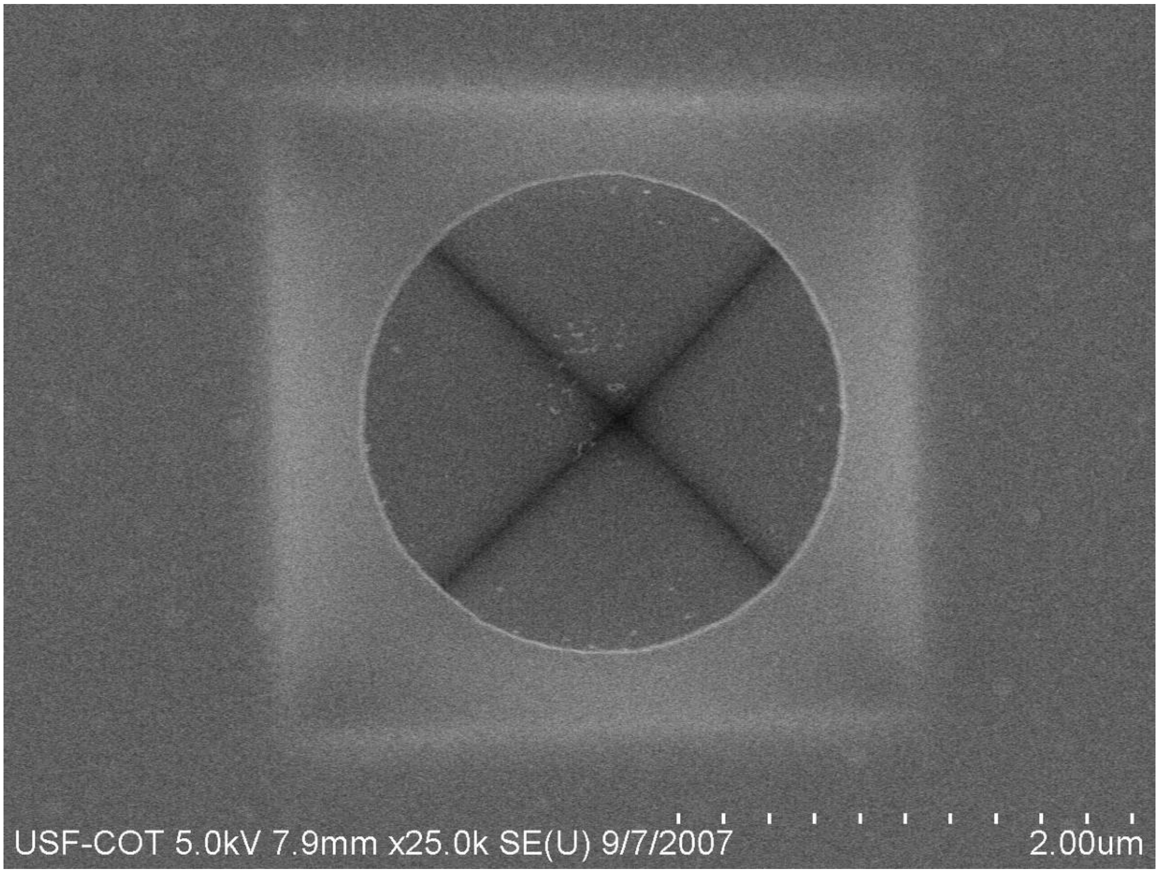

Figure 6.4 SEM Micrograph of the V-groove After Iron Oxide Etch

It can be noticed that the iron-precipitates have been successfully removed from the etched cavities. As mentioned earlier, the presence of iron particles in the grooves resulted in several problems during the post wafer processing. It was observed that the presence of iron particles has resulted in a discontinuous film and rough morphology of the diamond tips after they were etched and released. The SEM image shows the rough morphology of the diamond tip with several voids due to the embedded iron particles (Figure 6.5).

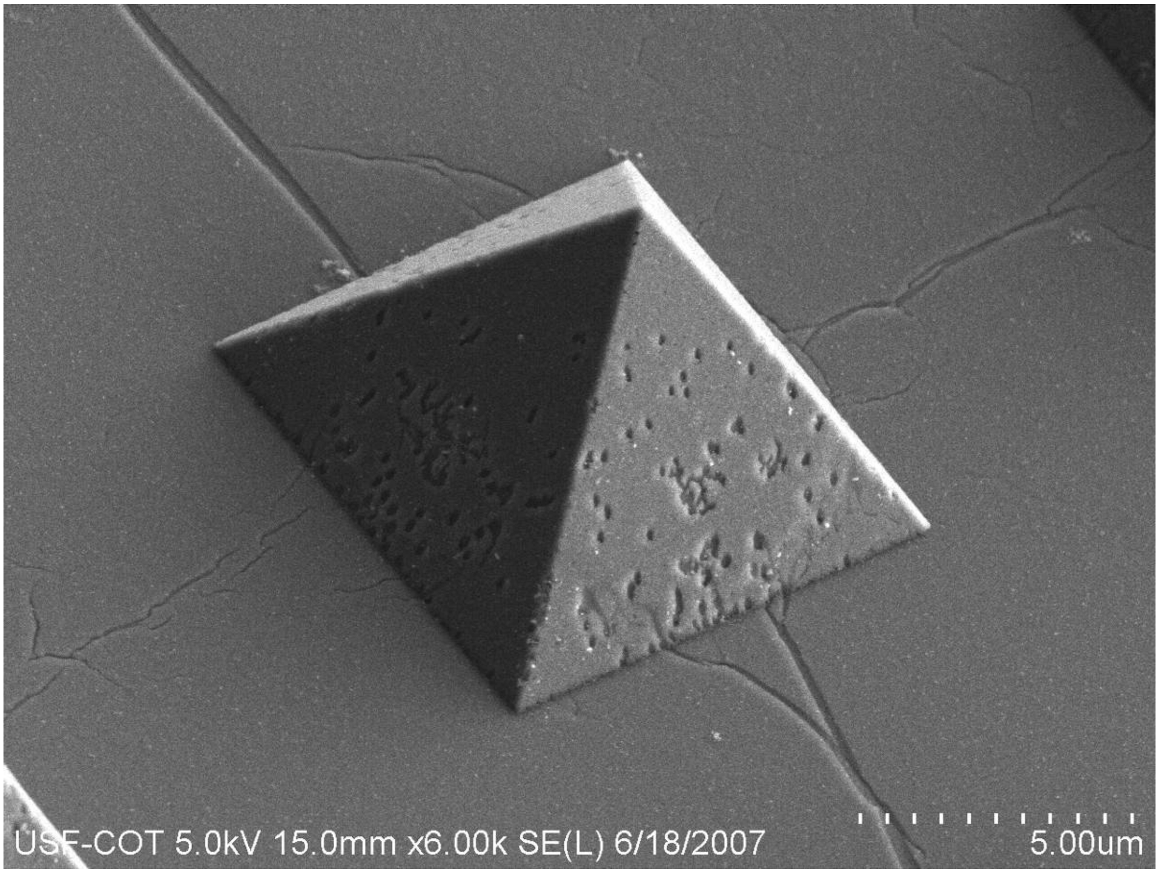

Figure 6.5 SEM Micrograph of a Diamond Pyramid With Pinholes Resulted From Iron Particulates in the Etched Cavities

6.4. Determination of Tip-Radius by Focused Ion Beam (FIB)

It is important to determine the radius of the emitter tip as it determines the geometrical field enhancement factor (β). It is widely known that as the tip becomes sharper the β factor is improved, thereby the field emission properties can be enhanced. In order to determine the tip radius, a single inverted pyramid in the pattern was milled by the focused ion beam. The sample preparation was made by depositing a layer of Pt followed by the milling or thinning down with Ga^+ ions. During ion milling, as the sample thins down from the edge of a pattern to inside, the depth of the mold gradually increases until the geometrical center plane of the square base is reached and then decreases with further milling. The actual depth and the radius of the tip are obtained at the geometrical center plane. The scanning electron micrograph of a tip at the geometric center plane is shown in Figure 6.6.

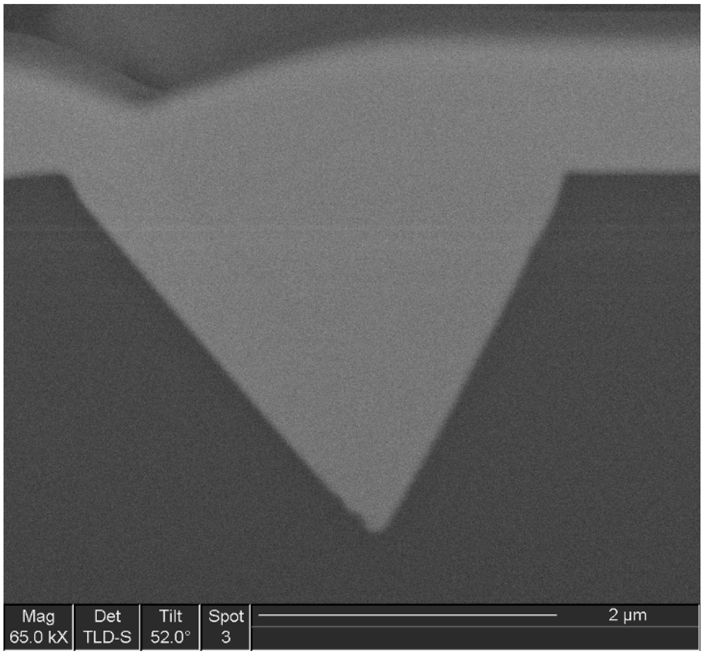

Figure 6.6 FIB Cross-Section Image of a V-groove in Silicon Substrate

It was estimated that the tip radius in the patterned wafers was ~ 100 nm. The radii can be further reduced by sharpening the tips by growing an oxide layer in the etched cavities [107].

6.5. Deposition of Nanocrystalline Diamond Films in the Inverted Pyramidal Molds

It is known that that the KOH etch of patterned Si (100) substrates results in intersecting (111) planes with an angle of 54.7° between (100) and (111) planes. As high density nucleation is important to grow uniform films, it is essential to achieve high density nuclei along all the planes of the patterned substrate. The seeding is initiated by ultrasonic scratching in a mixture of titanium nanopowder and diamond nanopowder suspended in acetone. NCD films have been deposited for different durations-3 hours, 6 hours and 12 hours to determine the uniformity of the growth. The SEM micrograph of an emitter pattern filled with n-NCD film is shown in Figure 6.7. The low-resolution SEM image (Figure 6.7(a)) shows an array of individual emitter cell, while the high-resolution SEM image (Figure 6.7(b)) shows the growth of the nanodiamond film in the etched cavity. It can be noticed that after a 6 hour deposition, the diamond film did not completely fill the silicon mold. For longer durations (samples grown for 12 hours), NCD films fill the pyramidal molds in the substrate. Continuous and uniform film along the inner walls of the pyramid, *i.e.* along the (111) planes, indicates the uniform nucleation in the cavity.

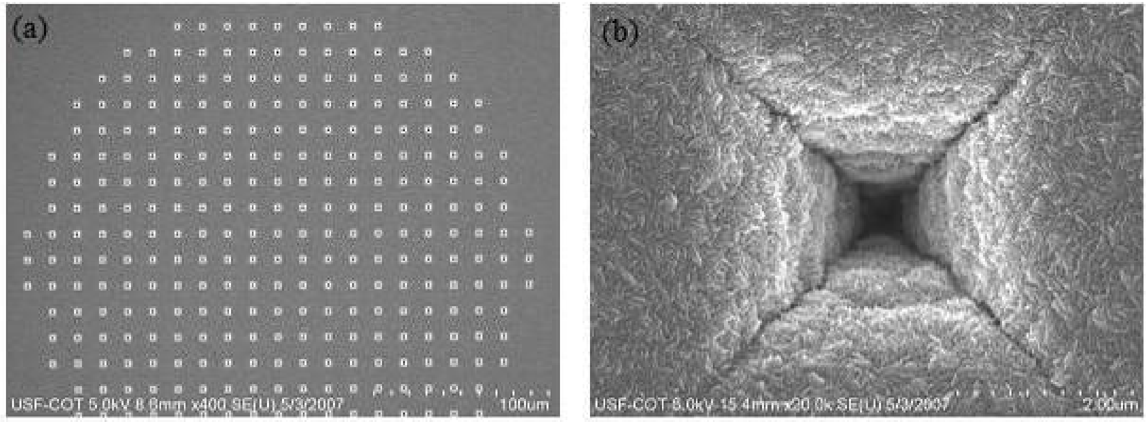

Figure 6.7 SEM Micrograph of the Surface of Nitrogen Incorporated NCD Film Partially Filled in the Silicon Mold (a) Low-Resolution Image of the Field Emitter Pattern (b) High-Resolution Image of the NCD Film Deposited in a Single Inverted Pyramidal Cavity

6.6. Processing Issues-Chip-Level Bonding

After depositing NCD films on the silicon substrates, the wafers are diced and the individual dice are bonded to a carrier wafer for etching the silicon mold, and thereby exposing the emitter tips. The chip-level bonding is performed by flip-chip method using anisotropic conductive film (ACF) and by gold-to-gold thermo-compression bonding. Figure 6.8 shows the temperature-time profile used in this method of bonding. A bi-layer of Cr/Au or Ti/Au was deposited by sputtering onto Pyrex or silicon carrier wafers. Prior to the bonding, ACF was cured for 20 to 30 minutes at room temperature. The flip-chip bonding was carried by applying an external load of 80N at a temperature of 175°C for 30 minutes. ACF melts under external heat and load to form a bond between the die and the carrier wafer.

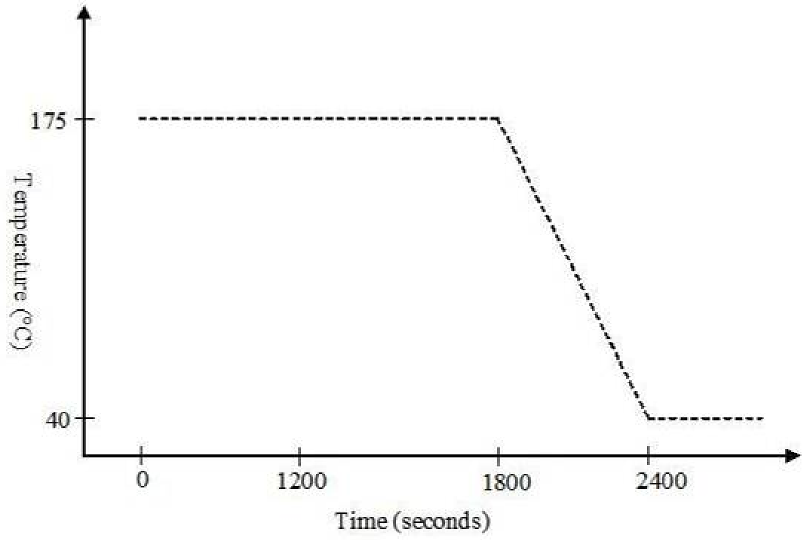

Figure 6.8 Time vs. Temperature Plot of Thermo-Compression Bonding Using Anisotropic Conductive Film

The next step in the device fabrication is to etch the silicon mold and expose the emitter tips. The bulk etching of silicon was carried either by HNA (mixture of Hydrofluoric acid, Nitric acid and water (instead of Acetic acid) in 2:1:2 ratio) or by hot KOH (30% KOH in H_2O, 80°C). The choice of the wet etchant depended upon the type and size of carrier wafer, and the bi-metal stack. It was observed that the etch rate of Si (100) planes in both KOH and HNA solution was approximately 1 μm/min. In order to protect the edges of the carrier wafers from etching, the wafers were loaded into custom-made jigs (Figure 6.9) that can protect the back and the sides of the wafer during etching the samples in the HNA solution.

Figure 6.9 100 mm Jig for Backside Wafer Protection During Etching

ACF consists of metal particles in the polymer matrix that allows the current conduction along one direction. The metal particles present in ACF were attacked by HNA during etching thereby the adhesion between the bonded die and the carrier wafer became poor. The SEM micrograph of a sample bonded using ACF is shown in Figure 6.10.

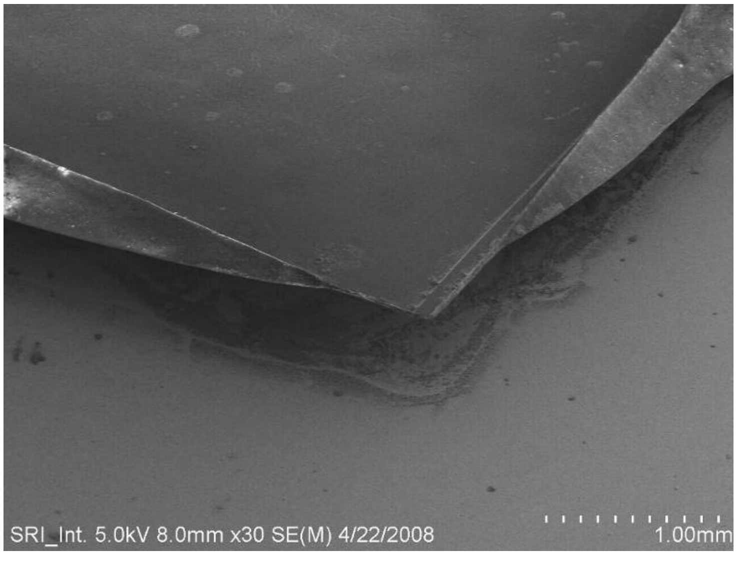

Figure 6.10 SEM Micrograph of ACF Bonded Chip After Partial Etching in HNA

The poor adhesion between the ACF bonded die and the carrier wafer can be observed. For prolonged HNA etching, the die detached from the carrier wafer. Hence, the use of ACF for bonding was abandoned and alternative bonding was carried.

To avoid the problems during etching, thermo-compression bonding was done with Au-Au as intermediate metal layers. A layer of Ti (100 nm)/Au (120 nm) or Cr (100 nm)/Au (120 nm) was deposited on both the patterned emitter wafer and the carrier wafer. In thermo-compression bonding, the individual die was bonded to the carrier wafers by applying an external load of 80 N at a temperature of 320 °C for 4 minutes. Figure 6.11 shows the temperature vs. time profile used in thermo-compression bonding.

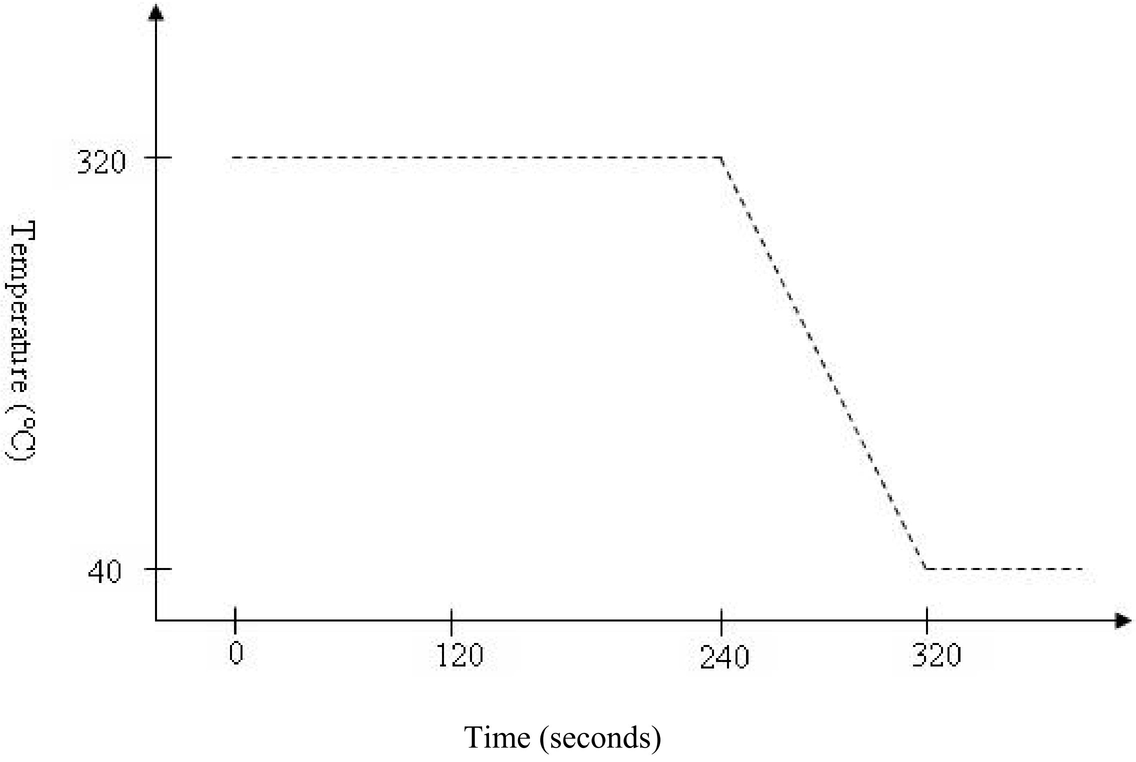

Figure 6.11 Time vs. Temperature Plot for Gold-to-Gold Thermo-Compression Bonding

It was observed that the bonding was not strong and the die was separated from the carrier wafer at the Au layer. By varying the thickness of Au films, and experimental conditions during bonding, there was no improvement. An electro-plated gold layer served as a very good intermediate metal layer for thermo-compression bonding. The details on the electro-plating are provided in the below section. The difference in the bond strengths of the sputtered and electro-plated gold films was attributed to the differences in the surface morphology of both the films.

The SEM micrographs of sputtered and electro-plated gold films are shown in Figure 6.12 (a) and (b) respectively. It can be observed that the sputtered gold films consist of well defined and closely packed grains. On the other hand, the surface of the electro-plated gold is non-homogenous. These differences in the morphology resulted in the different bond strengths during the chip-level bonding.

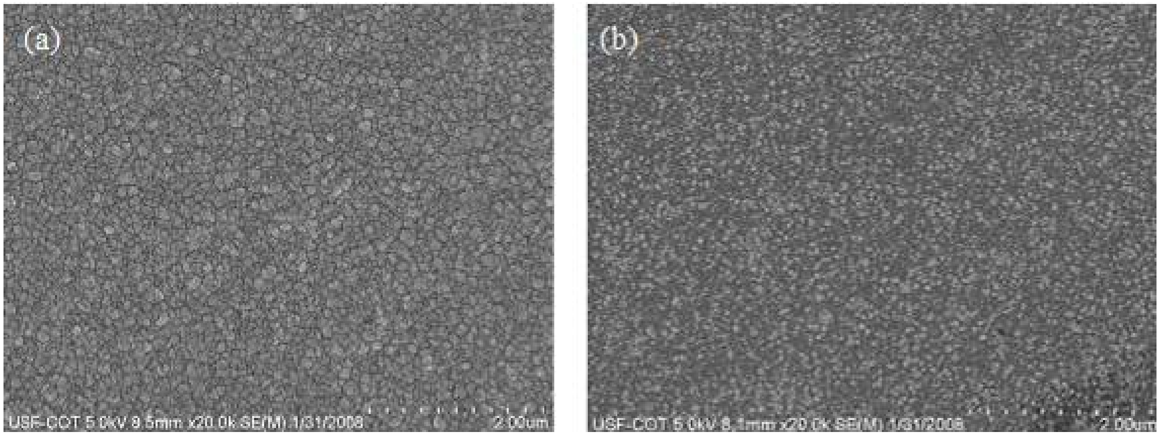

Figure 6.12 SEM Micrograph of (a) Sputtered Gold Film (b) Electroplated Gold Film

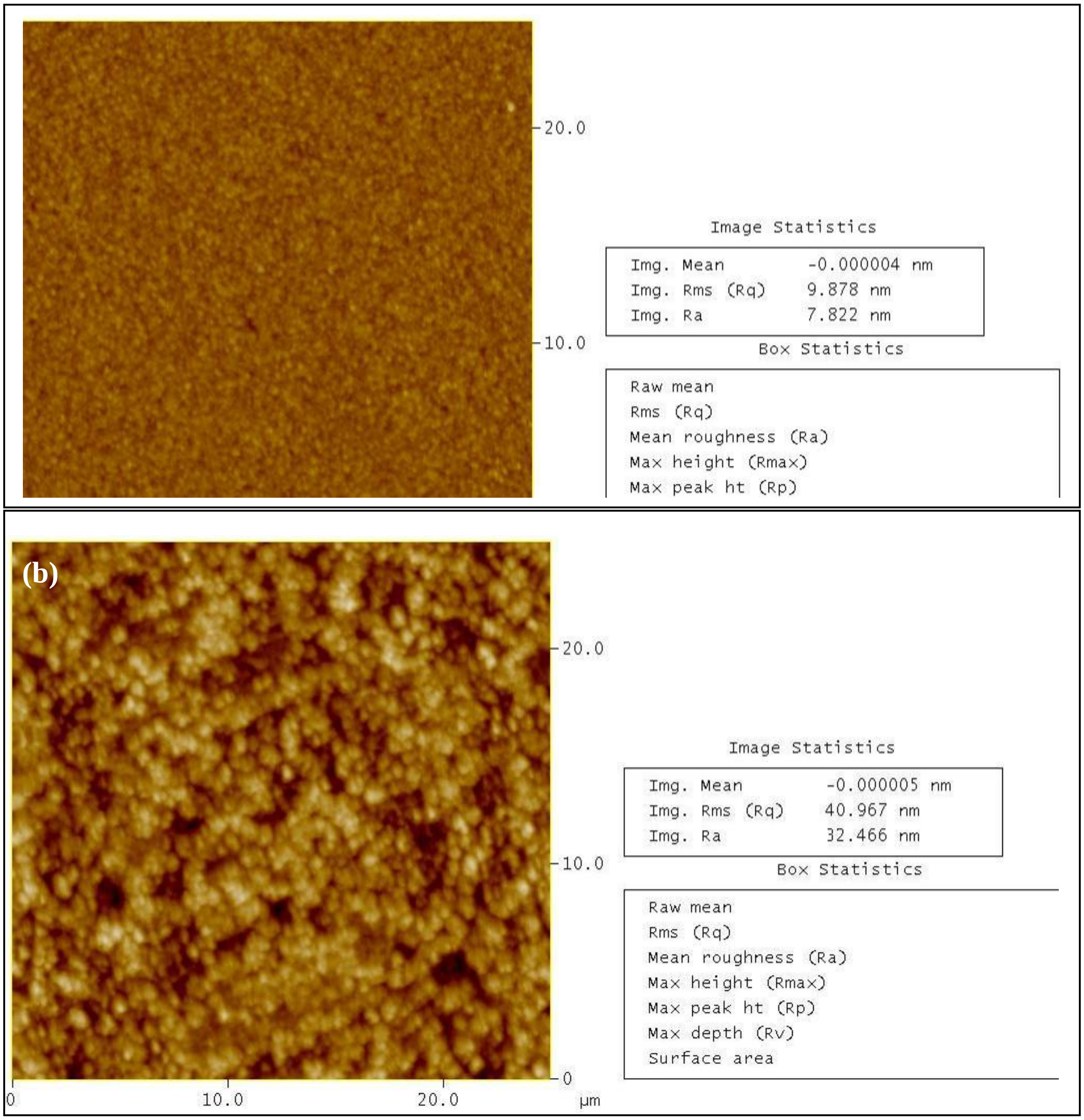

Image Statistics
Img. Mean -0.000004 nm
Img. Rms (Rq) 9.878 nm
Img. Ra 7.822 nm
Box Statistics
Raw mean
Rms (Rq)
Mean roughness (Ra)
Max height (Rmax)
Max peak ht (Rp)

Image Statistics
Img. Mean -0.000005 nm
Img. Rms (Rq) 40.967 nm
Img. Ra 32.466 nm
Box Statistics
Raw mean
Rms (Rq)
Mean roughness (Ra)
Max height (Rmax)
Max peak ht (Rp)
Max depth (Rv)
Surface area

Figure 6.13 AFM Micrographs of (a) Sputtered Gold Film (b) Electroplated Gold Film

The poor bonding between the sputtered gold films can also be due to extremely smooth surfaces of the films. The atomic force microscopy images of both sputtered and electroplated gold films are shown in Figure 6.13 (a) and (b) respectively. It can be found that the average surface roughness of the sputtered films was approximately 8 nm where as the electroplated films have a rough surface morphology with a mean surface roughness of approximately 30 nm. The difference in the surface roughness, along with the density and the mechanical properties of the films can cause poor mechanical interlock when the sputtered gold films were used as an intermediate metal layer. The low-resolution and high-resolution SEM micrograph of a thermo-compression bonded die is shown in Figure 6.14 (a) and (b) respectively.

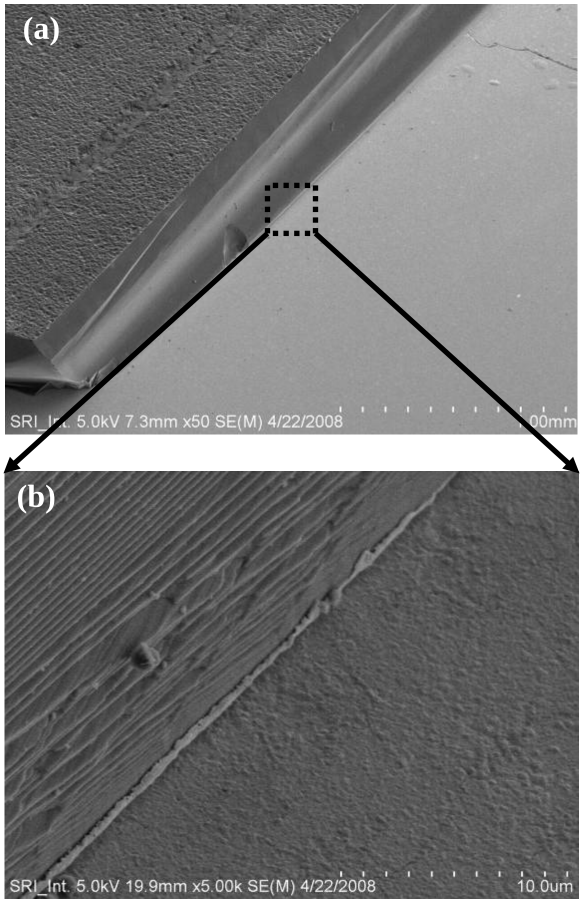

Figure 6.14 SEM Micrograph of Au-Au Bonded Chip (a) Low-Resolution (b) High-Resolution Showing the Interface

After bonding, the silicon mold was completely etched either by HNA or by KOH without any adhesion problems at the Au-Au interface. SEM micrograph of a free standing emitter array on a thin NCD film is successfully released from the buried silicon mold (Figure 6.15).

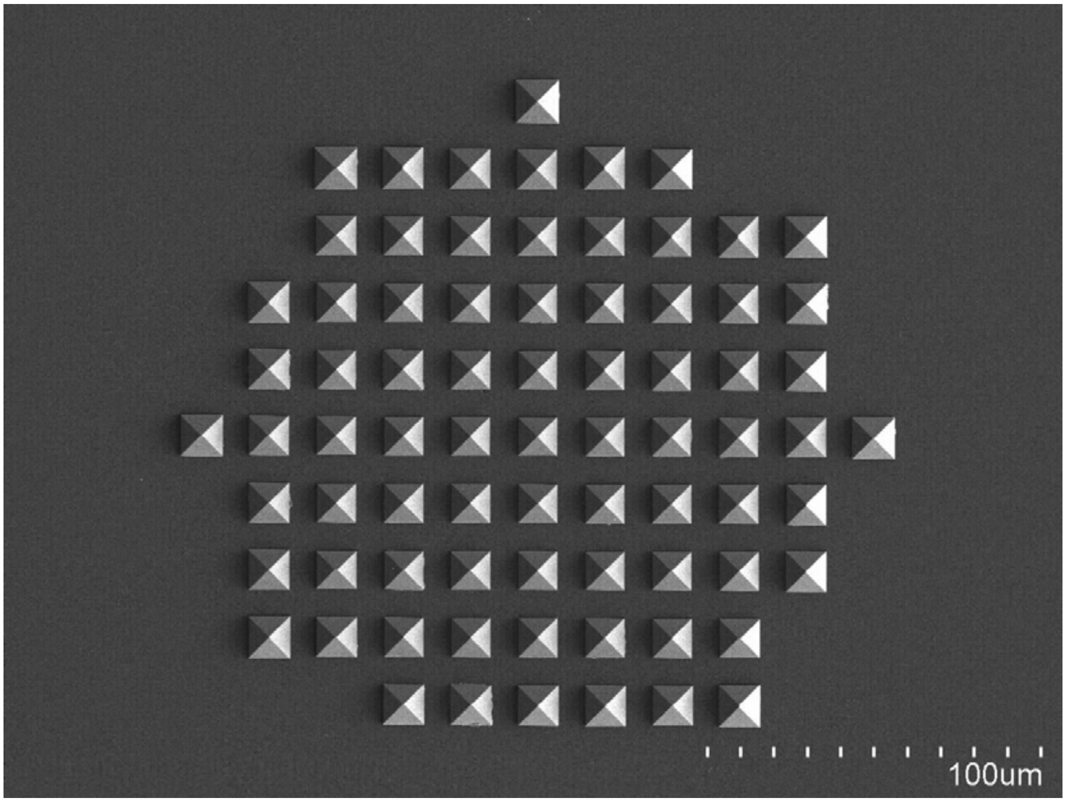

Figure 6.15 SEM Micrograph of a Free Standing Field Emitter Array After Successful Silicon Etch

6.7. Electroplating of Gold Films as Metal Layer for Thermo-Compression Bonding

Electroplating is a very convenient method for depositing thick metal layers, which may not be practical to deposit by other conventional deposition techniques. The electroplating of copper and gold are widely implemented in semiconductor manufacturing for interconnects, vias and trenches. In this research, electroplating was used to deposit the gold films as intermediate metal layers for bonding. Prior to the deposition of gold, a seed layer of Ti/Au or Cr/Au was deposited by sputtering. A simple electroplating setup is shown in Figure 6.16.

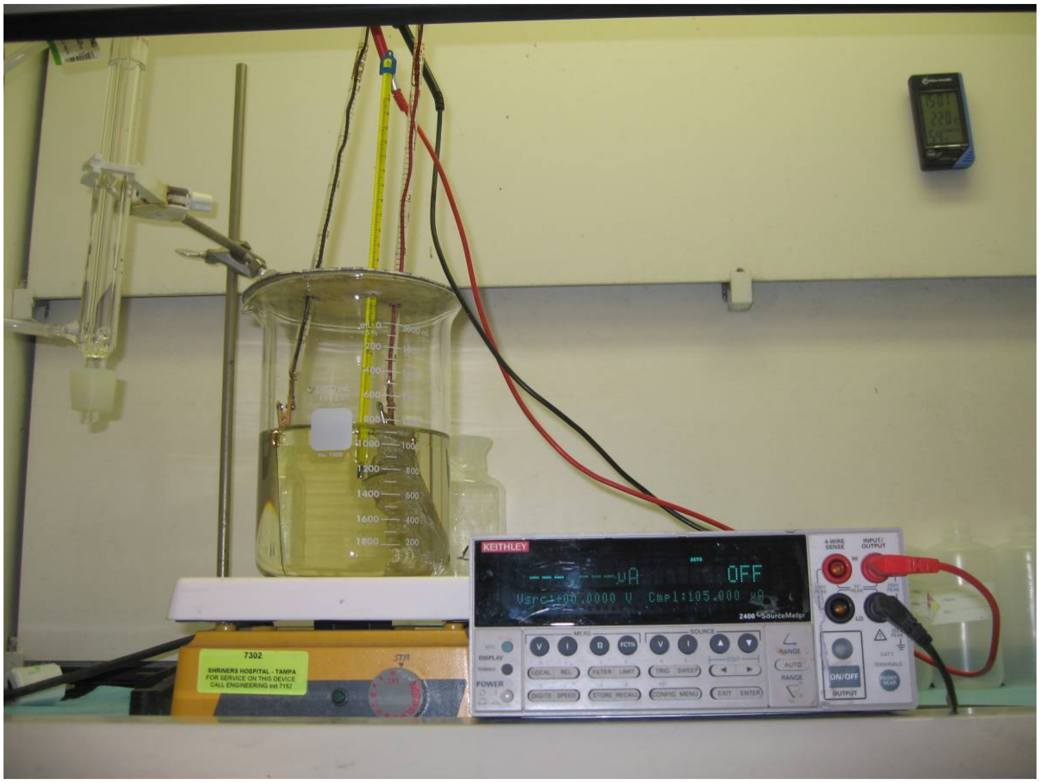

Figure 6.16 Electroplating Cell for Depositing Gold Films on 100 mm Wafers

Like any other electroplating cell, the cathode is connected to the sample and the anode to a platinum mesh. A commercially available TG25 RTU consisting of gold sulphate solution (*Technic Inc.*) is used as an electrolyte. The solution is continuously stirred and heated to 58 °C. A constant current density between 1-4 mA/cm^2 is passed to the cell by a

Kiethley 2400 current source meter. Typically for a 100 mm wafer, an approximate current of 162 mA/cm^2 is applied to electroplate a film of thickness ~ 4 µm.

6.8. Fabrication of Anode-on-Membrane Wafers Using Generation I Mask

The double side polished (DSP) Si (100) wafers (n-type, thickness; 300-350 µm, resistivity: 5-10 ohm.cm) were used as starter wafers for the fabrication of membranes. After the standard cleaning, a thin SiN_x layer was grown by low-pressure chemical vapor deposition (LPCVD). A negative resist NR 9 1500 was spun on the wafers followed by a subsequent pre-bake at 150° C for 60 seconds. After photo-lithography, the wafer is post baked at 100°C for 60 seconds and developed in RD6 for 40 seconds. After the nitride layer from the patterned regions is etched, the wafers were loaded in KOH bath (30% KOH (269.5 ml) in DI water (229.5 ml)) to etch the exposed silicon surface. As there was no etch-stop layer, a timed KOH etch was done until the desired thickness of the membrane was achieved. The process flow for the fabrication of silicon membranes using the generation I mask set is shown in Figure 6.17.

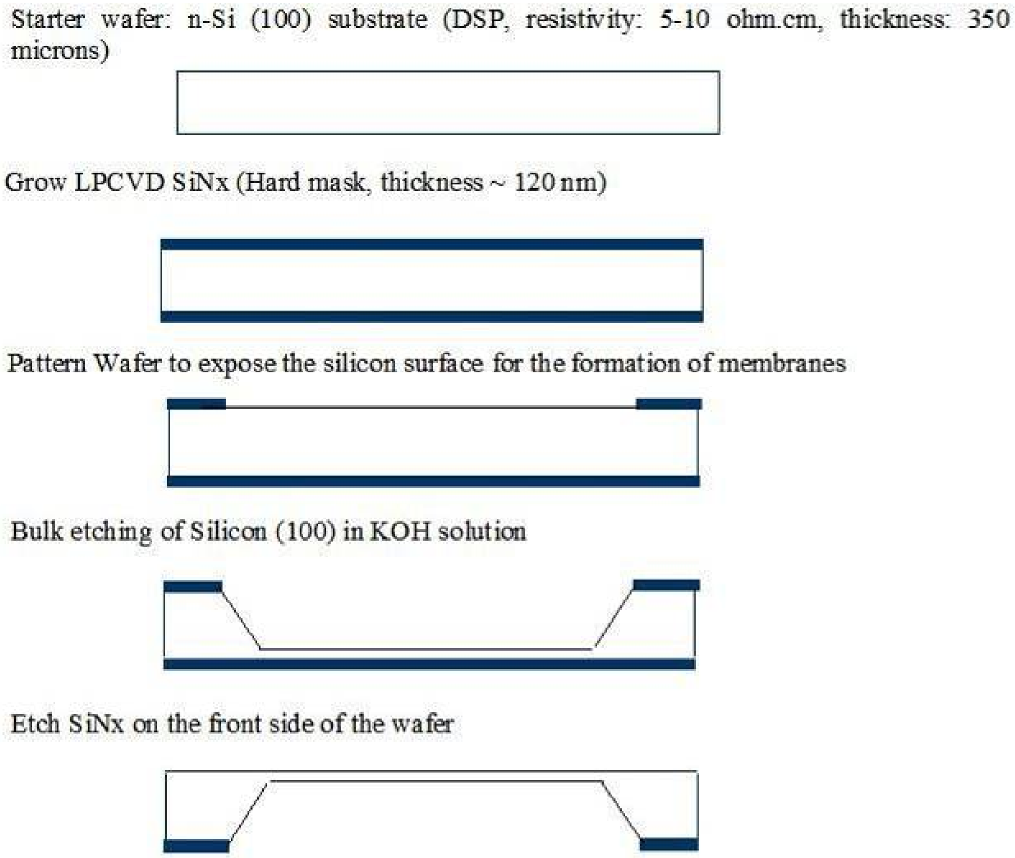

Figure 6.17 Process Steps for the Fabrication of Anode-on-Membrane Using Generation I Mask

The SEM micrograph of a membrane after the pattern is fully etched is shown in Figure 6.18. The thickness of the membrane as estimated using an optical microscope was between 10-20 µm. Figure 6.19 shows the picture of a fully processed 100 mm wafer with various membranes.

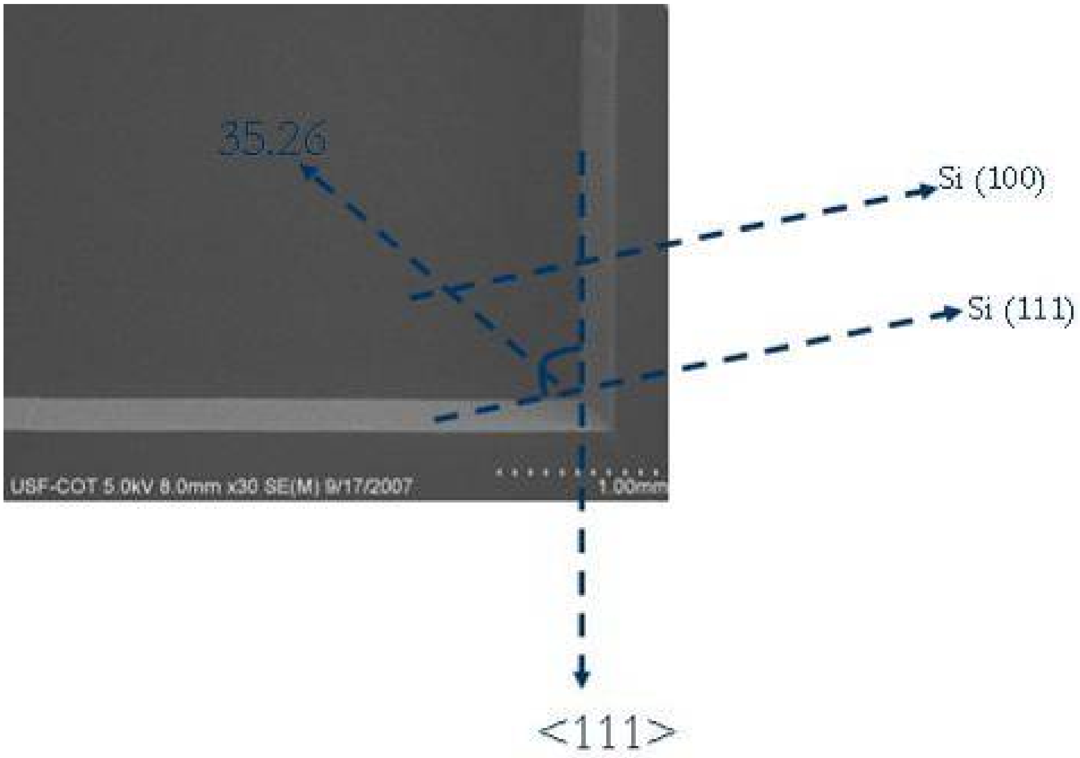

Figure 6.18 SEM Micrograph of a Generation I Silicon Membrane After Anisotropic KOH Etch

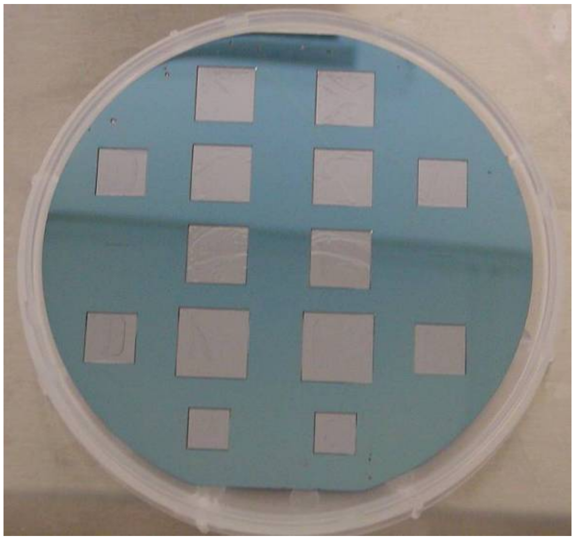

Figure 6.19 Snapshot of a Fully Processed Generation I Silicon Wafer After KOH Etch

6.9. Fabrication of Anode-on-Membrane Wafers Using Generation II Mask

In addition to the process steps as shown in Figure 6.17, an additional nitride layer is grown after the first KOH step. The modified process flow for the fabrication of generation II membranes is shown in Figure 6.20. After the shallow etch, a 120 nm thick nitride film was grown by low-pressure chemical vapor deposition (LPCVD) method. A photo-lithography step defines the regions of the center boss structure. After etching the nitride from the developed regions on the wafer, the negative photoresist is stripped and the wafers were then loaded in the KOH bath for bulk etching of the exposed silicon surface to form thin silicon membranes.

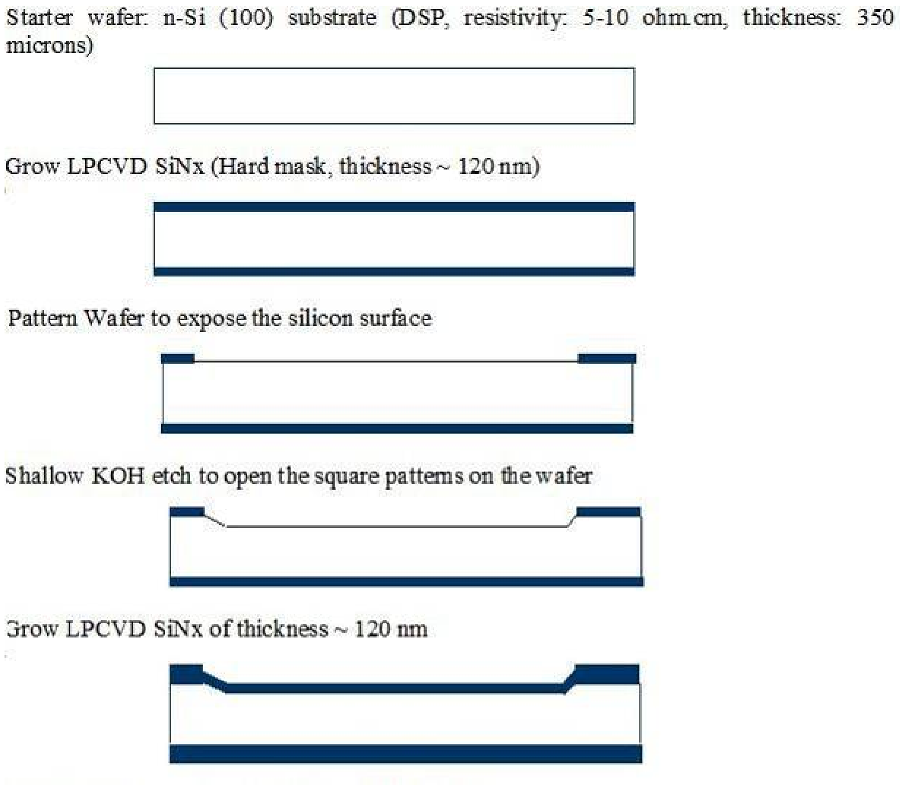

Starter wafer: n-Si (100) substrate (DSP, resistivity: 5-10 ohm.cm, thickness: 350 microns)

Grow LPCVD SiNx (Hard mask, thickness ~ 120 nm)

Pattern Wafer to expose the silicon surface

Shallow KOH etch to open the square patterns on the wafer

Grow LPCVD SiNx of thickness ~ 120 nm

Figure 6.20 Process Steps for the Fabrication of Silicon Membranes Using Generation II Mask

Pattern wafer to open areas for deep KOH etching

Bulk etching of Si to form the membranes

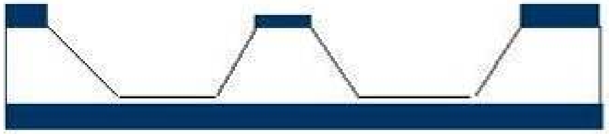

Etch Nitride from the front and back side of the wafer

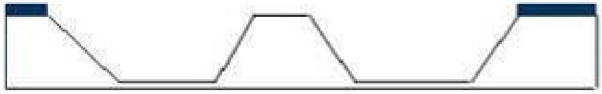

Figure 6.20 (Continued)

For a typical wafer thickness of 300-350 µm, and for an etch rate of 1 to 1.2 µm/min, the wafer is etched for 4.5 to 5 hours to obtain membranes of thicknesses on the order of 10 to 20 µm. The SEM micrograph (sample tilted) of a membrane formed after etching Si (100) wafer using second generation mask is shown in Figure 6.21. The under cut in the center boss structure is due to the anisotropic KOH etching. As the dimensions of the membranes are in several millimeters, the full size of the membrane could not be captured. Figure 6.22 shows the snap-shot of a fully processed 100 mm wafer with various membranes prior to the nitride etch.

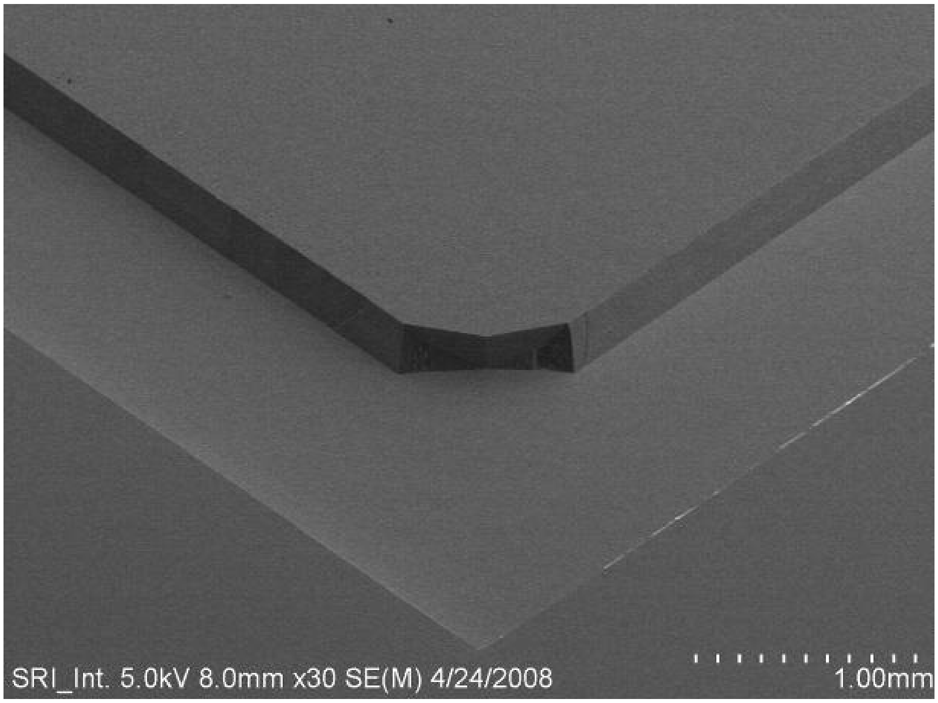

Figure 6.21 SEM Micrograph of a Fully Etched Generation II Membrane After Anisotropic KOH Etch

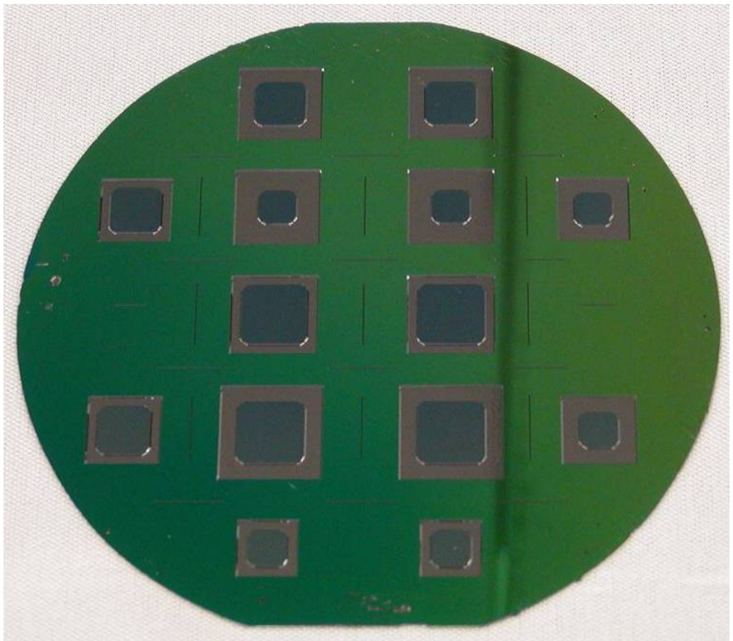

Figure 6.22 Snapshot of a Fully Processed Generation II Silicon Wafer

6.10. Integration of the Anode and the Cathode

To integrate the anode and the cathode, both the parts were fabricated on 100 mm wafers. The earlier version of the devices was bonded to a silicon wafer using gold as an intermediate metal layer. But due to the difficulty in protecting the silicon (carrier) wafer from unwanted etching, the process has been changed by implementing Pyrex wafer as a carrier substrate for bonding the individual field emitter dice. A bi-layer of Cr/Au was sputtered onto the Pyrex wafer followed by the deposition of a thick electroplated gold film. The wafer is then patterned to define the contact pads to bond the dice in a flip-chip bonder. In order to make the electrical contact, vias are opened in the bond pad regions by laser milling and through wafer interconnects were achieved. Prior to the testing, the vias were filled using a conductive silver epoxy. Figure 6.23 (a-c) shows the processing steps at the wafer level.

In the next step, the silicon mold was completely etched in hot KOH solution with similar composition as described earlier. By changing the process from silicon to Pyrex, the device fabrication was more reliable and reproducible. After 6 to 8 hours of KOH etch, the silicon mold was completely etched and the wafer consisted of an array of field emitter devices. The snapshot of a wafer after etching the silicon mold is shown in Figure 6.23 (c). The next step in the fabrication is bonding of the anode wafer to the cathode wafer in a wafer-to-wafer bonder. As the thermal expansion coefficients of Pyrex and silicon wafers are similar, thermal mismatch is minimal and therefore the bonding can be better.

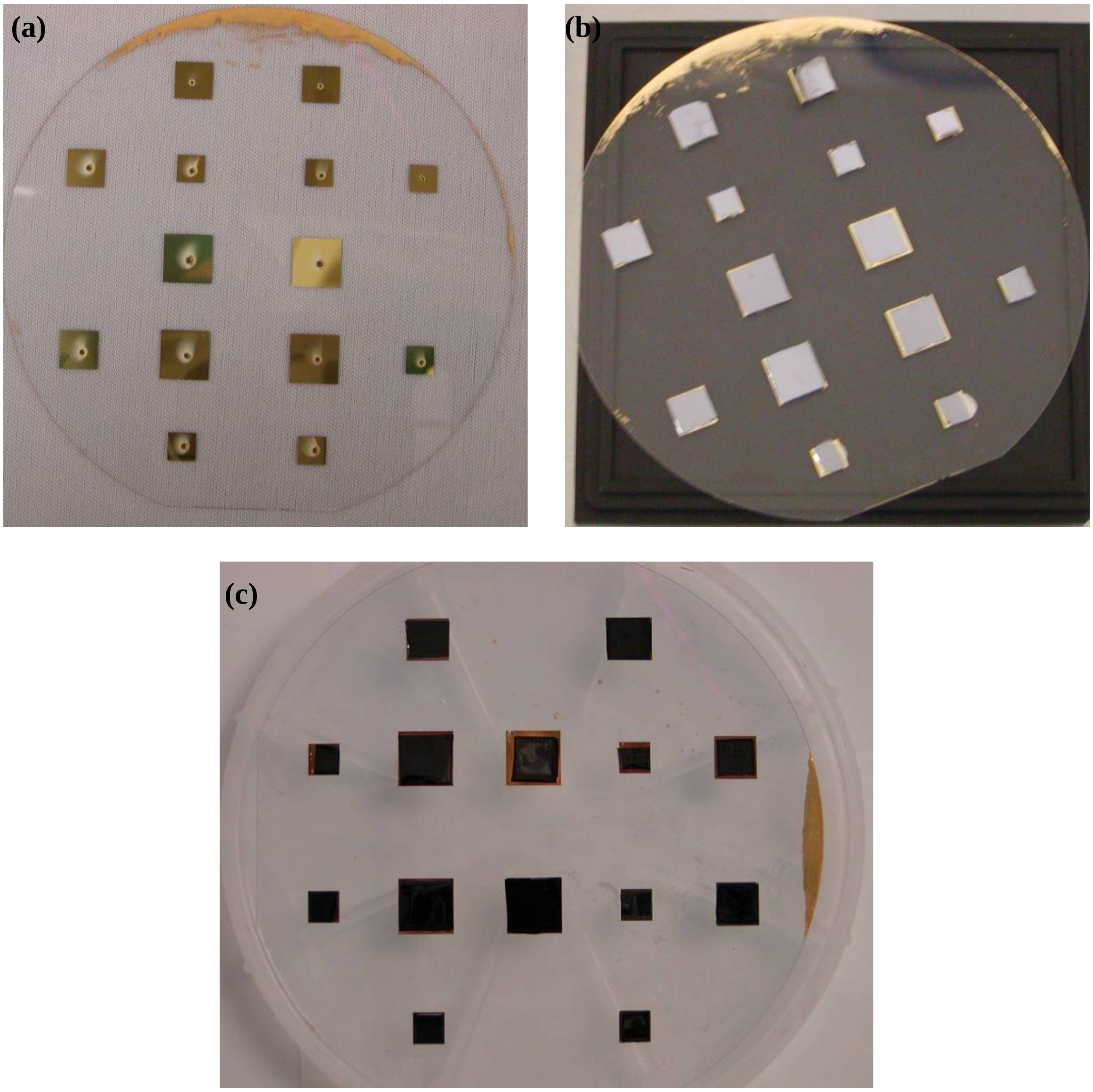

Figure 6.23 (a) Pyrex Wafer After Laser Milling Through Holes for the Electrical Contacts (b) Pyrex Wafer Flip-Chip Bonding Diamond Dice to the Gold Bond Pads (c) Snapshot of a 100 mm Wafer After Etching the Top Silicon Mold

6.11. Wafer-to-Wafer Bonding

The integration of anode and the cathode wafers was carried out in an *EVG EV501* wafer bonder by vacuum anodic bonding technique. Prior to the bonding, the hard mask (SiN_x) on the silicon wafer was etched and the silicon wafer with the membranes is bonded to the Pyrex carrier wafer. The process conditions used for the vacuum anodic bonding are: Force-500 N, Voltage- -1000 V, Temperature- 400°C, Bond time-20 minutes. As the thickness of the membranes was between 10 and 20 μm, some of the membranes were not mechanically strong to withstand bonding. When the silicon wafer consisted of the generation I membranes, the gap between the apex of the tips and the surface of the membrane was ~ 260-270 μm and therefore, the vacuum gap between the anode and the cathode could be achieved. But when the wafers consisted of generation II membranes, the spacing was reduced to ~ 50 μm and during wafer-to-wafer bonding; it was observed that the generation II silicon wafers and the Pyrex wafers were completely bonded. Ideally, during this step, it is anticipated to have a separation between the center proof mass regions and the cathode so that the vacuum gap can be obtained. A batch of wafers have been fabricated with different etch depths (20 μm to 100 μm) to find out the optimum depth at which the vacuum gap can be prevailed without bonding completely. But, the problem during the wafer-to-wafer bonding was not fully solved. When the initial etch depth was ~ 100 μm, the transfer of patterns from the second layer of mask was difficult due to non-uniform photoresist thickness at the edges of the first pattern. Therefore, the final version of the devices consisted of anodes fabricated using the generation I mask. After the wafers were bonded, a top metal contact (Cr/Au) was deposited by sputtering and the wafer stack was diced to individual chips for carrying the field emission testing.

6.12. Characterization of Field Emission Devices

The field emission characteristics of both free standing and capped devices were tested in a diode model (Figure 6.24).

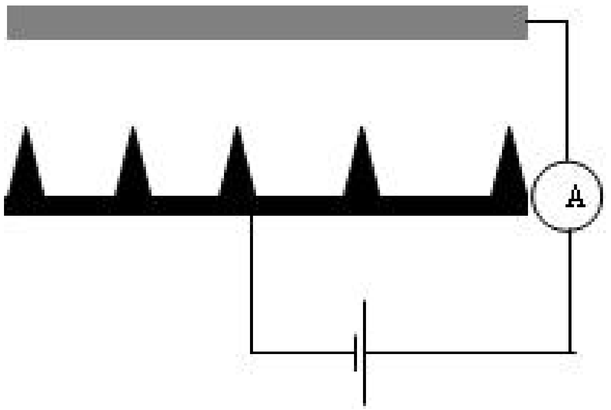

Figure 6.24 Field Emission Device in Diode Configuration

The field emission test chamber shown in Figure 6.25 is equipped with a turbo-molecular pump that can pump down to low pressure of 10^{-8} Torr. The D.C bias to the cathode can be applied through the high voltage electrical feed throughs and the emission current can be measured. Manipulation of the sample can be done by a linear motion feed through. In free standing devices, a molybdenum plate was used as an anode. The anode and the cathode are separated by an insulator. The field emission properties were tested at a base pressure of 5×10^{-8} Torr.

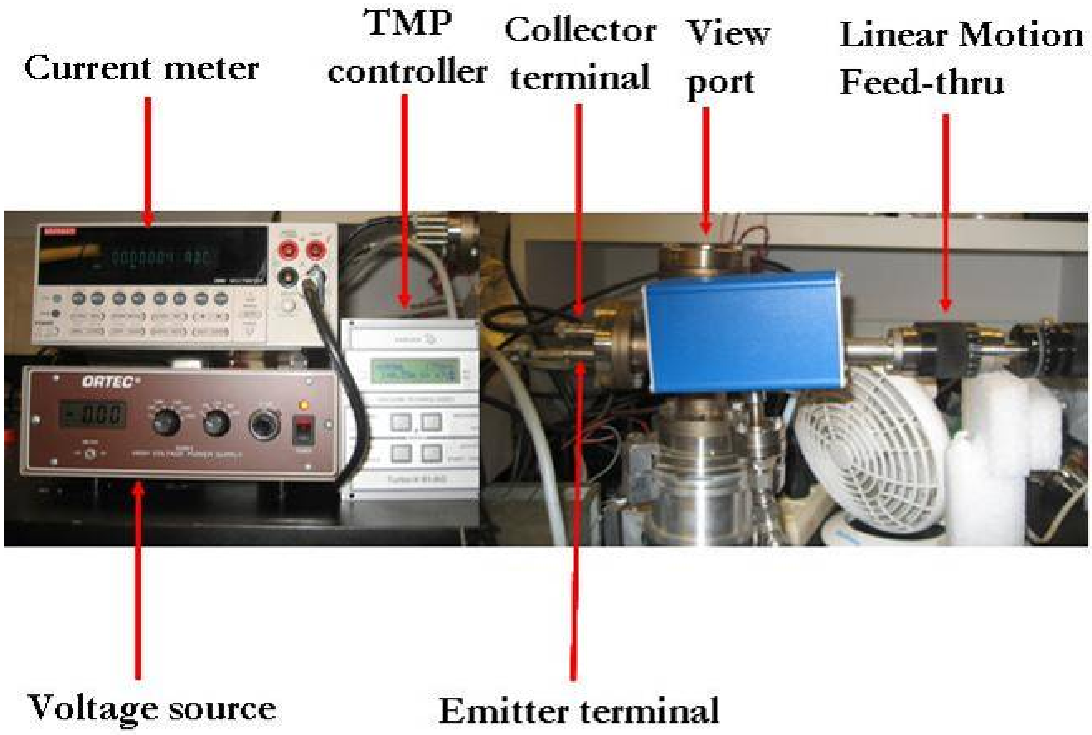

Figure 6.25 Field Emission Test Chamber

Initially, when the bias is applied, the emission current can be unstable due to the impurities at the tip surface. To overcome this problem, the tips are conditioned by thermal annealing or by applying a constant bias or by vacuum thermal electric (VTE) treatments. Of these three methods, VTE has been reported to stabilize the emission current by desorbing the impurities and reducing the surface work function [34]. In this study, a constant voltage (300-400 V) was applied for ~ 1 hour to condition the tip. After the emission current was stabilized, the voltage was gradually increased and the emission current was recorded. The emission current vs. electric field (I-F) characteristics of free standing emitter tips as collected at a molybdenum anode is shown in Figure 6.26 (a). The Fowler-Nordheim (F-N) characteristics are shown in Figure 6.26 (b). The exponential I-F in the forward bias and the linear F-N characteristics indicate the field emission behavior.

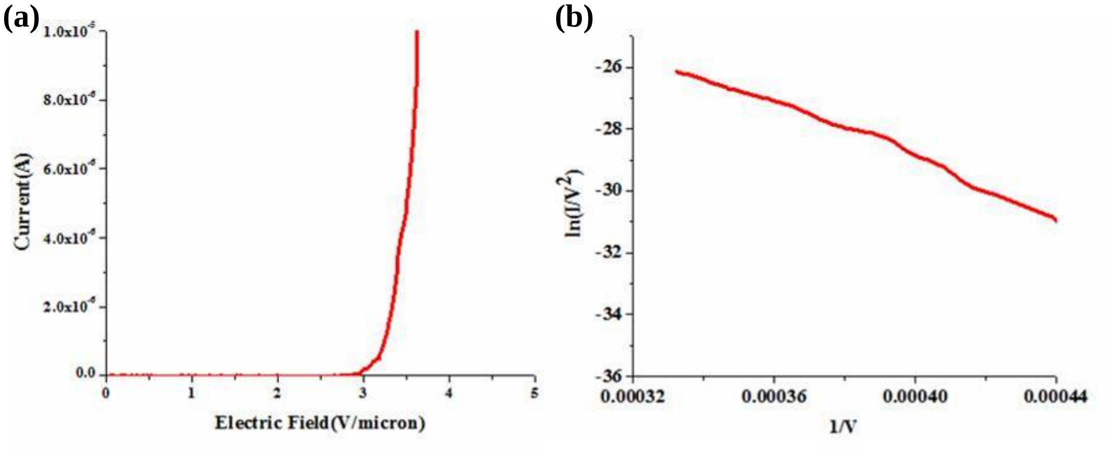

Figure 6.26 (a) Electric Field vs. Emission Current Characteristics (b) Fowler-Nordheim Characteristics of Free standing NCD Emitter Array With a Vacuum Gap of 1000 μm

The turn-on field is defined as the electric field at which there is a stable emission current of at least 1μA. In free standing devices, with an inter-electrode spacing of ~ 1000 μm, the turn-on electric field was found to be ~ 3 V/μm. As the applied voltage was increased, the emission current increased to only few microamperes. Due to the large separation between the anode and the cathode, the emission does not occur under low applied voltages. The gap between the anode and the cathode was gradually reduced after improving the fabrication methods. With a vacuum gap of 500 μm, the turn-on fields reduced to ~ 1.5 V/μm. The emission current vs. electric field characteristics of these devices at the turn-on voltage is shown in Figure 6.27.

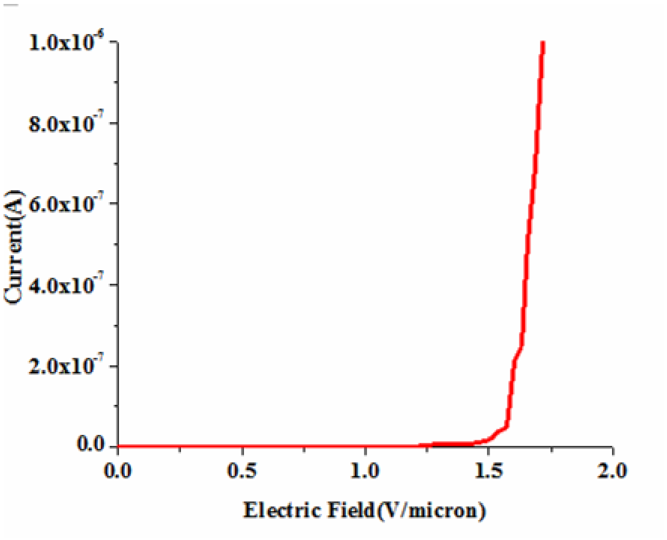

Figure 6.27 Electric Field vs. Emission Current Characteristics of Free Standing NCD Emitter Array With a Vacuum Gap of 500 μm

By reducing the inter-electrode spacing further to 300 μm, a lowest turn-on field of ~ 0.8 V/μm and highest emission current of 20 μA was achieved from free standing devices. The field emission characteristics of the device are shown in Figure 6.28.

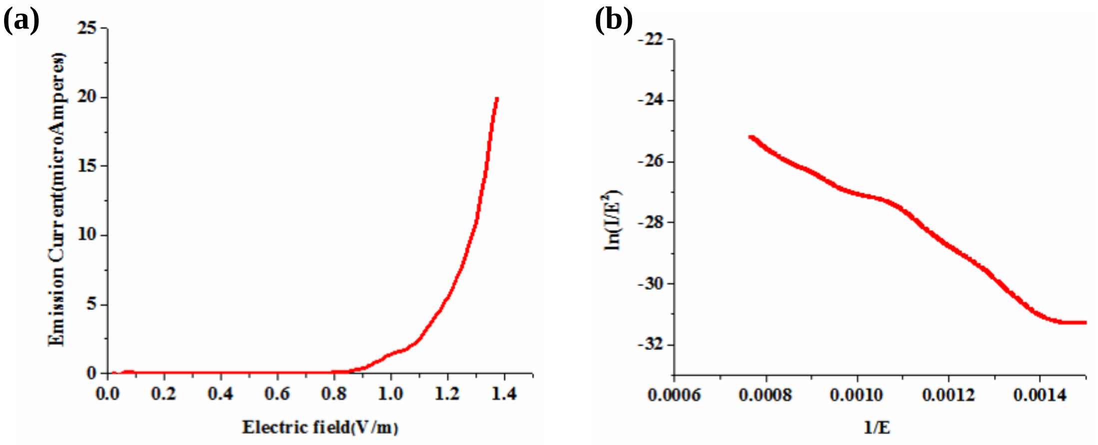

Figure 6.28 (a) Electric Field vs. Emission Current Characteristics (b) Fowler-Nordheim Plot With a Vacuum Gap of 300 μm

In all the above cases, it can be observed that under forward bias, the emission current increases exponentially (Figure 6.28 (a)) representing a simple diode characteristics. The electric fields of lines are highly concentrated at the apex and their density decreases away from tip. Therefore, as the inter-electrode spacing is changed, the turn-on field correspondingly changes. Besides, the linear trend in the Fowler-Nordheim plots (Figure 6.28 (b)) of the devices confirms that the electron flow in the devices is by tunneling.

6.13. Theoretical Analysis of the Field Emission Data

The field emission data is primarily examined by Fowler-Nordheim equation given by:

$$I = aJ = aA\left(\frac{LV}{Rd}\right)^2 \exp\left(\frac{-B}{\frac{LV}{Rd}}\right) \tag{6.1}$$

The F-N plot shows a linear characteristics between $\ln(I/E^2)$ vs. $1/E$. Accordingly, the linear mathematical equation can be written as

$$y = mx + c \tag{6.2}$$

$$m = -(B\Phi^{3/2})/\beta \tag{6.3}$$

$$= -(B\,\Phi^{3/2})/(L/R) \tag{6.4}$$

$$c = \ln((aA\beta^2)/\Phi) \tag{6.5}$$

$$A\ (\text{constant}) = 1.54 \text{ X } 10^{-6} \tag{6.6}$$

$$B\ (\text{constant}) = 6.83 \text{ X } 10^{7} \tag{6.7}$$

The slope and intercept of the F-N equation includes three unknown factors (Φ, β, and area (a)). It is not possible to deduce three unknown quantities from two equations. Therefore, one of the three parameters has to be determined using another technique. The emission from the individual tips takes place only from few atomic sites at the tip apex. Therefore, it is difficult to precisely estimate the net emission area. Hence, the emission area is omitted for the calculations. The geometrical field enhancement factor (β) can be estimated by SEM. The value of β in the emitter arrays varied between 56 to 140 for tips with height of 5.6 μm and 14 μm respectively.

For the field emission characteristics of free-standing devices shown in Figure 6.28 (b), the approximate linear mathematical fitting (Figure 6.29) is done to calculate the field emission parameters.

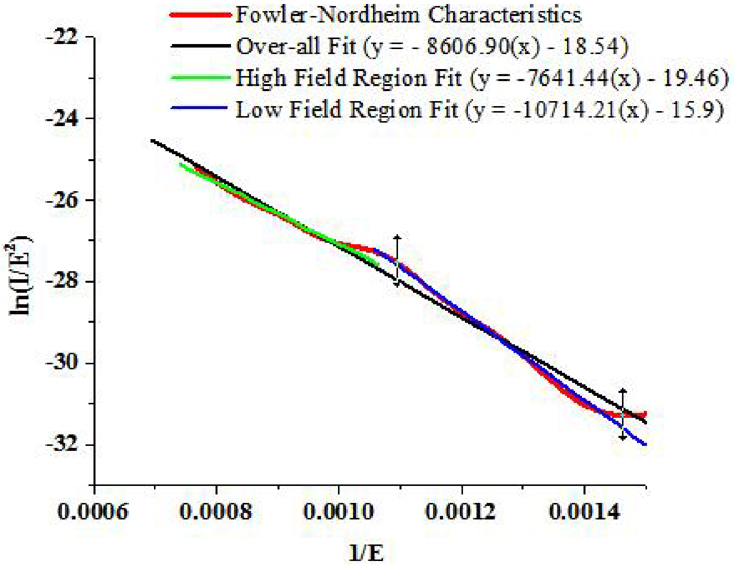

Figure 6.29 Fowler-Nordheim Characteristics With Approximate Mathematical Fit

The variation in the slopes across the high field and the low field regions is due to the image force effect [34]. The calculated value of Φ from the slope of the over-all curve was found to be 0.036 eV. Though the theoretical models showed that the nitrogen forms a shallow donor level with a net negative value of the electron affinity and work function, the true work function is slightly positive. Therefore, the diamond surface possesses an effective negative electron affinity instead of a true negative electron affinity.

6.14. Characterization of a Field Emission Sensor

The field emission sensors were fabricated with cathode and anode areas listed in Table 5.2 and Table 5.3 respectively. As discussed in chapter. 4, higher pressures or loads can be exerted on smaller anode membranes, while in the larger membranes, the full scale pressure range was reduced by at least one-half to operate the sensor in a linear and safe operating range of the device. The field emission sensor was tested in the same test chamber as the field emission source. Due to certain limitations in the system, the pressure inside the test chamber could not be increased through a leak valve in a controlled way. Hence, a linear motion feed through with an end effecter was employed to contact the anode and displace the membrane. Therefore, during this measurement, the actual change in the current is a function of the deflection of the center of the membrane. A proof-of concept of a field emisison sensor is demonstrated while further investigation is necessary to completely optimize the performance.

The dimensions of the cathode and the anode for the tested field emission sensor were 7000 X 7000 µm2 and 10000 X 10000 µm^2 respectively. In this version of devices, the anode and the cathode are separated by at least ~ 270-280 µm. Unlike the free standing devices, where the anode was a thin molybdenum plate, the anode of the capped devices has a thin silicon membrane. It was observed that the field emission properties of the capped devices were different than the free standing emitters. The turn-on voltage of the capped devices was found to be ~ 2 kV and the corresponding turn-on electric field was ~ 8V/µm. For the same emission current and inter-electrode spacing of ~ 280 to 300 µm, the turn-on electric field of free standing devices was ten times less than the capped devices. The turn-on electric field vs. emission current characteristics and the corresponding Fowler-Nordheim plot of the capped devices is shown in Figure 6.30 (a) and (b) respectively.

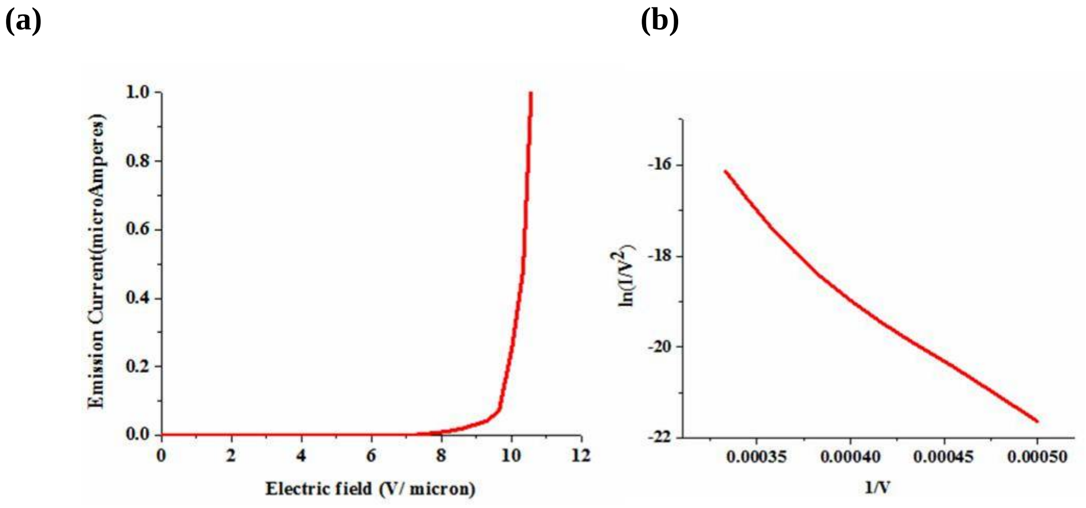

Figure 6.30 (a) Electric Field vs. Emission Current Characteristics (b) Fowler-Nordheim Characteristics of Capped Field Emisison Devices

In case of free standing devices, the anode is made of highly conductive metal plate, and therefore, the current losses within the metal plate are minimal. Besides, the devices are tested at a true base vacuum of 5 X 10^{-8} T. As the emission current directly depends up on the vacuum level in the test chamber, higher emission current and lower turn-on fields can be obtained at higher vacuum level.

On the other hand, in the capped field emission devices, the anode is made of silicon membrane. The electrical conductivity of the silicon membranes will be very much lower than the molybdenum plate. Moreover, Si (100) wafers used for the fabrication of the membranes are not heavily doped. Therefore, significant loss in the emission current can take place within the anode before it is collected. In the capped field emission devices, though the integration of anode and cathode is done under vacuum conditions, true vacuum inside the cavity cannot be exactly determined once they are bonded. Therefore, the voltage required for the emission of equivalent current is higher. The field emission sensor is tested under constant voltage mode. After collecting a stable emission current of 1 μA, the end effecter of the linear feed through was brought in contact with the anode to push the membrane toward the cathode. The emission current values were recorded as the relative position of the anode was changed from its previous position. The emission current increased from 1 μA (at 280 μm separation) to 25 μA (at 50 μm separation) at a constant turn-on field of ~ 8V/μm. A linear response was obtained between the change in the current vs. change in the relative position of the membrane. The corresponding pressure exerted on the membrane due to the deflection is obtained theoretically. The emission current is a linear function of the applied load (Figure 6.31). As the maximum travel of the linear motion feed through was limited to ~ 280 μm, the calculated value of the maximum load was below 40 psi. The current design of the field emission sensor limits its operation only to a low pressure regime.

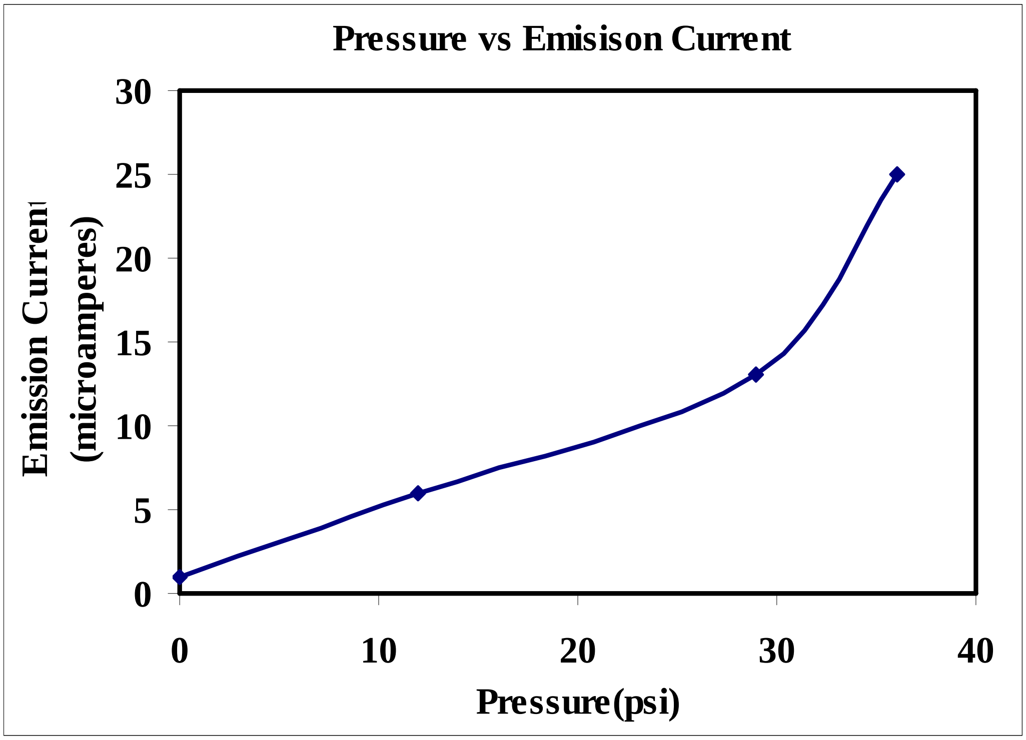

Figure 6.31 Pressure vs. Emission Current Characetristics

6.15. Summary

This chapter has discussed the process details for the fabrication of field emitter arrays by mold technique and anode-on-membranes using standard silicon wafers. The challenges in the fabrication of a vertical field emission device were presented and alternative process techniques have been developed for the successful device fabrication. Though the two types of anodes were fabricated, the difficulty in the integration of the second generation anode mask was a limitation. Two types of emitter devices were tested for their field emission characteristics in a diode configuration. The capped field emission devices were tested as a field emission source and a possible field emission sensor. Low turn-on electric fields (0.8 V/µm) were obtained in the un-capped emission devices while the turn-on electric field increased by an order of ten times (8 V/µm) in an integrated anode device. The field emission parameters of free standing and capped emission devices were different due to the different anode materials and relatively lower vacuum level during the test in the capped devices.

CHAPTER 7. CONCLUSIONS

7.1. Summary

The primary aim of this research was to develop the process for the application of CVD diamond thin films as a structural material in the microelectronics and microelectromechanical system (MEMS) devices. The research was two-folded with much of the focus on the growth of NCD thin films by microwave plasma enhanced chemical vapor deposition (MPECVD) technique and their characterization. Toward the growth of the NCD films, this research has presented three aspects. Firstly, the nucleation densities have been evaluated and improved method of seeding has been experimentally found. The next part of the research was focused on the development of process recipes for the growth of NCD films using hydrogen poor gas chemistry in presence of excess argon and a trace amount of methane at high microwave discharges. The structural and mechanical properties of the films were evaluated by the use of analytical and metrology tools. Finally, the optimized process recipes were used to grow high quality nanodiamond films on large area substrates. The next part of the research discussed on the development of conductive NCD films using nitrogen in the gas chemistry. The growth process has been optimized to obtain electrically conductive NCD films. The structural and the electrical properties of the conductive films were evaluated and the process has been optimized for its application in the device fabrication.

The second part of the research focused on the fabrication of field emission devices using conductive NCD films. The benefit of using NCD as a structural material for the fabrication of “Spindt-type” devices is recognized and the details on the fabrication of the vertical field emission devices by silicon mold technique were discussed. Both free standing, and capped field emitter devices were fabricated. A proto-type field emission sensor was fabricated using “anode-on-membrane” geometry. The fabrication of integrated field emission sensor includes three wafer processes with six levels of lithography and two levels of packaging. The anode-on-membrane configuration was designed to have thin silicon membranes and the cathode is made of nanodiamond field emitter arrays. The anode of the membrane forms the mechanical component of the sensor and the electrical component or as an electron collector in the field emission device. The integration of individual components was done by anodic bonding technique. The challenge in the fabrication of capped vertical emitter device was to achieve the vacuum gap between the anode and the cathode with optimum separation for the emission characteristics to be reliable. The field emission device in this configuration can be represented as a diode and their emission characteristics were tested in a high vacuum test chamber to determine the electric fields and the emission current densities. Low turn-on field of 0.8 V/µm and an emission current of 20 µA were obtained on the free standing devices while the turn-on fields in the capped devices increased by an order of magnitude.

7.2. Future Work

Much of the work in the growth and characterization of both intrinsic and conductive NCD thin films has been reported in the literature. Nevertheless, a fundamental study toward the nucleation and growth of the films is essential to fully exploit the material properties for its application in microelectronic device processing. During this entire research, the seeding has been initiated by ultrasonic scratch method. Alternative methods such as bias enhanced nucleation needs to be fully understood and the process has to be optimized for its application in *Cyrannus I* IPLAS reactor. As the growth rate of the nanodiamond films is less, through-put can be increased by in-situ seeding using bias enhanced nucleation technique. Though extensive characterization techniques have been used to analyze the structural, mechanical and electrical properties, the thermal properties of the films have to be evaluated as the future microelectronics industry needs high efficiency heat sinks. During the growth of conductive NCD films, it was observed that the addition of nitrogen in the reactor drastically changes the behavior of the microwave plasma discharge. Therefore, the process has to be further optimized to address this issue and grow conductive films on 100 mm wafers.

In terms of the device fabrication, vertical field emitter devices have been fabricated using diamond and several other materials. The current research focused primarily on the application of conductive NCD films for electron emitters. As mentioned in chapter. 5, the dimensions of the trapezoidal base determine the tip height which in turn determine the geometrical field enhancement factor. Therefore, for smaller base width and pitch, the density of the emitter tips can be increased, and correspondingly the field emission current can be increased. Therefore, the next generation devices have to be fabricated using improved device designs. Further, the method of tip sharpening by oxidation can be included in the fabrication process to reduce the radius of the tip and improve the field emission properties.

The fabrication of a proto-type field emission sensor has been described in this research. In the current test method, the load exerted and the corresponding deflection on the membrane is a relative position of the membrane displaced by the motion feed through. The current design of the field emission sensor limits its operation only to a low pressure regime. It is important to increase the net anode area for efficiently collecting the field electrons, but on the other hand, as the anode is made of thin membranes, the larger membranes tend to deflect more than the safe operating range and therefore limit the operation of the sensor to a narrow pressure scale. Though an improved design for the fabrication of the anode membranes was aimed, the difficulties in the integration of the individual components have limited its application. Therefore, alternative fabrication procedures have to be implemented to address these issues. The next generation devices can be fabricated by improving the designs of the anode and the cathode masks.

REFERENCES

1. S. Tolansky, (1962). The History and Use of Diamond, London: Shenval Press.

2. Davies, (1984). Diamond. Bristol: Adam Hilder Ltd.

3. W. P. Kang, J. L. Davidson, K. Subramanian, B. K. Choi, and K. F. Galloway, (2007). Nanodiamond Lateral VFEM Technology for Harsh Environments, IEEE Transactions on Nuclear Science, 54, 4.

4. L. S. Pan and D. R. Kania, (1995). Diamond: Electronic Properties and Applications, Boston: Kluwer Academic Publishers.

5. General Electric Company, (1955). Press release.

6. W. G. Eversole, (1962 a) U.S. Patent 3,030,187, (1962 b) U.S. Patent 3,030, 188.

7. J. C. Angus, H. A. Will, and W. S. Stanko, (1968). Growth of Diamond Seed Crystals by Vapor Deposition, J. of Appl. Phys. 39, 6, 2915.

8. B. V. Deryagin, and D. V. Fedoseev, (1976). Sci. Am, 233, 102.

9. F. P. Bundy, H. T. Hall, H. M. Strong, and R. J. Wentorf Jr., (1955). Man Made Diamonds, Nature, 176, 51.

10. S. Aisenberg, R. Chabot, (1971). Ion-Beam Deposition of Thin Films of Diamond like Carbon, J. of Appl. Phys. 42, 2953.

11. Electronic-reference: http://newton.ex.ac.uk/research/qsystems/people/sque/diamond/structure/

12. R. F. Davis, (1993) Diamond Films and Coatings.

13. M. A. Prelas, G. P. Popovici, and L. K. Bigelow, (1998). Handbook of Industrial Diamonds and Diamond Films, New York: Marcel Dekker.

14. Paoletti and A. Tucciarone, (1997). The physics of Diamonds, Amsterdam, IOS Press.

15. W. B. Choi, D. S. Chung, J. H. Kang, H. Y. Kim, Y. W. Jin, I. T. Han, Y. H. Lee, J. E. Jung, N. S. Lee, G. S. Park, and J. M. Kim, 1999. Fully sealed, high-brightness carbon-nanotube field-emission display, Appl. Phys. Lett, 75, 3725.

16. L. H. Pan, V. J. Peridier, and T. E. Sullivan, (2005). Quantum filtering of electron emission from ultrasharp tips, Phys. Rev. B71, 035345.

17. J. L. Davidson, W. P. Kang, Y. M. Wong, K. Subramanian, (2006). Diamond/Carbon Field Emission Based Structures for Sensors and MEMS, 210th ECS Meeting.

18. I. Brodie and P. R. Schwoebel, (1994). Vacuum microelectronic devices, Proc. of the IEEE, 82, 1006.

19. C. A. Spindt, (1968). A thin film field-emission cathode, J. Appl. Phys. 39, 3504.

20. S. E. Huq, L. Chen, P. D. Prewett, (1995). Sub 10nm silicon field emitters produced by electron beam lithography and isotropic plasma etching, Microelectronics engineering, 27, 95.

21. M. J. Powers, M. C. Benjamin, L. M. Porter, R. J. Nemanich, R. F. Davis, J. J. Cuomo, G. L. Doll, Stephen J. Harris, (1995). Observation of a negative electron affinity for boron nitride, Appl. Phys. Lett, 67, 3912.

22. M. C. Benjamin, C. Warig, R. F. Davis, R. J. Nemanich, (1994). Observation of a negative electron affinity for heteroepitaxial AlN on α(6H)-SiC (0001), Appl. Phys. Lett, 64, 3288.

23. W. P. Kang, A. Wisitsora-at, J. L. Davidson, O. K. Tan, W. G. Zhu, Q. Li and J. F. Xu, (2003). Effect of annealing temperature on the electron emission characteristics of silicon tips coated with $Ba_{0.67}Sr_{0.33}TiO_3$ thin film, J. Vac. Sci. Technol. B, 21, 1, 453.

24. X. D. Bai, C. Y. Zhi, S. Liu, E. G. Wang, Z. L. Wang, (2003). High-density uniformly aligned silicon nanotip arrays and their enhanced field emission characteristics, Solid State Communications 125, 185.

25. Z. S. Wu, S. Z. Deng, N. S. Xu, Jian Chen, J. Zhou, and Jun Chen, (2002). Needle-shaped silicon carbide nanowires: Synthesis and field electron emission properties, Appl Phys. Lett, 80, 20, 3829.

26. C. J. Lee, T. J. Lee, S. C. Lyu, Y. Zhang, and H. J. Ruh, (2002). Field emission from well-aligned zinc oxide nanowires grown at low temperature, Appl. Phys. Letters, 81, 3648.

27. S. Kar, S. Chakrabarti and S. Chaudhuri, (22006). Morphology dependent field emission from In_2O_3 nanostructures, Nanotechnology 17, 3058.

28. Y. J. Chen, Q. H. Li, Y. X. Liang, and T. H. Wang, Q. Zhao and D. P. Yu, (2004). Field-emission from long SnO_2 nanobelt arrays Appl. Phys. Letters, 85, 23, 5682.

29. M. Miyauchi, H. Tokudome, Y. Toda, T. Kamiya, H. Hosono, (2006). Electron field emission from TiO_2 nanotube arrays synthesized by hydrothermal reaction, Appl. Phys. Lett, 89, 043114.

30. S. Iijima, (1991). Helical microtubules of graphitic carbon, Nature, 354, 56.

31. B. C. Djubua, N. N. Chubun, (1991). Emission properties of Spindt-type cold cathodes with different emission cone material, IEEE Trans. Electron. Dev. 38 (10), 2314.

32. A. R. Krauss, O. Auciello, M. Q. Ding, D. M. Gruen, Y. Huang, V. V. Zhirnov, E. I. Givargizov, A. Breskin, R. Chechen, E. Shefer, V. Konov, S. Pimenov, A. Karabutov, A. Rakhimov, N. Suetin, (2001). Electron field emission for ultrananocrystalline diamond films, J. Appl. Phys. 89, 5, 2958.

33. V. V. Zhirnov, G. J. Wojak, W. B. Choi, J. J. Cuomo, and J. J. Hren, (1997). Wide band gap materials for field emission devices, J. Vac. Sci. Technol. A 15, 3, 1733.

34. Anurat Wisitsorat-at, (2002) Micropatterned diamond field vacuum field emission devices, Ph. D Dissertation.

35. J. Robertson, M. J. Rutter, Band diagram of diamond and diamond-like carbon surfaces (1998). Diam. and Relat. Mater, 7, 620.

36. M. J. Rutter, J. Robertson, (1998). Ab intio calculation of electron affinities of diamond surfaces, Phys. Rev. B, 57, 9241.

37. K. Subramanian, W. P. Kang, J. L. Davidson, J. D. Jarvis, W. H. Hofmeister, B. K. Choi, M. Howell, (2006). Geometrical field enhancement on micropatterned nanodiamond film for electron emissions, 15, 2-3, 417.

38. R. H. Fowler, L. Nordheim, (1928). Proc. Roy. Soc. London A119, 173.

39. V. N. Tondare, N. Pradeep, D. D. Bambaladi, V. P. Godbole and D. S. Joag, (2001). Field emission from diamond coated tungsten tips, Solid-State Electronics, 45, 957.

40. O. Groning, O.M. Kuttel, P. Groning, L. Schlapbach, (1999). Field emission properties of nanocrystalline chemically vapor deposited-diamond films, J. Vac Sci. Technol. B, 17, 1970.

41. W. P. Kang, A. Wisitsora-at, J. L. Davidson, M. Howell, and D. V. Kerns,Q. Li and F. Xu, (1999). Sub-volt turn-on voltage self-align gate diamond emitter fabricated by self-align-gate-sharpened molding technique, J. Vac. Sci. Technol. B 17.2, 740.

42. W. P. Kang, J. L. Davidson, A. Wisitsora-at, M. Howell, A. Jamaludin, Y. M. Wong, K. L. Soh, and D. V. Kerns, (2003). Fabrication and field emission characteristics of lateral diamond field emitter, J. Vac. Sci. Technol. B 21.1, 593.

43. S. P. Chang and M. G. Allen, (2004). Capacitive pressure sensors with stainless steel diaphragm and substrate, J. Micromech. Microeng, 14, 612.

44. J. L. Davidson, D. R. Wur, W. P. Kang, D. Kinser and D.V.Kerns, (1996). Polycrystalline Diamond Pressure Microsensor, Diam. and Relat. Materials, 5, 86.

45. P. K. Pattnaik, B. Vijayaaditya, T. Srinivas, A. Selvarajan, (2005). Optical MEMS pressure sensor using ring resonator on a circular diaphragm, International Conference on MEMS, NANO and Smart Systems Proceedings. 24-27, 277.

46. D. Nicolaescu, (1995). Modeling of the field emitter triode (FET) as a displacement/pressure sensor, Applied Surface Science 87-88, 61.

47. M. I. Marqués, P. A. Serena, D. Nicolaescu and J. Itoh, (1999). Modeling of a pressure sensor based on an array of wedge emitters, Applied Surface Science, 146, 1-4, 239.

48. Dan Nicolaescu, Valeriu Filip, Junji Itoh, (2000). Analysis of a pressure sensor using n-Si/nitrogen doped diamond cathodes, J. Vac. Sci. Technol. B 18.2, 1077.

49. H.C. Lee, R. S. Huang, (1992). A theoretical study on field emission array for microsensors, IEEE Transaction on Electronic Devices, 39, 2, 313.

50. Zhiyu Wen, Ying Wu, Zhengyuan Zhang, Shilu Xu, Shanglian Huang and Youli Li, (2003). Development of an integrated vacuum microelectronic tactile sensor array, Sensors and Actuators A, 103, 301.

51. N. Badi, K. He, A. Nair, A. Bensaoula, (2004). Design and fabrication of field emission- based pressure microsensors, Vacuum Nanoelectronics Conference, Technical Digest of the 17th International Conference, 24-25.

52. I. Kleps, A. Angelescua, N. Samfirescu, A. Gil, A. Correia, (2001). Study of porous silicon, silicon carbide and DLC coated field emitters for pressure sensor application, Solid-State Electronics, 45, 997.

53. Rajeshuni Ramesham, (1999). Fabrication of diamond microstructures for microelectromechanical systems (MEMS) by a surface micromachining process, Thin Solid Films 340, 1.

54. M. Belmonte, P. Ferro, A. J. S. Fernandes, F. M. Costa, J. Sacramento, R. F. Silva, (2003). Wear resistant CVD diamond tools for turning of sintered hard metals, Diam. and Relat. Mater, 12, 738.

55. S. Turchetta, L. Carrino, W. Polini, (2005). CVD diamond insert in stone cutting, Diam. and Relat. Mater, 14, 641.

56. G. S. Yang, D. M. Aslam, M. White, J. J. McGrath, (1997). The characterization of single structure diamond heater and temperature sensor, Diam. and Relat. Mater, 6, 394.

57. D. M. Gruen, X. Pan, A. R. Kauss, S. Liu, J. Luo, C. M. Foster, (1994). Deposition and Characterization of Nanocrystalline Diamond Films, J. Vacuum Science and Technology, A, Vacuum Surface Films, 12, 4, 1491.

58. D. Zhou, D. M. Gruen, L. C. Qin, T. G. McCauley, A. R. Krauss, (1998). Control of diamond film microstructure by Ar additions to CH_4/H_2 microwave plasmas, J. of App. Phys, 84, 1981.

59. O. Auciello, J. Birrell, J. A. Carlisle, J. E. Gerbi, X. Xiao, B. Peng and H. D. Espinosa, (2004). Materials science and fabrication processes for a new MEMS technology based on ultrananocrystalline diamond thin films, J. Phys.: Condens. Matter 16, R539.

60. Y. Hayashi, T. Soga, (2004). Structural, optical and mechanical properties of nanostructure diamond synthesized by chemical vapor deposition, Tribology International, 37, 965.

61. M. Kubovic, K. Janischowsky, E. Kohn, (2005). Surface channel MESFETs on nanocrystalline diamond, Diam. and Relat. Mater, 14, 514.

62. N. S. Xu, J. Chen, S. Z. Deng, K. H. Wu and E. G. Wang, (2000). Study of field electron emission from nanocrystalline diamond thin films grown from a N_2/CH_4 microwave plasma, J. Phys. D: Appl. Phys. 33, 1572.

63. A. A. Morrish, Pehr E. Pehrsson, (1991). Effects of surface pretreatments on nucleation and growth of diamond films on a variety of substrates, Appl. Phys. Lett., 59, 4, 417.

64. G. S. Yang and M. Aslam, (1995). Ultrahigh nucleation density for growth of smooth diamond films, Appl. Phys. Lett, 66, 311.

65. S. Yugo, T. Kanai, T. Kimura, and T. Muto, (1991). Generation of diamond nuclei by electric field in plasma chemical vapor Deposition, Appl. Phys. Lett. 58, 10, 11, 1036.

66. B. R. Stoner, G.-H. Ma, S. D. Wolter, J. T. Glass, (1992). Characterization of Bias-enhanced nucleation of diamond on silicon by in-vacuo surface analysis and transmission electron microscopy, Physical Review B, 45, 19, 11067.

67. X. Jiang, W. J. Zhang, and C. P. Klages, (1998). Effects of ion bombardment on the nucleation and growth of diamond films, Physical Review B, 58, 11, 7064.

68. Sekaric, J. M. Parpia, and H. G. Craighead, T. Feygelson, B. H. Houston and J. E. Butler, (2002). Nanomechanical resonant structures in nanocrystalline diamond, Appl. Phys. Lett, 81, 23, 4455.

69. Electronic reference: http://www.cyrannus.com/pages/welcome.html.

70. S. J. Harris, and D. G. Goodwin, (1993). Growth on the reconstructed diamond (100) surface, J. Phys. Chem, 97, 1, 23.

71. D. M. Gruen, (1999). Nanocrystalline Diamond Films, Annu. Rev. Mater. Sci., 29, 211.

72. O. Matsumoto, H. Toshima, Y. Kamazaki, (1985). Effect of dilution gases in methane on the deposition of diamond-like carbon in a microwave discharge, Thin Solid Films, 128, 341.

73. O. Matsumoto, T. Katagiri, (1987). Effect of dilution gases in methane on the deposition of diamond-like carbon in a microwave discharge II: Effect of hydrogen, Thin Solid Films, 146, 283.

74. W. Zhu, A. Inspektor, A. R. Badzian, T. Mc-Kenna, R. Messier, (1990). Effects of noble gases on diamond deposition from methane-hydrogen microwave plasmas, J. Appl. Phys. 68, 1489.

75. S. Rotter, M. Yoshikawa, Y. Koga, Y. Tzeng, C. P. Klages, K. Miyoshi, (1999). Proceedings of the Applied Diamond Conference/ Frontier Carbon Technologies, ADC/FCT '99, 25.

76. N. N. Naguib, J. W. Elam, J. Birrell, J. Wang, D. S. Grierson, B. Kabius, J. M. Hiller, A. V. Sumant, R. W. Carpick, O. Auciello, J. A. Carlisle, (2006). Enhanced nucleation, smoothness and conformality of ultrananocrystalline diamond (UNCD) ultrathin films via tungsten interlayers, Chemical Physics Letters, 430, 345.

77. W. P. Leroy, C. Detavernier, R. L. Van Meirhaeghe, A. J. Kellock, C. Lavoie, (2006). Solid-state formation of titanium carbide and molybdenum carbide as contacts for carbon-containing semiconductors, J. Appl. Phys. 99, 063704.

78. Y. C. Lee, S. J. Lin, C. Y. Lin, M. C. Yip, W. Fang, I. N. Lin, (2006). Pre-nucleation techniques for enhancing nucleation density and adhesion of low temperature deposited ultra-nanocrystalline diamond, Diam. and Relat. Mater, 15, 2046.

79. S. Deguchi, and S. Mukai, (2006). Top-down Preparation of Dispersions of C60 nanoparticles in Organic Solvents, Chemistry Letters, 35, 4, 396.

80. Y. Chakk, R. Brener, and A. Hoffman, (1995). Enhancement of diamond nucleation by ultrasonic substrate abrasion with a mixture of metal and diamond particles, Appl. Phys. Lett. 66, 21, 2819.

81. S. A. Solin, A. K. Ramdas, (1970). Raman Spectrum of Diamond, Phys. Rev., B 1 1687.

82. R. J. Nemanich, S. A. Solin, (1979). First- and second-order Raman scattering from finite-size crystals of graphite, Phys. Rev., B 20, 392.

83. N. Wada, P.J. Gaczi, S.A. Solin, (1980). "Diamond-like" 3 fold-coordinated amorphous carbon, J. Non-Cryst. Solids 35, 543.

84. A. Gicquel, F. Silva, K. Hassouni, (2000). Diamond Growth Mechanisms in Various Environments, J. Electrochem. Soc.147, 2218.

85. Joachim Stöhr, (2003). NEXAFS Spectroscopy, New York: Springer Series in Surface Sciences.

86. F. L. Coffman, R. Cao, P. A. Pianetta, S. Kapoor, M. Kelly, L. J. Terminello, (1996). Near-edge x-ray absorption of carbon materials for determining bond hybridization in mixed sp^2/sp^3 bonded materials, Appl. Phys. Lett, 69, 4, 568.

87. R. Haubner, (2001). Comparison of sulfur, boron, nitrogen and phosphorus additions during low-pressure diamond deposition, Diam. and Relat. Mater. 14, 355.

88. T. Lin, Y. Yu, A. T. S. Wee, Z. X. Shen, K. P. Loh, (2000). Compositional mapping of the argon–methane–hydrogen system for polycrystalline to nanocrystalline diamond film growth in a hot-filament chemical vapor deposition system, Appl. Phys. Lett. 77, 2692.

89. L. Fayette, B. Marcus, M. Mermoux, G. Tourillon, K. Laffon, P. Parent, F. LeNormand, (1998). Local order in CVD diamond films: Comparative Raman, x-ray-diffraction, and x-ray-absorption near-edge studies, Phys. Rev., B 57, 14123.

90. U.A. Palnitkar, P.T. Joseph, H. Niu, H.Y. Huang, W.L. Fang, H.F. Cheng, N.H. Tai, I. N. Lin. (2008). Adhesion properties of nitrogen ion implanted ultra-nanocrystalline diamond films on silicon substrate Diam. and Relat. Mater, 17, 4-5, 864.

91. S. Bhattacharyya, O. Auciello, J. Birrell, J. A. Carlisle, L. A. Curtiss, A. N. Goyette, D. M. Gruen, A. R. Krauss, J. Schlueter, A. Sumant, P. Zapol, (2001). Synthesis and characterization of highly-conducting nitrogen-doped ultrananocrystalline diamond films, Appl. phys. Lett, 79, 10, 1441.

92. Y. Yamazaki, K. Ishikawa, N. Mizuochi, S. Yamasaki, (2005). Structural change in diamond by hydrogen plasma treatment at room temperature, Diam. and Relat. Mater, 14, 1939.

93. Y. C. Lee, D. Pradhan, S. J. Lin, C. T. Chia, H. F. Cheng, I. N. Lin, (2005). Effect of surface treatment on the electron field emission property of nano-diamond films, Diam. and Relat. Mater, 14, 2055.

94. A. N. Goyette, J. E. Lawler, L.W. Anderson, D. M. Gruen, T. G. McCauley, (1998). C_2 Swan band Emission Intensity as a Function of [C_2], Plasma Sources Sci. Technol, 7, 149.

95. J. Birrell, J. A. Carlisle, O. Auciello, D. M. Gruen, J. M. Gibson, (2002). Morphology and electronic structure in nitrogen-doped ultrananocrystalline diamond, Appl. Phys. Lett., 81, 12, 2235.

96. G. Sh. Gildenblat, S. A. Grot, C. W. Hatfield, C. R. Wronski, A. R. Badzian, T. Badzian, and R. Messier, (1989). Electrical properties of homoepitaxial diamond films, in Proc. Fall 1989 MRS, Boston, MA, 162, 297.

97. T. Teraji, M. Katagiri, S. Koizumi, T. Ito and H. Kanda, (2003). Ohmic Contact Formation for N-type Diamond by Selective Doping, Jpn. J. Appl. Phys., 42, L882.

98. J. E. Gerbi, O. Auciello, J. Birrell, D. M. Gruen, B. W. Alphenaar, J. A. Carlisle, (2003). Electrical contacts to ultrananocrystalline diamond, Appl. Phys. Letters, 83, 10, 2001.

99. A. Laikhtman and A. Hoffman, (2002). Enhancement of secondary electron emission by annealing and microwave hydrogen plasma treatment of ion-beam-damaged diamond films, J. Appl. Phys., 91, 4, 2481.

100. S. Bhattacharyya, (2004). Mechanism of high n-type conduction in nitrogen-doped nanocrystalline diamond, Physical Review B, 70, 125412.

101. V. Mortet, K. Haenen, J. Potmesil, M. Vanecek, and M. D'Olieslaeger, (2006). Diamond- Application to piezoelectric bimorph cantilever sensors, phys. stat. sol. (a) 203, 12, 3185.

102. K. C. Holmes, J. L. Davidson, W. P. Kang, A.L. Sternberg, (2002). Diamond Micromechanical Sensors for Pressure and Acceleration Sensing, IEEE proceedings, 45.

103. D. R. Wur, J. L. Davidson, W. P. Kang, and D. L. Kinser, (1995). Polycrystalline Diamond Pressure Sensor, Journal of Microelectromechanical Systems, 4, 1, 34.

104. M. I. Marque, P. A. Serena, D. Nicolaescu, A. Correia, (2000). Design of field emission based magnetic sensors, J. Vac. Sci. Technol. B 18.2., 1068.

105. A. Wisitsora-at, W. P. Kang, J. L. Davidson, D. V. Kerns, and S. E. Kerns, (2001). Diamond emitter arrays with uniform self-aligned gate built from silicon-on-insulator wafer, J. Vac. Sci. Technol. B 19.3, 971.

106. C. B. Nielsen, Z. C. Christensen, C. Pedersen, and E. V. Thomsen, (2004). Particle Precipitation in Connection with KOH Etching of Silicon, Journal of Electrochemical Society, 151(5) G338.

107. W. P. Kang, J. L. Davidson, A. Wisitsora-at, D. V. Kerns, and S. Kerns, (2001). Recent development of diamond microtip field emitter cathodes and devices, J. Vac. Sci. Technol. B, 19, 3, 936.

108. A. C. Ferrari, J. Robertson, (2001). Origin of the 1150 cm^{-1} Raman mode in nanocrystalline diamond, Phys. Rev. B. 63, 121405.

109. K. Teii, T. Ikeda, A. Fukutomi, K. Uchino, (2006). Effect of Hydrogen Plasma Exposure on the Diamond Films J. Vac. Sci. Technol. B 24, 1, 263.

110. R. Pfeiffer, H. Kuzmany, P. Knoll, S. Bokova, N. Salk, B. Günther,(2003). Evidence for trans-polyacetylene in nano-crystalline diamond films, Diam. and Relat. Mater, 12, 268.

111. S. Jeedigunta, P. Spagnol, J. Bumgarner, A. Kumar, (2007). Role of Nucleation in the growth of Nanocrystalline Diamond (NCD) Films: A Particular Study in the Fabrication of Micro-cantilevers, MRS Fall 2007 meeting, Boston, MA.

112. S. Jeedigunta, P. Spagnol, Z. Xu, J. Bumgarner, A. Kumar, (2006). Effect of Post Deposition Treatment of the Metal Contacts on the Electrical properties of Nitrogen Doped Nanocrystalline Diamond Films, MRS Fall 2006 meeting, Boston, MA.

113. S. Albin, L. Watkins, (1990). Electrical properties of hydrogenated diamond, Appl. Phys. Lett 56, 15, 1454.

114. Y. C. Chen, A. J. Cheng, M. Clark, Y. K. Liu, Y. Tzeng, (2006). Effects of post-deposition heat treatment and hydrogenation on electrical conductivity of nanodiamond films, Diam. and Relat. Mater. 15, 440.

115. J. Birrell, J. E. Gerbi, O. Auciello, J. M. Gibson, D. M. Gruen, J. A. Carlisle, (2003). Bonding structure in nitrogen doped ultrananocrystalline diamond, J. Appl. Phys 93, 9, 5606.

116. Materials Characterization, 10, ASM Handbook.

117. HERMON Beam line, Synchrotron Radiation Center, University of Wisconsin, Madison

118. Electronic reference: http://www.bristol.ac.uk/Depts/Chemistry/MOTM/diamond/cphased.gif

ABOUT THE AUTHOR

Sathyaharish Jeedigunta has received Bachelor of Technology in Electrical and Electronics engineering from Jawaharlal Nehru Technological University (JNTU), India in 2001. He has received Master of Science in Electrical Engineering with microelectronics as specialization from University of South Florida, Tampa in 2004. He has continued working toward the doctoral degree in Electrical engineering from the year 2004. During the doctoral work, he has worked on the development of thin films, nanostructures and fabrication of microelectronic devices. His dissertation work is focused on the development of the diamond thin films for microelectronics and MEMS applications. The author's other research interests include: one-dimensional nanostructures, photo-voltaics, and thin films. He has been affiliated with Materials Research Society (MRS) and The Metals Society (TMS).